Integrated Design Methods for Mini Organic Rankine Cycle Power Systems

Bahamonde, Juan S.

DOI
10.4233/uuid:200a93f9-531e-44ff-b73f-278394dc8299

Publication date
2018

Document Version
Final published version

Citation (APA)
Bahamonde, J. S. (2018). *Integrated Design Methods for Mini Organic Rankine Cycle Power Systems*. [Dissertation (TU Delft), Delft University of Technology]. https://doi.org/10.4233/uuid:200a93f9-531e-44ff-b73f-278394dc8299

Important note
To cite this publication, please use the final published version (if applicable).
Please check the document version above.

INTEGRATED DESIGN METHODS FOR MINI ORGANIC RANKINE CYCLE POWER SYSTEMS

א

Juan Sebastián Bahamonde Noriega

2018

INTEGRATED DESIGN METHODS FOR MINI ORGANIC RANKINE CYCLE POWER SYSTEMS

Dissertation

for the purpose of obtaining the degree of doctor
at Delft University of Technology,
by the authority of the Rector Magnificus prof.dr.ir. T.H.J.J. van der Hagen,
chair of the Board for Doctorates
to be defended publicly on
Friday 21 September 2018 at 10:00 o' clock

by

Juan Sebastián BAHAMONDE NORIEGA

Master of Science in Mechanical Engineering, Delft University of Technology, the Netherlands
born in Quito, Ecuador

This dissertation has been approved by the promotors.

Composition of the doctoral committee:

Rector Magnificus	chairperson
Prof.dr.ir. P. Colonna	Delft University of Technology, promotor
Dr.ir. M. Pini	Delft University of Technology, copromotor

Independent members:

Prof. dr. ir. L.L.M. Veldhuis	Delft University of Technology
Prof. dr. D. Sánchez	University of Seville
Prof. dr. J. Schiffmann	École Polytechnique Fédérale de Lausanne
Dr.-Ing. M. Hombsch	Dana N.V.
Dr. C.M. De Servi	Flemish Institute for Technological Research (VITO)

This research was funded by Bosch GmBH and the Netherlands Organization for Scientific Research, NWO.

ISBN 978-94-6375-112-4

An electronic version of this dissertation is available at
http://repository.tudelft.nl/.

The Aleph's diameter would be about two or three centimeters,
but the cosmic space was there, undiminished.

The Aleph. Jorge Luis Borges, 1945.

To my parents, to my sister, to my brother, to Cristina,
to everyone who has led me here.

CONTENTS

SUMMARY

The constant progress of humanity is inherently linked to an ever-increasing demand for energy. Coping with this demand by means of fossil-fuel power plants has lead to extensive environmental damage like global warming, destruction of natural habitats, and air pollution. In order to ensure the well-being of future generations, civilization must transition to a new energy mix, where clean energy technologies play a major role.

Currently, few clean technologies are widely exploited, notably, solar photo-voltaic and onshore wind power plants. As a result, the trends in the global energy market have changed in favor of the renewable energy sector, which supplied half of the electricity demand growth in 2016. However, achieving carbon-neutral energy generation is still a distant objective. With the current planetary environmental-related ambitions, the CO_2 discharge will decrease only after 2050; in 2100 reverting global warming will be practically impossible.

Within the new energy mix, decentralized energy conversion systems will play an important role due to advantageous features: they are customized according to the client need; and they are typically installed close to the end user, thus eliminating transmission losses. Moreover, they can be used in energy consumption sectors that require attention, e.g., road-transport fuel economy, building energy consumption, or energy-intensive industrial processes. In many of these cases, the available thermal energy sources share various characteristics, prominently, a low-to-medium peak temperature ($\leq 400^{\circ}$C), or a power output ranging from few kWs to tens of kWs. In the author's opinion, the organic Rankine cycle (ORC) technology is the best alternative to transform the potential of these types of sources into useful forms of energy.

High-temperature mini-ORC (*m*ORC) turbogenerators (power $\leq$ 50 kW, peak temperature $\geq 250^{\circ}$C) have gained increasing interest in the last years, specially because of their wide range of applications, and also because they can reach conversion efficiencies in excess of 20%. Nonetheless, their design poses difficult challenges. In many cases, the system must be sufficiently efficient, light and compact. The design paradigm is therefore different from that of conventional stationary ORC power plants of much larger capacity. Moreover, no consolidated experience exists, for R&D efforts were discontinued once the oil prices dropped in the 80's, thus leading to a lack of design guidelines.

The turbine realization is the most important task, mainly because few efficiency points can have a decisive impact in the entire project feasibility. Furthermore, the turbine design is an intricate challenge, for the machine specifications are tightly connected to the thermodynamic cycle operating conditions; and also because the design process might be constrained by limitations on the machine geometry (e.g., minimum blade height), or the machine operation (e.g., maximum rotational speed). The design for maximum system performance thus constitutes a constrained, multidimensional, and multi-objective optimization problem. The work reported in this dissertation provides methodologies capable of tackling this complex task; and also presents an exemplary application of the design of a high-temperature *m*ORC unit.

Method for the Preliminary Fluid Dynamic design of high-temperature mini-ORC turbines

The work in this chapter stems from two aspects that make the design of high temperature *m*ORC turbines particularly difficult: i) the design procedures employed for conventional turbomachinery do not apply; ii) the optimization problem features a large number of interdependent constraints, thus finding a feasible design space is troublesome and time consuming. To tackle this challenge, this chapter presents a two-step design method that integrates the thermodynamic cycle analysis and the turbine preliminary design. First, a feasible design space is defined by means of design calculations of the thermodynamic cycle coupled with those of the turbine. In this case, the turbine design employs a simplified constant-efficiency procedure. This design space is then used in the second step: a constrained optimization whose objective function integrates the thermodynamic cycle calculation and a turbine 1D meanline design code. The application of the method is illustrated with an exemplary case: the design of a 10 kW *m*ORC turbine. Three expander configurations are considered: a radial inflow, a three-stage radial outflow, and a three-stage axial turbine. The results suggest that a radial inflow turbine is the best alternative for high-temperature *m*ORC power plants: the optimal pressure ratio is not limited by the blade height, and its performance is weakly dependent on the tip clearance losses.

Active Subspaces for the Optimal Meanline Design of Unconventional Turbomachinery

Incorporating the working fluid design in the optimization process is a compelling challenge. The work presented in this chapter achieves so by including the parameters of the correlations employed to compute thermodynamic properties in the optimizer design space. As a consequence, the cumulative number of variables defining the thermodynamic cycle, the turbine, and the working fluid, surpasses the dozen. The design problem thus features the curse of dimensionality: solving it requires considerable computational resources, and it is impossible to find a global optimum. To tackle this challenge, a reduced-order model of the turbine total-to-static efficiency function is created by means of *Active subspace methods*. The study case is the design of a *m*ORC system operating with a single-stage radial inflow turbine. The resulting surrogate model is a smooth two-dimensional response surface that integrates into a single optimization framework the selection of the working fluid, the thermodynamic cycle calculation and the preliminary sizing of the turbine. Its evaluation consumes negligible computational resources, because it is an explicit algebraic equation. Furthermore, the opimal solutions can be found in a small-region in the response surface. These solutions contain information regarding the turbine geometry, the working fluid parameters, and the thermodynamic cycle operating conditions. Finally, the new model can be used to infer which parameters are dominant with respect to turbine performance. For instance, in this study, the most influential fluid model parameters are the molar mass, the critical temperature, and the acentric factor.

Hybrid Electric Powertrain for Long-haul Trucks and Buses: Preliminary Analysis of a New Concept Based on a Combined Cycle Power Plant

Heavy-duty road transport accounts for approximately 5% of the European Union's total greenhouse gas emissions, more than international shipping and aviation. Electric hybridization of the power train is likely the most promising alternative to face this problem. This chapter presents the analysis of a combined cycle unit as a prime mover for a hybrid electric heavy-duty vehicle. The combined cycle is constituted by a micro gas turbine (μGT)

fueled by natural gas or diesel, and a *m*ORC unit operating with toluene. The study has two steps: i) preliminary design of the combined cycle power plant, ii) estimation of the vehicle fuel economy and the emissions over a representative driving cycle. The study case is a fully loaded, 36 ton, long-haul truck. The hybrid power train is of the series type, because it decouples the combined cycle from the truck energy demand; the combined cycle thus runs at optimum conditions uninterrupted. The combined cycle system is designed with a peak efficiency of 0.44, and a nominal power output of about 150 kW, which corresponds to the power demand at cruise conditions. The system is compared against a vehicle featuring a next generation diesel engine, with a peak efficiency equal to 50 %. The hybrid power train presents remarkable advantages. Its fuel economy is higher than that of the benchmark. It produces emissions that are well below the regulated limits in the United States and Europe, without the need of an exhaust aftertreatment system. Finally, its discharge of greenhouse gases is lower than that from a diesel engine.

SAMENVATTING

De constante voortgang van de menselijkheid is inherent gekoppeld aan een altijd groeiende vraag naar energie. Het gebruik van energiecentrales op fossiele brandstoffen om deze vraag naar energie te behalen heeft tot aanzienlijke milieuschade geleid; waaronder wereldwijde temperatuurstijging, de vernieling van natuurlijke habitats en luchtvervuiling. Om het welzijn van toekomstige generaties te bewaken, moet men overstappen naar een nieuwe energie-mix, waarin duurzame energie technologieën een grote rol spelen. Op dit moment worden nog weinig van deze schone energie technologieën: met name zonne-energie en onshore windturbines, op grote schaal benut. Dit heeft ervoor gezorgd dat de trends in de globale energiemarkt zich hebben gericht op de hernieuwbare energie-sector. Deze sector heeft in 2016 de helft van de groei in de vraag naar energie geleverd. Echter is het behalen van een volledig koolstof-neutrale energie-generatie nog een doel van de toekomst. Met de huidige milieu-eisen zal de CO_2 uitstoot pas na 2050 afnemen, en in 2100 zal het vrijwel onmogelijk worden om de opwarming van de aarde om te keren.

Binnen de nieuwe energie-mix zullen decentrale opwekkingsystemen een belangrijke rol spelen vanwege hun voordelen: Deze zullen gespecialiseerd zijn op de wensen van de klant, en zijn over het algemeen dicht bij de eindgebruiker geplaatst, waardoor er geen transportverlies is. Ook kunnen deze worden ingezet bij de sectoren die hier het meeste van kunnen profiteren; b.v. in de transportindustrie, met name het brandstofgebruik, het energiegebruik van gebouwen, en in de energie-intensieve industriële processen. Veel van deze sectoren gebruiken warmtebronnen met soortgelijke karakteristieken, waaronder een late tot matige hoge temperatuur ($\leq 400^{\circ}$C), of een output van een paar kWs tot tientallen kWs. Naar de mening van de auteur is de organische rankinecyclus (ORC) technologie het beste alternatief om het verloren potentieel van deze bronnen om te zetten in bruikbare vormen van energie.

In de afgelopen jaren hebben mini-ORC (*m*ORC) turbogeneratoren op hoge temperaturen (50 kW, met piektemperatuur 250°C) meer aandacht gekregen, met name vanwege hun brede toepasbaarheid en omdat deze een omzettings-rendement van meer dan 20% kunnen behalen. Echter komt het ontwerpen ban deze generatoren met technische uitdagingen: In veel gevallen moeten deze systemen efficiënt, licht en compact genoeg zijn. Het ontwerp is hierdoor anders dan dat van conventionele vaste ORC energiecentrales met een hogere capaciteit. Bovendien is er nog weinig ervaring opgedaan in dit gebied, omdat de R&D werd stopgezet toen de olieprijzen daalden in de 80-er jaren. Dit heeft geleid tot een gebrek aan ontwerp-richtlijnen.

Het realiseren van de turbine in de *m*ORC is de meest belangrijke taak, vooral omdat een kleine verandering in de efficiëntie hiervan een grote impact kan hebben op de haalbaarheid van het hele project. Daarbij is het ontwerp van de turbine een ingewikkelde uitdaging, omdat de specificaties van deze machine verbonden zijn met de thermodynamische randvoorwaarden of omdat het ontwerp gelimiteerd wordt door geometrie (b.v. blad-hoogte) of door bedrijfsomstandigheden (b.v. maximum rotatiesnelheid). Het ontwerp voor de maximale prestatie is hierdoor een gelimeteerd en multi-dimensioneel optimalistie-probleem met meerdere doelstellingen. Het werk in dit proefschrift omvat

methodologieën die in staat zijn om deze complexe taak te voltooien, en bevat tevens een illustratieve toepassing van het ontwerp van een *m*ORC unit op hogere temperaturen.

Methode voor het voorlopige vloeistof-dynamica ontwerp van mini-ORC turbines op hoge temperaturen.

Het werk in dit hoofdstuk is ontstaan uit twee aspecten die het ontwerp van *m*ORC turbines op hoge temperaturen moeilijk maakt: i) De ontwerpprocedures voor conventionele turbomachines zijn niet van toepassing; ii) Het optimalisatie-probleem bevat een goot aantal onderling afhankelijke randvoorwaarden. Hierdoor is het vinden van een haalbare ontwerp-ruimte lastig en tijdrovend. Om deze uitdaging aan te gaan, wordt er in dit hoofdstuk een ontwerpmethode met twee stappen voorgesteld, die de thermodynamische cyclus-berekeningen en het voorlopige ontwerp integreert. Eerst wordt er een haalbare ontwerp-ruimte gedefinieerd d.m.v. berekeningen van de thermodynamische cyclus in combinatie met die van de turbine. In dit geval wordt er een procedure met constant rendement gebruikt voor het ontwerp van de turbine. De zo bepaalde ontwerpruimte wordt daarna gebruikt in de tweede stap: Een optimalisatie binnen randvoorwaarden, waarvan de objectieve functie zowel de thermodynamische cyclus-analyse als een 1D meanline design code combineert. Het toepassen van deze methode wordt geïllustreerd met een voorbeeld: Het ontwerpen van een 10 kW *m*ORC turbine. Er worden hier drie expander configuraties overwogen: Een turbine met radiale instroming, een drietrapse turbine met radiale uitstroming en een drietrapse axiale turbine. Uit de resultaten blijkt dat een turbine met radiale instroming de beste keuze is voor *m*ORC energiecentrales op hoge temperatuur: De optimale drukverhouding is niet gelimiteerd door de blad-hoogte, en de prestatie is zwak afhankelijk van de verliezen van de luchtspleet aan de punten van de schoepen.

Actieve deelruimten voor het optimale meanline ontwerp van onconventionele turbomachines.

Het combineren van het ontwerp van de werkvloeistof in het optimalisatieproces is een boeiende uitdaging. In dit hoofdstuk wordt uitgelegd hoe dit wordt gedaan met de parameters van de correlaties die toegepast worden voor de thermodynamische eigenschappen in de ontwerpruimte van de optimalisatie. As gevolg hiervan zijn er meer dan een dozijn variabelen die de thermodynamische cyclus, de turbine en de werkvloeistof definiëren. Het ontwerpprobleem is hierdoor vervloekt door de vele dimensies: Om deze op te lossen is een aanzienlijke hoeveelheid rekenkracht nodig, en het is onmogelijk om een globaal optimum te vinden. Om deze uitdaging op te lossen wordt er gereduceerd model van de totaal-naar-statische rendementsfunctie van de turbine gecreëerd d.m.v. methoden op *actieve deelruimten*. De gevalstudie in dit hoofdstuk omvat het ontwerp van een eentrapse radiale instroom turbine. Het resulterende surrogaat-model is een vloeiend tweedimensionaal reactieoppervlak, wat de keuze van de werkvloeistof, de thermodynamische cyclusberekeningen en de voorlopige dimensies van de turbine in een enkel optimalisatie proces integreert. De evaluatie hiervan gebruikt verwaarloosbaar weinig rekenkracht, omdat het een expliciet algebraïsche vergelijking omvat. Bovendien kunnen de optimale oplossingen in een klein gebied in het reactie-oppervlak gevonden worden. Deze oplossingen bevatten informatie over de geometrie van de turbine, de parameters van de werkvloeistof, en de werkomstandigheden van de thermodynamische cyclus. Tot slot kan er uit het nieuwe model worden afgeleid welke parameters bepalend zijn voor de turbine-prestaties. In de

gevalstudie blijkt bijvoorbeeld dat de meest kritieke parameters de molaire massa, de kritieke temperatuur en de acentric factor zijn.

Een nieuw concept gebaseerd op een Combined-Cycle Power Plant

Zwaar wegtransport is verantwoordelijk voor ongeveer 5% van de totale broeikas uitstoot van de Europese Unie, meer dan de internationale scheepvaart en de luchtvaart. De meest belovende manier om dit probleem op te lossen is om de aandrijflijn van zware voertuigen te hybridiseren. Dit hoofdstuk bevat de analyse van een combined-cycle unit als een hoofdaandrijver voor een elektrisch-hybride heavy-duty vrachtwagen. De combined-cycle bestaat uit een micro grasturbine (μGT), aangedreven door aardgas or diesel, en een mORC unit werkend met tolueen. De gevalstudie bestaat uit twee stappen: i) Voorlopig ontwerp van het combined-cycle opwekkingssysteem, ii) schatting van het brandstofverbruik en uitstoot gedurende een algemene rijcyclus. De studie behandelt een volbeladen long-haul truck van 36 ton. De hybride aandrijflijn is in serie geschakeld, omdat dit de combined-cycle van de energie benodigdheden van de truck ontkoppelt. Hierdoor loopt de combined-cycle onder optimale condities zonder onderbroken te worden. Het combined-cycle systeem is ontwikkeld met een maximale efficiëntie van 0.44, en een nominale energie-output van 150 kW, wat vergelijkbaar is met de vraag naar energie op cruise-omstandigheden. Het systeem word vergeleken met een voertuig dat is uitgerust met dieselmotoren, zoals ze in de toekomst gemaakt kunnen worden, met een maximale efficiënte van 50 %. De hybride aandrijflijn biedt in vergelijking opmerkelijke voordelen: De brandstofefficiëntie is hoger dan dat van de dieselmotor, omdat die altijd op zijn hoogst rendement kan draaien. Het produceert een uitstoot ver onder de gereguleerde limieten in de Verenigde Staten en Europa, zonder een nabehandeling op de uitlaat nodig te hebben. Ook is de uitstoot van broeikassen lager dan dat van de conventionele diesel motor.

1

INTRODUCTION

1.1. DECENTRALIZED ENERGY CONVERSION SYSTEMS IN THE NEW ENERGY-MIX

In the last decades, humanity has seen an unstoppable escalation of the global energy consumption, which has increased 60 % since 1990 [1, p. 28]. Although this demand has been mostly covered by fossil-fueled and gigawatt-size power plants, it is currently undeniable that a transition to a new energy supply paradigm is required, for the consequences from employing fossil fuels at large scale are evident. Air pollution, destruction of natural habitats, and global warming are important examples.

Systems integration is key to the future. Fossil-fuel plants will play an important role, yet their impact has to be reduced by a growing clean energy market that includes medium- and small-capacity suppliers. Ultimately, cities will receive their power from distributed, mostly renewable or renewable equivalent (waste heat recovery), energy sources coordinated by smart control systems. The perspectives are somewhat encouraging, because the global energy market is changing rapidly in favor of the renewable energy sector, which supplied half of the electricity demand growth in 2016 [1, p. 21]. As a result, it seems that the energy-related CO_2 discharge has been steady for the last three years [1, p. 17]. This is partly caused by the few clean energy technologies whose potential is extensively exploited, notably, solar photo-voltaic and onshore wind power plants.

However, it is way too early to claim that energy conversion technologies are on the right track to become carbon-neutral. If the current planetary environmental-related ambitions are maintained, civilization will face a potentially tragic future: CO_2 emissions will decrease only after 2050. In 2100, global warming will manifest with a total temperature rise of 2.7°C; at this point reverting the trend will be practically impossible [1, p. 19].

It is thus indispensable to foster the development of decentralized renewable energy systems that can be used in sectors that are somehow falling behind regarding sustainability, e.g., road-transport, building energy consumption, or energy-intensive industrial processes. These power plants are typically close to the user, hence featuring an inherent advantage: the elimination of transmission lines (and the corresponding losses). Moreover, their design is customized according to the characteristics of the energy source, the customer needs, and the surrounding environment. In many cases, the available thermal

energy sources share various characteristics, prominently, a low-to-medium peak temperature (≤ 400°C), or a power capacity ranging from few kW to tens of kW (e.g., automotive waste heat recovery Ref.[2], or concentrated solar power [3]). In the author's opinion, the organic Rankine cycle (ORC) technology is the best alternative to transform the potential energy from these types of sources into useful forms of work.

1.2. ORGANIC RANKINE CYCLE TECHNOLOGY

The ORC engine is a Rankine thermal machine in which the working medium is an organic compound that features a molecular weight larger than that of water. Relevant advantages stem from this practice [4, 5]:

- the working fluid critical parameters become additional degrees of freedom that allow the designer to maximize the thermodynamic cycle efficiency according to the source/sink temperature values.
- Maximum and minimum cycle pressures can be selected somewhat independently from the source/sink temperatures. Besides, it is possible to design thermodynamic cycle configurations otherwise unattainable with water, e.g., a supercritical cycle at a low temperature.
- It is also possible to design low-stress and comparatively economic turbines with few number of stages and a high efficiency, particularly for low power outputs and temperature ranges where steam turbines are impractical.
- Figure 1.1a presents an exemplary process flow diagram of an ORC unit with regeneration; Figure 1.1b shows the related thermodynamic cycle in the temperature-entropy diagram of the working fluid. Note that a high thermal efficiency can be achieved with a simple cycle configuration, thanks to a regeneration process that

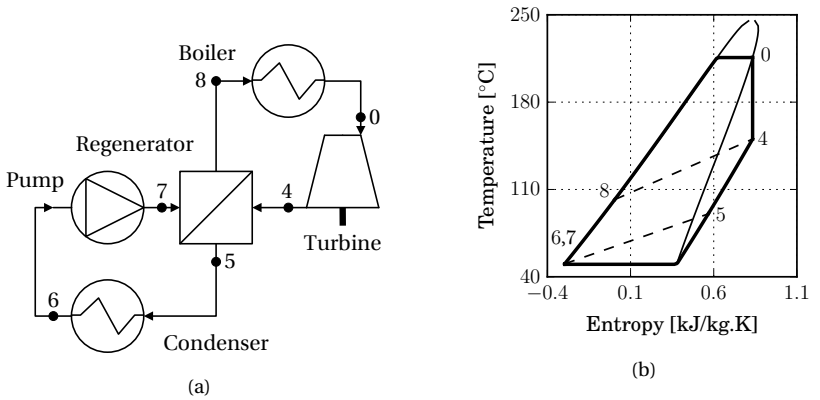

Figure 1.1: Exemplary ORC unit with regeneration. a) Process flow diagram. b) Temperature-entropy diagram of a thermodynamic cycle operating with hexamethyldisiloxane ($O[Si(CH_3)_3]_2$). Specifications: condensing temperature 50°C, evaporating pressure 12 bar, regenerator pinch temperature 40 K, no superheating, no pressure losses, isentropic compression/expansion.

does not require extracting inter-stage vapor. Note also that the fluid expansion is *dry*, thus condensation in the turbine flow passages is impossible.

- Finally, note that non-toxic and environmentally friendly working fluids are available, and that new fluids are constantly introduced in the market, e.g., see Refs. [6, 7].

The aforementioned characteristics provide ORC technologies with an extraordinary versatility, because the engine can be optimized to exploit virtually any external energy stream with a source/sink temperature difference ranging between 30 K and 500 K [8]. In particular, mini ORC systems (*m*ORC, power output ≤ 50 kW) constitute a game-changer subset, because they can be used in relevant renewable energy production systems like geothermal energy [5], waste heat recovery from automotive and aircraft prime movers [9, 10], biomass combustion [11], or concentrated solar power [5].

1.2.1. THE DESIGN OPTIMIZATION OF A HIGH-TEMPERATURE *m*ORC SYSTEM

Low-temperature *m*ORC units are a matter of constant interest, e.g., see Refs. [12–14]. These systems inherently feature a poor thermal efficiency and a low pressure ratio, and in most cases incorporate a volumetric expander. On the other hand, high-temperature *m*ORC power plants (turbine inlet temperature ≥ 250°C [8]) present a larger expansion ratio, and could reach efficiencies in excess of 20 %. In this case, a volumetric expander cannot be employed, because it is constrained by its built-in volume ratio, which ultimately makes the machine unrealizable or suboptimal [15]; a turbine thus is the sole alternative. Specially due to its high efficiency, high-temperature *m*ORC turbo-generators have gained increasing interest in the last years [16].

Although various high-temperature *m*ORC power plants were realized in past decades, e.g., see Refs. [17, 18], R&D efforts were discontinued once the oil prices dropped in the 80's. As a consequence, no consolidated experience exists, leading to a lack of design guidelines. In this respect, recent developments advocate employing an integrated approach, whereby the specifications of the thermodynamic cycle and the equipment are simultaneously conceived [16]. Note though that the design of the heat exchangers and the turbomachinery feature distinct grades of complexity and quite different challenges. Almost any effectiveness value can be achieved by increasing the amount of heat transfer surface, which is limited by economic constraints. Conversely, not every mini-turbine is realizable, because the optimal design process might fail due to technological and manufacturing constraints, like minimum blade height or maximum rotational speed; thus resulting in machines with unfeasible specifications or an unacceptable performance. The consequences of selecting a suboptimal machine are critical for the system design: an expander featuring a poor isentropic efficiency can have a disruptive impact in the system performance and its economic feasibility.

The design of the turbo-expander is therefore the most important and challenging task within the process leading to the realization of a high-temperature mini-ORC system, because the machine specifications are tightly connected to the working fluid and the cycle thermodynamic parameters. The design for maximum system performance thus constitutes a constrained, multidimensional, and multi-objective optimization problem. The work reported in this dissertation provides methodologies enabling the tackling of this complex task, and also presents an exemplary application of the design of a potential game-changer high-temperature *m*ORC unit.

1.3. THESIS OUTLINE

Three chapters form the main content of this dissertation. Each one is an adaptation from a scientific article already published in a peer-reviewed international journal. A summary of the chapters follows.

Chapter 2 describes novel optimal design method integrating the preliminary design of the thermodynamic cycle and that of the turbine. This method consists of two steps. First, a feasible design space is revealed by means of design calculations of the thermodynamic cycle coupled with those of the turbine. In this case, the turbine design employs a simplified constant-efficiency procedure. This approach mitigates the problem of the lack of design paradigms and guidelines for high-temperature *m*ORC turbines. The design space is then used in the second step: a constrained optimization whose design function integrates the thermodynamic cycle calculation and a 1D meanline code for turbine preliminary design. The application of the method is illustrated with an exemplary case, namely the design of a 10 kW *m*ORC turbine to be tested in the ORCHID setup currently under construction at the Delft University of Technology.

Chapter 3 introduces a method to incorporate the working fluid design in the optimization process. To do so, the parameters of the correlations employed to compute thermodynamic properties are included in the optimizer design space. As a result, the cumulative number of variables defining the thermodynamic cycle, the turbine, and the working fluid, can easily surpass the dozen. Solving such problem requires considerable computational resources, and it is practically impossible to find a global optimum. To tackle this challenge, *active subspace methods* are employed to create a reduced-order model of the turbine total-to-static efficiency function. The resulting surrogate model is a smooth two-dimensional response surface that integrates into a single optimization framework the selection of the working fluid, the thermodynamic cycle calculation and the preliminary sizing of the turbine. The method is applied to the design of a *m*ORC system operating with a single-stage radial inflow turbine. The novel design procedure is compared in terms of computational efficiency to the conventional approach based on using a genetic algorithm and the original multidimensional function.

Chapter 4 demonstrates the potential of *m*ORC systems by means of the design of a combined cycle unit as a prime mover for an innovative hybrid electric heavy-duty vehicle. This power plant is constituted by a micro gas turbine (μGT) fueled by natural gas or diesel, and a *m*ORC unit operating with cyclopentane. The evaluation of this system is done in two steps: preliminary design of the combined cycle power plant, and estimation of the vehicle fuel economy and the emissions over a representative driving cycle. The combined cycle system is designed with a peak efficiency of 0.44, and a nominal power output of about 150 kW, which corresponds to the power demand at cruise condition of a 36 ton long-haul truck. A series configuration with lithium-ion batteries is selected for the hybrid powertrain, for it decouples the prime mover from the truck power demand, thus allowing the combined cycle to run always at optimum conditions. The system is compared against a vehicle featuring a next generation diesel engine, with a peak efficiency equal to 50 %. The results show that the hybrid powertrain employing a combined cycle system offers significant advantages in terms of fuel economy and emissions.

REFERENCES

[1] Directorate of Sustainability, Technology and Outlooks, *Energy Technology Perspectives*, Tech. Rep. (International Energy Agency, 2017).

[2] L. Shi, G. Shu, H. Tian, and S. Deng, *A review of modified organic Rankine cycles (ORCs) for internal combustion engine waste heat recovery (ICE-WHR),* Renewable and Sustainable Energy Reviews **92**, 95 (2018).

[3] U. Caldiño-Herrera, L. Castro, O. Jaramillo, J. Garcia, G. Urquiza, and F. Flores, *Small organic Rankine cycle coupled to parabolic trough solar concentrator,* in *4th International Seminar on ORC Power SystemsSeptember* (2017).

[4] E. Macchi, *Design criteria for turbines operating with fluids having a low speed of sound,* (Von Karman Institute for Fluid-dynamics, 1977) Chap. Closed Cycle Gas Turbines, Lecture Series 100.

[5] G. Angelino, M. Gaia, and E. Macchi, *A review of italian activity in the field of organic Rankine cycles,* in *International VDI Seminar* (1984) pp. 465–482.

[6] B. Minor, K. Kontomaris, and B. Hydutsky, *Nonflammable low gwp working fluid for organic Rankine cycles,* in *ASME Turbo Expo*, Vol. 3B (2014) p. 8.

[7] D. Bonalumi, P. Bombarda, and C. InvernizziInvernizzi, *Potential performance of environmental friendly application of ORC and flash technology in geothermal power plants,* in *IV International Seminar on ORC Power Systems* (2017).

[8] P. Colonna, E. Casati, C. Trapp, M. T., J. Larjola, T. Turunen-Saaresti, and A. Uusitalo, *Organic Rankine cycle power systems: from the concept to current technology, applications and an outlook to the future,* Journal of Engineering for Gas Turbines and Power **137**, 100801 (2015).

[9] W. Lang, P. Colonna, and R. Almbauer, *Assessment of waste heat recovery from a heavy-duty truck engine by means of an ORC turbogenerator,* Journal of Engineering for Gas Turbines and Power **135**, 042313 (2013).

[10] C. De Servi, L. Azzini, M. Pini, A. G. Rao, and P. Colonna, *Exploratory assessment of a combined-cycle engine concept for aircraft propulsion,* in *Proceedings of the 1st Global Power and Propulsion Forum - GPPF2017*, GPPF-2017-78 (2017) p. 11.

[11] U. Drescher and D. Brüggemann, *Fluid selection for the organic Rankine cycle (ORC) in biomass power and heat plants,* Applied Thermal Engineering **27**, 223 (2007).

[12] R. Bracco, S. Clemente, D. Micheli, and M. Reini, *Experimental tests and modelization of a domestic-scale ORC (Organic Rankine Cycle),* Energy **58**, 107 (2013).

[13] S. Declaye, S. Quoilin, L. Guillaume, and V. Lemort, *Experimental study on an open-drive scroll expander integrated into an ORC (Organic Rankine Cycle) system with R245fa as working fluid,* Energy (Article in press) **55**, 173 (2013).

[14] A. Borsukiewicz-Gozdur, *Experimental investigation of R227ea applied as working fluid in the ORC power plant with hermetic turbogenerator,* Applied Thermal Engineering **56**, 126 (2013).

[15] S. Quoilin, M. Van Den Broek, S. Declaye, P. Dewallef, and V. Lemort, *Techno-economic survey of organic Rankine cycle (ORC) systems,* Renewable and Sustainable Energy Reviews **22**, 168 (2013).

[16] P. Colonna, *Mini-orc turbogenerator: the upcoming leap forward?* in *3rd International Seminar on ORC Power Systems* (2015).

[17] J. Abbin, *Solar Total Energy Test Facility Project Test Summary Report: Rankine Cycle Energy Conversion Subsystem*, Tech. Rep. SAND-78-0396 (Sandia National Laboratories, 1978).

[18] L. DiNanno, F. DiBella, and M. Koplow, *An RC-1 Organic Rankine Bottoming Cycle for an Adiabatic Diesel Engine*, Tech. Rep. DOE/NASA/0302-1 (NASA, Lewis Research Center, 1983).

2

METHOD FOR THE PRELIMINARY FLUID DYNAMIC DESIGN OF HIGH-TEMPERATURE MINI-ORC TURBINES

The contents of this chapter appeared in:

S. Bahamonde, M. Pini, C. De Servi, and P. Colonna, *Method for the preliminary fluid dynamic design of high-temperature mini-ORC turbines*, J. Eng. Gas Turb. Power 139, 082606-01-14 (2017).

Widespread adoption of renewable energy technologies will arguably benefit from the availability of economically viable distributed thermal power conversion systems. For this reason, considerable efforts have been dedicated in recent years to R&D over mini organic Rankine cycle (ORC) power plants, thus with a power capacity approximately in the 3 – 50 kW *range. The application of these systems for waste heat recovery from diesel engines of long-haul trucks stands out because of the possibility of achieving economy of production. Many technical challenges need to be solved, as the system must be sufficiently efficient, light and compact. The design paradigm is therefore completely different from that of conventional stationary ORC power plants of much larger capacity. A high speed turbine is arguably the expander of choice, if high conversion efficiency is targeted, thus high maximum cycle temperature. Given the lack of knowledge on the design of these turbines, which depends on a large number of constraints, a novel optimal design method integrating the preliminary design of the thermodynamic cycle and that of the turbine has been developed. The method is applicable to radial inflow, axial and radial outflow turbines, and to superheated and supercritical cycle configurations. After a limited number of working fluids is selected, the feasible design space is explored by means of thermodynamic cycle design calculations integrated with a simplified turbine design procedure, whereby the isentropic expansion efficiency is prescribed. Starting from the resulting design space, optimal preliminary designs are obtained by combining cycle calculations with a 1D mean-line code, subject to constraints. The application of the procedure is illustrated for a test case: the design of turbines to be tested in a new experimental setup named ORCHID, which is being constructed at the Delft University of Technology. The first turbine selected for further design and construction employs siloxane MM (hexamethyldisiloxane,* $C_6H_{18}OSi_2$*), supercritical cycle, and the radial inflow configuration. The main preliminary design specifications are: power output equal to* 11.6 kW*, turbine inlet temperature equal to* 300 °C*, maximum cycle pressure equal to* 19.9 bar*, expansion ratio equal to* 72*, rotational speed equal to* 90 krpm*, inlet diameter equal to* 75 mm*, minimum blade height equal to* 2 mm*, degree of reaction equal to* 0.44*, estimated total-to-static efficiency equal to* 77.3 %*. Results of the design calculations are affected by considerable uncertainty related to the loss correlations employed for the preliminary turbine design, as they have not been validated yet for this highly unconventional supersonic and transonic mini-turbines. Future work will be dedicated to the extension of the method to encompass the preliminary design of heat exchangers and the off-design operation of the system.*

2.1. INTRODUCTION

Decentralized power conversion systems from renewable sources will arguably have a major influence on the global scenario, as they can contribute to the reduction of the environmental impact of traditional, large-scale, power plants [1]. Thermal systems based on the Organic Rankine Cycle (ORC) concept offer unique advantages: i) flexibility in terms of operating conditions, capacity, and part-load operation, ii) simplicity, iii) cost-effectiveness [2]. This technology is mature for power capacity ranging from hundreds of kW to few MW, and for the conversion of low-enthalpy geothermal reservoirs, biomass-based fuel, and waste heat. Know-how about the design of this type of power plants is therefore well established.

Recently, the large potential of mini-ORC turbogenerators (*m*ORC, 3 – 50 kW) has been rediscovered, after the conspicuous R&D activity of the seventies and the subsequent hiatus in interest due to the low cost of fossil fuels [2]. Waste heat recovery from long-haul truck engines by means of *m*ORC systems is currently attracting major R&D efforts. If large

market penetration will be achieved, opportunities for other widespread application of the technology will arise, e.g., distributed concentrated solar power (CSP) trigeneration, and distributed heat recovery.

If the temperature of the heat source is low, the net conversion efficiency of the system is bound to be low, and large heat transfer surfaces are needed; in case of solar radiation conversion, also large collection areas become mandatory. Their large capital cost negatively affects the economic viability of systems, more so if power capacity is low. If the thermal energy source is available at relatively high temperature (300 – 500 °C), like in the case of diesel engine exhaust, it seems therefore more reasonable to develop systems which can efficiently exploit the full thermodynamic potential, even if the high value of the maximum cycle temperature poses additional technological challenges. If the expander inlet temperature is in the 300 to 400 °C range, a volumetric machine cannot be adopted, because the corresponding large expansion ratio makes its realization impossible, or strongly penalizes its efficiency [3]. On the contrary, as discussed for example in Ref. [2], high-temperature *m*ORC systems can be realized with efficient turbo-expanders if the working fluid is made of complex organic molecules.

The design and construction of several high-temperature (> 250 °C) *m*ORC prototypes utilizing turbo-expanders is documented in the literature. For example, in the 70's, a 32 kW_e unit was tested at Sandia National Laboratories. Refrigerant R113 was chosen as working fluid, and the power block was connected to parabolic solar through collectors via an intermediate thermal oil loop. The system supplied at the same time electricity, heating and cooling [2]. Another example from the same period is the prototype realized at the Jet Propulsion Laboratory: a parabolic solar dish directly heated the working fluid up to 400 °C, toluene in this case. The measured solar-to-electric efficiency was 18%, while the power output was 16 kW_e [2]. A thorough investigation on waste heat recovery from a 240 kW heavy-duty truck diesel engine was sponsored by NASA in the 80's. An ORC system recovering thermal energy from the exhaust of a commercial engine was designed and built. The high-speed turbine was mechanically connected to the engine shaft, and the ORC system was capable of producing approximately 40 kW at maximum engine load, using a mixture of pentafluorobenzene and hexafluorobenzene as working fluid, and reaching peak temperatures of the order of 400°C at the turbine inlet [4, 5].

However, the advent of low oil prices made the products possibly resulting from these efforts economically unattractive. As a consequence, most experimental facilities were eventually shut down, and research programs interrupted, leaving a lack of consolidated experience about system and turbine design. Such know-how for the design of *m*ORC systems, and turbines in particular, is fundamental. The problem is very challenging, as it involves a much larger number of constraints and requirements, if compared to the design of large-capacity systems. For example, if the design of the turbine is concerned, the maximum inlet pressure is constrained by the minimum blade height, which is imposed by manufacturing or fluid dynamic limits. Therefore, the selection of the working fluid and the design of the thermodynamic cycle and of each component are tightly connected, and an integrated approach relying also on modern computational optimization would arguably be the method of choice. In this respect, some research has been recently conducted, but only for the case of large-capacity systems and with constraints pertinent to a preselected type of turbine, see, e.g., Ref. [6, 7].

This work concerns a computer-based method for the optimal preliminary fluid dynamic design of the turbine performed simultaneously with the optimal design of the ther-

modynamic cycle. The procedure is especially suitable for high-temperature *m*ORC systems. The mini-turbine is the most critical component to design, given the many constraints and their interaction with thermodynamic cycle parameters. Constraints on volume and weight strongly influence the design of the heat exchangers in case of mobile applications, but an automated preliminary design procedure encompassing the simultaneous optimization of fluid selection, thermodynamic cycle and components design is very complex and left for a successive stage of the investigation.

The design procedure described here requires the selection of the working fluid, of the turbine configuration (radial inflow, axial or radial outflow), assumes that the thermodynamic cycle is either superheated or supercritical with regeneration, and consists then in two steps. First, the space of feasible designs is scanned and delimited by performing design calculations of the thermodynamic cycle coupled with those of the turbine, subject to main constraints. However, the preliminary design calculation of the turbine is simplified, whereby the turbine isentropic efficiency is specified. Identifying the design envelope serves the purpose of guaranteeing robustness to the second step of the procedure leading to the optimal design of the turbine. This approach mitigates the problem of the lack of design paradigms and guidelines for high-temperature *m*ORC turbines. In the second step of the method, the calculation of the optimal thermodynamic cycle and turbine are fully coupled and the turbine total-to-static efficiency is determined with a mean-line procedure. The application of the method is illustrated with an exemplary case, namely the design of 10 kW *m*ORC turbines to be tested in the ORCHID setup currently under construction at the Delft University of Technology [8].

2.2. METHODS

The procedures constituting the optimal turbine design method have been coded into a general-purpose programming environment [9], and in an in-house Fortran program for the preliminary fluid dynamic design of turbines named zTURBO. In these procedures, thermophysical properties of fluids are calculated by means of a linked library implementing a variety of models for a large number of fluids and mixtures [10].

2.2.1. DESIGN SPACE

Any design optimization problem requires the definition of a suitable design space. An ill-defined design problem might prevent the optimizer algorithm from finding any solution, even suboptimal. For ORC turbines, variables like working fluid, degree of reaction and rotational speed are closely related. Therefore, the choice of the admissible values for one of these variables intrinsically determines the design space, thus the possible range of values for the other inputs to the problem. In case of the design of conventional turbines (gas turbines, steam turbines, turbocompressors etc.), knowledge and empirical rules provide the necessary bounds to the optimal design problem. The devised procedure overcomes this deficiency for *m*ORC turbines.

The simplified preliminary design of a turbine for a range of input variables and subject to constraints is accomplished by performing the thermodynamic cycle calculation and by applying fundamental turbomachinery relations. The process flow diagram of the system and an exemplary thermodynamic cycle in the $T-s$ diagram of the working fluid are shown in Figure 2.1. The inputs of the cycle calculations are listed in Table 2.1; the computation of the output is performed according to the standard sequence for a Rankine cycle that can

be found in textbooks, see, e.g. [11].

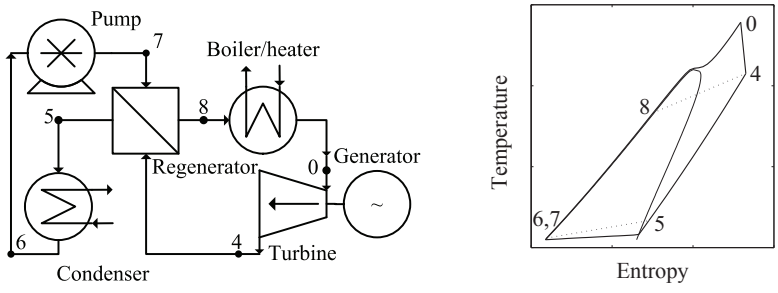

Figure 2.1: (a) Process flow diagram of an ORC system with regeneration. (b) Exemplary temperature-entropy thermodynamic diagram of a supercritical ORC cycle.

Table 2.1: Inputs required for the ORC thermodynamic cycle calculation.

Approximate net power	$\dot{W}_{\text{net}}$	Condensing temperature	T_6
Turbine inlet temperature	$T_0 = T_{\text{tit}}$	Regenerator pinch temperature	$\Delta T_{\text{pn,rg}}$
Pump adiabatic efficiency	η_{pm}	Pressure drop	ΔP_{tot}
Transmission efficiency	η_{me}	Maximum pressure	$P_7 = P_{\text{max}}$
Generator efficiency	η_{ge}	Turbine isentropic efficiency	$\eta_{\text{tr,ts}}$
Working fluid			

The maximum cycle pressure and the stage degree of reaction are the chosen degree of freedom of the problem. The procedure is briefly recalled here. A working fluid and a turbine configuration are selected, and the isentropic efficiency of the turbine specified. Assumptions in this case are: i) negligible change of kinetic energy of the fluid between the inlet and outlet of the turbine; ii) the difference between the flow angle and the blade angle at the outlet of blades is negligible, iv) the flow in the stator is isentropic. Figure 2.2 shows the velocity triangles at the rotor inlet and outlet. The adopted numbering for the stage locations is: (0) stator inlet, (1) stator outlet, (2) rotor inlet, (3) rotor outlet.

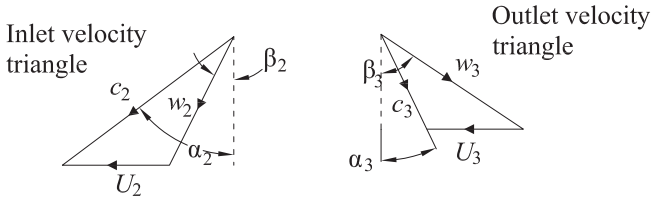

Figure 2.2: Turbine velocity triangles.

According to the angles convention shown in Figure 2.2, and recalling that the difference in fluid kinetic energy between the inlet and outlet of the stage is negligible, the Eulerian work is given by

$$\Delta h_{\text{ss,tr}} = U_2 c_{\theta,2} + U_3 c_{\theta,3}, \tag{2.1}$$

where $\Delta h_{ss,tr}$ is the static enthalpy drop across the turbine, U is the blade peripheral speed, and c is the flow velocity, whose tangential and meridional components are indicated by the subscripts θ and m, respectively. Combining (2.1) with appropriate relations for peripheral speed and velocity triangles, yields

$$\left(\frac{r_3}{r_2}\right)^2 U_2^2 - \left(c_{\theta,2} + w_{\theta,3}\frac{r_3}{r_2}\right) U_2 + \Delta h_{ss,tr} = 0. \tag{2.2}$$

U_2 can thus be obtained from (2.2), once all the other parameters are assigned values, depending on the selected stage configuration. Notice that (2.2) is quadratic, therefore it allows for two solutions. Further analysis shows that one of the two solutions is nonphysical. The enthalpy drop $\Delta h_{ss,tr}$ in (2.2) is obtained from the thermodynamic cycle calculation as

$$\Delta h_{ss,tr} = \eta_{tr,is}(h_0 - h_{3,is}), \tag{2.3}$$

where $\eta_{tr,is}$ is the prescribed turbine efficiency, h_0 is the entalphy at the turbine inlet, and $h_{3,is}$ is the enthalpy at the turbine outlet, assuming isentropic expansion. The absolute velocity at the stator outlet is a function of the given degree of reaction and of the enthalpy drop, as in

$$c_2 = \sqrt{2\,(1-R)\,\Delta h_{ss,tr}}. \tag{2.4}$$

The parameters in (2.2) depend on the stage configuration and their calculations is as follows.

RADIAL INFLOW TURBINE STAGE

Figure 2.3 shows a schematic diagram of the cross section of a radial inflow turbine (RIT). Additional expressions can be derived from the velocity triangles, leading to

$$w_{\theta,3} = \tan(\beta_3)\, c_{m,3}, \tag{2.5}$$

$$c_{m,3} = \phi U_2, \tag{2.6}$$

where β_3 is the rotor outlet angle, and ϕ is the axial exit flow coefficient, which, when designing a RIT stage, is commonly specified [12]. Combining (2.5), (2.6), and (2.2) gives

$$\left[\left(\frac{r_3}{r_2}\right)^2 - \tan(\beta_3)\phi\frac{r_3}{r_2}\right] U_2^2 - c_{\theta,2} U_2 + \Delta h_{ss,tr} = 0. \tag{2.7}$$

The peripheral speed U_2 is computed from (2.7), once the remaining parameters are specified with values reccommended in the literature. The rotor radius r_2 is then obtained by means of the mass conservation equation applied at the turbine outlet [12], hence

$$r_2 = \sqrt{\frac{\dot{m}}{\rho_3 \phi U_2 \pi \left(\frac{r_{s,3}}{r_2}\right)^2 \left(1 - \left(\frac{r_{h,3}}{r_{s,3}}\right)^2\right)}}, \tag{2.8}$$

where $r_{s,3}$ is the shroud radius at rotor outlet, $r_{h,3}$ is the hub radius at rotor outlet, and ρ_3 is the fluid density at the rotor outlet. The rotational speed Ω is a function of r_2 and U_2. Finally, the blade height at the inlet of the rotor can be calculated with the mass conservation equation, giving

$$b_2 = \frac{\dot{m}}{2\pi r_2 \rho_2 c_{m,2}}, \tag{2.9}$$

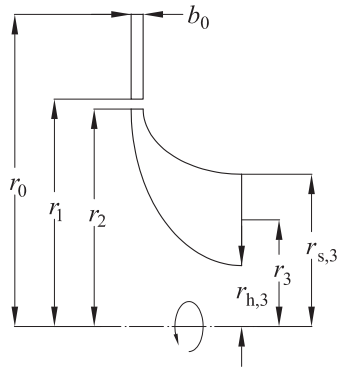

Figure 2.3: Meridional channel of a radial inflow turbine.

where ρ_2 is the density at rotor inlet. The density used in equations (2.8) and (2.9) is obtained from the thermodynamic states at the inlet and outlet of the turbine and from the degree of reaction. Equations (2.4), (2.7), (2.8), and (2.9) form a system whose unknown and specified variables are listed in Table 2.2. The unknowns are all related to the rotor inlet and are: the absolute flow velocity, the peripheral speed, the radius, and the blade height, while the other outputs can be calculated from simple relations to the unknowns.

Table 2.2: Inputs/outputs of Equations (2.3), (2.4), (2.7), (2.8), and (2.9). This system of equations constitutes the constant-efficiency design method for a RIT stage.

Inputs		**Outputs**	
Isentropic efficiency	$\eta_{tr,is}$	Radius	$r_{0..3}$
Inlet to outlet stator radius ratio	r_0/r_1	Blade height	$b_{0..3}$
Outlet stator to inlet rotor radius ratio	r_1/r_2	Rotational speed	Ω
Outlet shroud to inlet rotor radius ratio	$r_{s,3}/r_2$	Blade peripheral speed	$U_{2,3}$
Outlet hub to shroud rotor radius ratio	$r_{h,3}/r_{s,3}$	Absolute flow velocity	$c_{0..3}$
Stator outlet angle	α_2	Relative flow velocity	$w_{2,3}$
Rotor outlet angle	β_3	Absolute flow Mach number	$M_{ab,2,3}$
Degree of reaction	R	Relative flow Mach number	$M_{rl,2,3}$
Axial flow coefficient	ϕ	Specific work	$\Delta h_{ss,tr}$
Working fluid mass flow	$\dot{m}$	Power	$\dot{W}_{tr}$
Inlet/oulet static pressure	P_0, P_3	Rotor inlet angle	β_2
Inlet temperature	$T_0 = T_{tit}$		
Working fluid			

RADIAL OUTFLOW AND AXIAL TURBINE STAGES

Figure 2.4 displays a simple diagram of the cross section of either a radial outflow turbine (ROT) or an axial turbine (AXT), depending on the specification of the axis of rotation. For simplicity the design calculation of multi-stage turbines is performed by adopting the *repeating stage* criterion. Thus, the rotor inlet and outlet velocity triangles are equal, i.e.,

$$c_{m,2} = c_{m,3}, \tag{2.10}$$

$$\alpha_2 = \beta_3. \tag{2.11}$$

Note though, that in a ROT the peripheral speed must change with the radius, hence (2.10) cannot hold rigorously. Nonetheless, to a first approximation, the difference between the

peripheral speed at rotor inlet and outlet is negligible, because of the small size of the radial chord in *m*ORC turbines. The repeating stage criterion also requires that the total pressure ratio is equally distributed among the stages, thus

$$\Pi_{sg} = \Pi_{tot}^{1/N_{sg}}, \tag{2.12}$$

where Π_{sg} is the stage pressure ratio, Π_{tot} is the total pressure ratio, and N_{sg} the number of stages.

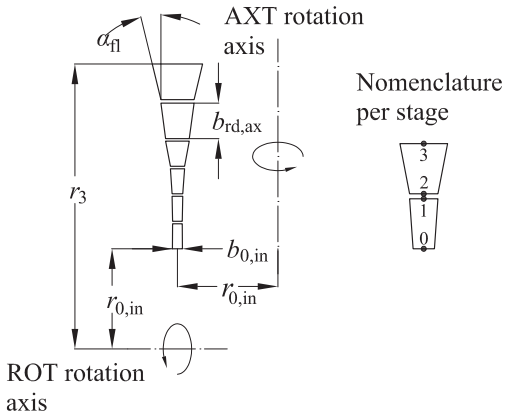

Figure 2.4: Meridional channel for a radial outflow and axial turbine.

By combining equations (2.2), (2.10), and (2.11), it is possible to obtain another equation, valid only for ROT and AXT stages, namely

$$\left(\frac{r_3}{r_2}\right)^2 U_2^2 - \left(c_{\theta,2} + c_{\theta,2}\frac{r_3}{r_2}\right) U_2 + \Delta h_{ss,tr} = 0. \tag{2.13}$$

This equation allows to calculate U_2, if all the parameters have specified values. The rotational speed is a function of U_2 and r_2. The blade height at the inlet of the rotor is given by

$$b_1 = \frac{\dot{m}}{2\pi(r_0 + b')\rho_1 c_{m,1}}, \tag{2.14}$$

where b' is the stage radial chord, which is equal to the blade chord b_{rd} for ROTs, and zero for AXTs. Equations (2.4), (2.13), and (2.14) constitute a system of algebraic equations. Table 2.3 reports the inputs and the outputs of the simplified turbine design procedure.

Equations (2.13) and (2.7) are quadratic in U_2. For the ROT/AXT case, the roots are real if condition

$$R \leq 1 - \frac{2\,(r_3/r_2)^2}{\sin^2(\alpha_2)\,(1 + r_3/r_2)^2} \tag{2.15}$$

is satisfied. Equation (2.7), valid for the RIT, leads to a similar condition. Ultimately, the maximum degree of reaction depends on the chosen design parameters.

Table 2.3: Inputs/outputs of Equations (2.3), (2.4), (2.13), and (2.14). This system of equations constitutes the constant-efficiency design method for a ROT or AXT stage.

Inputs		**Outputs**	
Isentropic efficiency	$\eta_{\text{tr,is}}$	Radius	$r_{0..3}$
Inlet radius	$r_{0,\text{in}}$	Blade height	$b_{0..3}$
Radial/axial chord	$b_{\text{rd,ax}}$	Rotational speed	Ω
Stator outlet angle	α_2	Blade peripheral speed	$U_{2,3}$
Rotor outlet angle	β_3	Absolute flow velocity	$c_{2,3}$
Degree of reaction	R	Relative flow velocity	$w_{2,3}$
Working fluid mass flow	$\dot{m}$	Absolute flow Mach number	$M_{\text{ab},2,3}$
Inlet/outlet static pressure	$P_{0,3}$	Relative flow Mach number	$M_{\text{rl},2,3}$
Inlet temperature	T_0	Specific work	$\Delta h_{\text{ss,tr}}$
Number of stages	N_{sg}	Power	$\dot{W}_{\text{tr}}$
Working fluid			

OUTPUT

The outcome of a design space calculation is shown in Figure 2.5. Such chart is obtained by varying the maximum cycle pressure and the degree of reaction between specified values, and by specifying the input variables introduced in Tables 2.1, 2.2 and 2.3. The chart provides reliable indication about the maximum and minimum rotational speed and diameter.

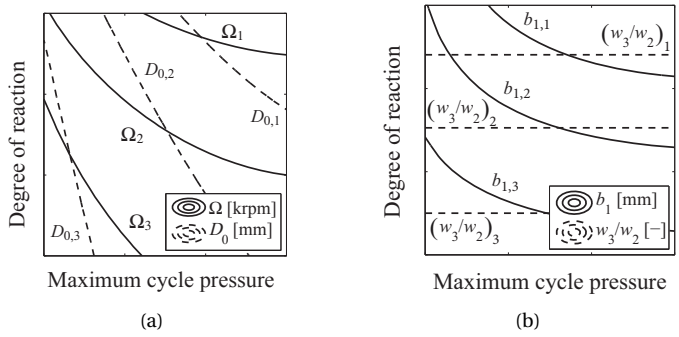

Figure 2.5: Exemplary contour plot with (a) the rotational speed Ω and the turbine inlet diameter D_0, and (b) the blade height at stator outlet and the rotor flow acceleration, as a function of the maximum pressure P_{max} and the degree of reaction R.

2.2.2. OPTIMAL DESIGN

The second step of the design method is implemented by coupling a well know optimizer [13, 14] with the thermodynamic cycle calculation and with zTURBO, an in-house mean-line code for design and performance estimation of turbines. The objective function of the optimization can be the net system efficiency, the net power output or other values of interest.

The reader is referred to Ref. [15] for details on the mean-line code. The loss models available in zTURBO are listed in Table 2.4. Note that windage losses in radial inflow ma-

chines are neglected, because their contribution seems to be not influential according to recent studies related to similar applications [16].

Table 2.4: Models employed in the meanline code zTURBO.

	RIT	ROT, AXT
Profile, secondary and tip clearance loss	Glassman [17], Baines [18]	Traupel [19]
Incidence losses	Wasserbauer and Glassman [20]	—
Optimum incidence angle	Stanitz (adapted for turbines) [12, 21]	—
Flow angles at row outlet	Osnaghi [22] (supersonic)	Sawyer [23] (trans.)
Throat opening in converging-diverging nozzles	Deich et al. [24]	—
Supersonic mixing losses	Osnaghi [22]	—

Table 2.5 itemizes the inputs zTURBO requires. Importantly, in the case of the axial turbine, the meridional flow diameter is allowed to grow in order to accommodate for the increase in volumetric flow.

Table 2.5: Inputs required by zTURBO, the 1D meanline code providing the preliminary fluid dynamic design of *m*ORC turbines.

RIT		ROT, AXT	
Tip clearance	t_{cl}	Tip clearance	t_{cl}
Trailing edge thickness	t_{te}	Trailing edge thickness	t_{te}
Inlet to outlet stator radius ratio	r_0/r_1	Stage gap	t_{rw}
Outlet stator to inlet rotor radius ratio	r_1/r_2	Inlet blade height	$b_{0,in}$
Inlet blade height	$b_{0,in}$	Inlet radius	r_0
Inlet radius	r_0	Blade chord	$b_{ax,rd}$
Rotational speed	Ω	Rotational speed	Ω
Rotor outlet blade angle	β_3	Outlet stator blade angle	α_2
Degree of reaction	R	Outlet rotor blade angle	β_3
Inlet/outlet static pressure	$P_{0,3}$	Degree of reaction	R
Inlet temperature	T_0	Number of stages	N_{sg}
Working fluid mass flow	$\dot{m}$	Working fluid mass flow	$\dot{m}$
		Inlet/outlet static pressure	P_0, P_3
		Inlet temperature	T_0
		Stator inlet to outlet mean radius ratio*	$r_{out,st}/r_{in,st}$
		Stator inlet to outlet mean radius ratio*	$r_{out,rt}/r_{in,rt}$

* Only applicable to AXTs.

2.3. IMPLEMENTATION

Figure 2.6 shows the flow chart of the design method (step 1 and step 2) as implemented in the code. The first step of the method, the integration of the thermodynamic cycle calculation and the simplified turbine design method (prescribed isentropic efficiency), can be expressed by means of a vector function

$$\Upsilon = f(\mathbf{X}_{cyc}, \mathbf{Z}_{tr}), \tag{2.16}$$

where $\mathbf{X}_{cyc}$ and $\mathbf{Z}_{tr}$ are vectors containing the input variables related to the turbine preliminary design (see Tab. 2.2 and 2.3) and to the system operating conditions (see Tab. 2.1), respectively.

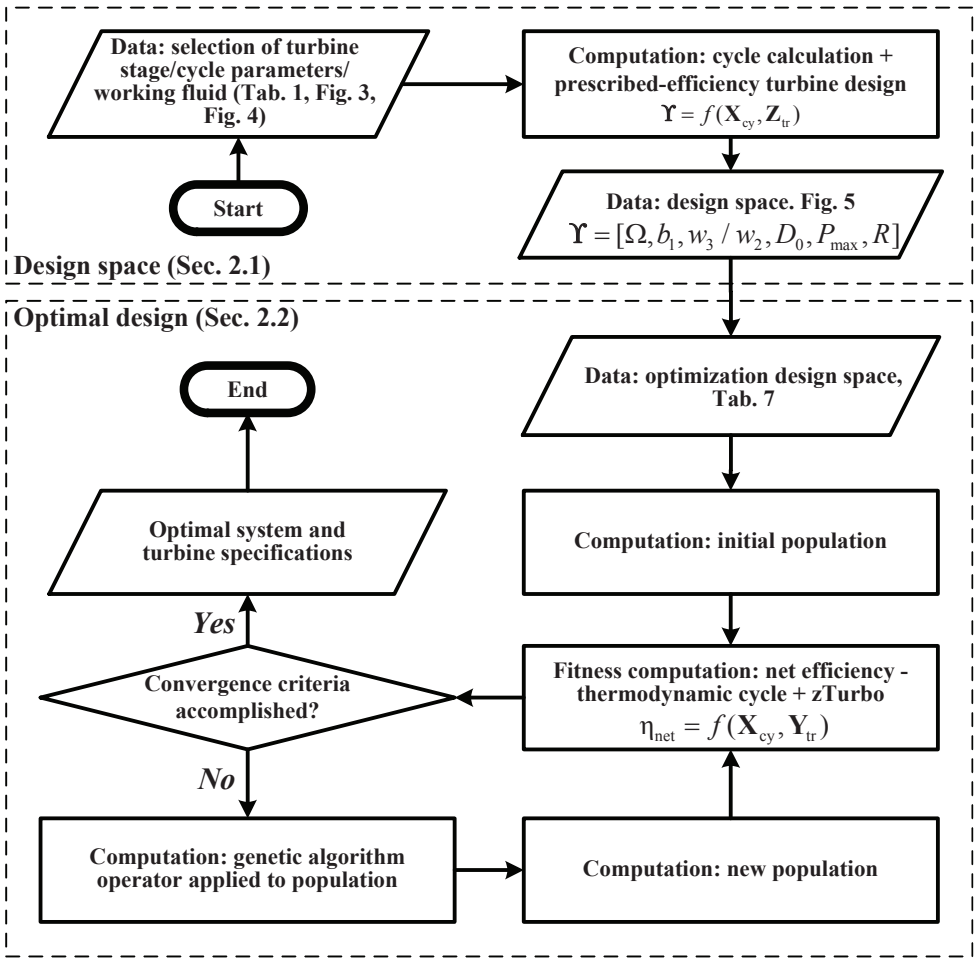

Figure 2.6: Flow chart illustrating the implementation of the design optimization method.

The solution of (2.16) is a vector containing turbine operating and geometrical variables, which are then used to infer the bounds of the design space, i.e.,

$$\Upsilon = [\Omega\,,\, b_1\,,\, M_{2,\mathrm{rl}}\,,\, \text{etc.}]. \tag{2.17}$$

The main variables of interest are Ω, b_1, D_0, and, in case of RIT, w_3/w_2. The program plots these variables, together with the input maximum cycle pressure and degree of reaction, in charts like the one in Fig. 2.5 providing visual information about the design space.

The second step of the method consists in solving the constrained optimization problem

$$\begin{aligned} &\text{maximize} && \eta_{\mathrm{net}} = \Psi(\mathbf{X}_{\mathrm{cyc}}, \mathbf{Y}_{\mathrm{tr}}), \\ &\text{subject to} && \Phi_{\mathrm{mn}}(\mathrm{i}) \le \Phi(\mathrm{i}) = \Psi(\mathbf{X}_{\mathrm{cyc}}, \mathbf{Y}_{\mathrm{tr}}) \le \Phi_{\mathrm{mx}}(\mathrm{i}), \\ &\text{where} && \mathrm{i} = 1\,,\, 2\,,\, \ldots \text{ Number of constraints.} \end{aligned} \tag{2.18}$$

In this case, $\mathbf{Y}_{tr}$ is a vector containing the ZTURBO input data listed in Tab. 2.5). Function Ψ represents the integration of the thermodynamic cycle and ZTURBO calculations, and it provides an array with the ensemble of all the possible cost functions (e.g., system net efficiency η_{net}) and constraints Φ(i) (e.g., maximum blade height at first stator outlet b_1).

Due to the large amount of design variables (between six and fifteen, depending of the turbine configuration), and in order to avoid the convergence to local solutions, an optimizer based on a genetic algorithm has been adopted [14]. In addition, the code has been parallelized in order to run on a multi-core computer [25]. An exemplary turbine design optimization takes approximately three hours on a 64-bit computer, running the Microsoft Windows operating system, and equipped with a 3.60 GHz processor with eight virtual cores and 16 GB of RAM.

2.4. APPLICATION, RESULTS AND ANALYSIS

In order to illustrate the application of the design method in detail, the preliminary design of *m*ORC turbines for the ORCHID setup is considered [8]. One of the main goals of the setup is to provide performance data of mini turbines operating at high temperature and with different working fluids. The nominal power output is set to approximately 10kW, as this power level is compatible with the expected specification for the heat recovery system of long-haul truck diesel engines.

The fluids that are initially considered are MM (hexamethyldisiloxane, $C_6H_{18}OSi_2$) and PP_2 (perfluoromethylcyclohexane, C_7F_{14}). They were chosen because their molecular complexity is high as required by this application (high temperature, small power capacity), their thermal stability is adequate, they are not toxic, and their flammability is either low (MM) or zero (PP_2). In addition, their condensing pressure at the chosen minimum cycle temperature (50 °C) is sufficiently high, i.e., 0.17 bar for MM, and 0.43 bar for PP_2. Unfortunately the Global Warming Potential of PP_2 is very high, nonetheless PP_2 is possibly the best fluid from all other standpoints, and thus very attractive for experimental work aimed at devising general theory on *m*ORC turbine performance. Table 2.6 presents the system specifications.

Table 2.6: Constant system specifications used in the design of mini-ORC turbogenerator.

$\dot{W}_{net}$	kW	10.0	η_{ge}	%	96.5	η_{me}	%	92.0
T_0	°C	300.0	T_6	°C	50.0	$\Delta T_{pn,rg}$	°C	20.0
η_{pm}	%	65.0	ΔP_{tot}	%	1.0	Fluid		MM, PP_2

The discussion of the results treated here pertains mostly to calculations concerning systems employing MM as the working fluid, since the results of calculations of systems employing PP_2 as working fluid are qualitatively similar.

2.4.1. DESIGN SPACE

Table 2.7 shows the turbine parameters selected for the design of the RIT. The selection of their values is mostly based on design recommendations or manufacturing constraints. For instance, the radius ratio $r_{s,3}/r_2$ should not exceed 0.7, in order to avoid excessive curvature of the shroud. Likewise, $r_{h,3}/r_{s,3}$ should be higher than 0.4, in order to avoid flow blockage at the hub [26]. Additionally, the ratio r_0/r_1 and r_1/r_2, have been chosen in such a way that the stator blade height vs. chord is in accordance with design practice. The value of the

isentropic turbine efficiency is set equal to 80 %, as expected from considerations taking into account information from the literature, e.g. [4], the small size of the expander and the high expansion ratio.

Table 2.7: Fixed parameters adopted for the determination of the RIT design space.

$\eta_{tr,is}$	%	80.0	$r_{s,3}/r_2$	–	0.7	$r_{h,3}/r_{s,3}$	–	0.4
r_0/r_1	–	1.3	α_2	°	80.0	β_3	°	50.0
r_1/r_2	–	1.02	ϕ	–	0.30			

Figure 2.7 displays the design space referring to a RIT for the ORCHID setup with MM as working fluid. Figure 2.7a presents the corresponding rotational speed and inlet diameter. For a given cycle maximum pressure, an increase of degree of reaction decreases the flow velocity (and its tangential component $c_{\theta,2}$) at stator outlet. Equation (2.1) shows that, given that the Eulerian work is a datum, the peripheral speed U_2 must increase. Besides, according to (2.8), a larger U_2 leads to smaller rotor inlet diameter D_2. As a consequence, and due to constant radius ratios r_0/r_1 and r_1/r_2, D_0 decreases with higher R. Finally, the rotational speed ($\Omega = U_2/r_2$) is larger for larger degree of reaction.

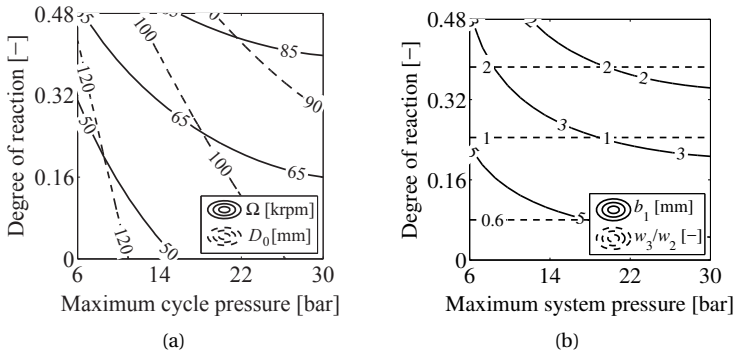

Figure 2.7: Design space for a 10 kW radial inflow turbine, using MM as the working fluid.

Similarly, for a given degree of reaction, a higher P_{max} increases the fluid acceleration, thus resulting in a larger rotational speed. A higher cycle maximum pressure also increases the specific work, thus reduces the required mass flow rate and the inlet diameter, see (2.8).

Figure 2.7b shows a contour map of the minimum blade height b_1 and of w_3/w_2, the ratio between relative flow velocity at the rotor inlet and outlet. While b_1 is used as a design input for the optimization, w_3/w_2 must be constrained according to recommendations for the preliminary design of radial inflow turbines [12, 26, 27]. For a fixed maximum cycle pressure, a higher R results in a decrease of both $c_{m,2}$ and D_2, and in an increase of ρ_2. Although the three variables influence b_1, see (2.9), the density effect is dominant, leading to an inversely proportional relation between R and b_1.

Increasing the degree of reaction increases the acceleration in the rotor, hence R is proportional to w_3/w_2. However, P_{max} has no effect on w_3/w_2, as it can be proven that the flow acceleration is solely a function of the degree of reaction, by combining equations (2.8) and (2.4) with the definition of the flow coefficient ($\phi = c_{m,3}/U_2$) and trigonometrical relations from the velocity triangles in Fig. 2.2.

The combined effect of b_1 and w_3/w_2 has relevant implications on the turbine design, because it limits the cycle maximum pressure. For instance, if a manufacturing constraint is $b_1 \geq 2$ mm, and a fluid dynamic design constraint is $w_3/w_2 \geq 2.0$, the highest P_{max} is approximately 22 bar, since higher values would lead either to an excessively short blade or to excessively small rotor flow acceleration.

Design space calculations with the same input, but considering PP_2 as the working fluid, lead to results with similar trends. However, given that PP_2 features higher critical pressure and higher molecular complexity if compared to MM, the enthalpy drop over expansion is smaller, thus the mass flow rate larger. This further results in a design space whereby the maximum cycle pressure is higher, and the rotational speed lower.

Table 2.8 lists the input parameters for the design space calculation in case ROT and AXT are the chosen configurations. Since multi-stage configurations for both machines are considered, assumptions concerning the load distribution among the stages and the geometry are to be made; more specifically:

i) the number of stages is set to three, in order to attain transonic flow regime within the blade passages, with the minimum number of stages. The choice results from trial calculations using the simplified design method;

ii) the expansion ratio is equally distributed among the stages. As discussed in the following, the blade height at the outlet of the first stator constraints the maximum turbine inlet pressure. Although different expansion ratios per stage might help increasing the stator outlet blade height [28], a sensitivity analysis showed that this does not hold for the current study case;

iii) the value of the inlet diameter is set to 25 mm. Lower values might reduce the inlet flow area to levels that require unacceptably high fluid velocities. On the other hand, larger diameters would require unfeasible small blades at the outlet of the first stator. Also in this case, some trial calculations are needed in order to identify the proper value for D_0;

iv) the maximum blade outlet angles are fixed and they are $\alpha_2 = \beta_3 = 75°$, according to design practice;

v) finally, manufacturing and operational constraints suggest a blade chord (axial or radial) of $b_{ax,rd} = 5$ mm.

Table 2.8: Fixed parameters adopted for the determination of the ROT and AXT design space.

$\eta_{tr,is}$	%	80.0	α_2	°	75.0	$D_{0,in}$	m	0.025
N_{sg}	–	3	β_3	°	75.0	$b_{ax,rd}$	m	0.005

Recent work [28] demonstrated that, in case of *m*ORC turbines, the fluid dynamic design of the first stage is the most critical and limiting as far as ROT and AXT are concerned, therefore design space calculations are restricted to the first stage. In particular, Figure 2.8 shows the contour maps of the rotational speed Ω and blade height at stator outlet b_1.

As in the RIT case, higher P_{max} and R result in higher rotational speed. Additionally, for a given pressure ratio, a higher R increases ρ_2 and decreases $c_{m,2}$, and both variables affect the calculation of b_1, see (2.14). As a consequence, the blade height at rotor inlet is

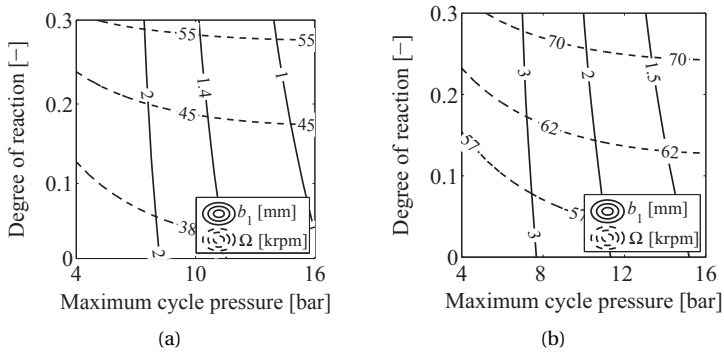

Figure 2.8: Design space for a 10 kW radial outflow (a) and axial (b) turbine, using MM as the working fluid.

almost independent from the degree of reaction. A further consequence is therefore that the constraint on the blade height unequivocally determines the maximum cycle pressure. For example, if manufacturing requires that $b_1 \geq 2$ mm, then the maximum value of $P_{\max}$ is approximately 8 bar.

Figure 2.8b reports the contour map of Ω and b_1 for the AXT. The trends are similar to those found for the ROT. However, the flow area of an AXT does not inherently increase as is the case in the ROT, thus it demands for higher blade height in order to accommodate for the increasing volumetric flow. A higher blade height implies also the corresponding maximum $P_{\max}$ is higher if compared to the ROT, 12 bar in this case. Another difference between ROT and AXT is that, for the same pressure ratio, the rotational speed of the AXT is higher than that of the ROT. This is due to the fact that the meridional diameter at the outlet of the AXT rotor is smaller compared to that of the ROT.

Despite the intrinsic limitations of the constant turbine efficiency method, its application reveals remarkable features inherent to the design of *m*ORC systems, i.e., that the cycle maximum pressure can be limited by a manufacturing constraint of the turbine, namely the minimum blade height, which, in turn, largely depends on the turbine configuration.

2.4.2. OPTIMAL DESIGN

Turbine maximum and minimum degree of reaction, inlet diameter, rotational speed, and maximum cycle pressure are selected based on the examination of Figures 2.7 and 2.8. Table 2.9 presents the information used to set up the turbine design optimization. Some of the input parameters of the turbine design are selected as follows

i) absolute tip clearance, $t_{\text{cl}} = 0.1$ mm; trailing edge thickness relative to the throat width, $t_{\text{te}} = 0.1 \cdot o_{\text{to}}$; ROT and AXT gaps between blade cascades, $t_{\text{rw}} = 0.1 \cdot b_{\text{ax,rd}}$. These choices stem from considerations on manufacturing capability and cost.

ii) The lenght of the ROT and AXT chords is the same per stage, as common in practice [28].

Furthermore, in order to guarantee that the fluid flow in the rotor is subsonic, the relative Mach number is set to a maximum value of 0.85. The flaring angle is limited to 15°, in

Table 2.9: Inputs for the global optimization, with MM as the working fluid: constant parameters, design space, and constraints. The values in parenthesis refer to PP_2.

RIT		ROT		AXT	
Constant parameters					
$t_{cl} = 0.1$	mm	$t_{cl} = 0.1$	mm	$t_{cl} = 0.1$	mm
$t_{te} = 0.1 \cdot o_{to}$	mm	$t_{te} = 0.1 \cdot o_{to}$	mm	$t_{te} = 0.1 \cdot o_{to}$	mm
$r_0 / r_1 = 1.3$	–	$t_{rw} = 0.1 \cdot b_{ax}$	mm	$t_{rw} = 0.1 \cdot b_{ax}$	mm
$r_1 / r_2 = 1.02$	–	$b_{0,in} = 2.0$	mm	$b_{0,in} = 2.0$	mm
$b_{0,in} = 2.0$	mm	$N_{sg} = 3$	–	$N_{sg} = 3$	–
		$\Pi_{sg} = \Pi_{tot}^{1/N_{sg}}$	–	$\Pi_{sg} = \Pi_{tot}^{1/N_{sg}}$	–
Design space					
$5 \le P_{max} \le 22\,(34)$	bar	$5 \le P_{max} \le 11\,(15)$	bar	$5 \le P_{max} \le 15\,(25)$	bar
$60 \le D_{in} \le 120$	mm	$20 \le D_{in} \le 30$	mm	$20 \le D_{in} \le 30$	mm
$60\,(30) \le \Omega \le 100\,(80)$	krpm	$30 \le \Omega \le 60\,(40)$	krpm	$50\,(30) \le \Omega \le 120\,(80)$	krpm
$0.3 \le R \le 0.7$	°	$0.0 \le R \le 0.7$	–	$0.0 \le R \le 0.7$	–
$45 \le \beta_3 \le 60$	–	$55 \le \beta_3 \le 75$	°	$55 \le \beta_3 \le 75$	°
$1.5 \le r_2 / r_3 \le 2.5$	–	$55 \le \alpha_2 \le 75$	°	$55 \le \alpha_2 \le 75$	°
		$5 \le b_{rd} \le 10$	mm	$5 \le b_{ax} \le 30$	mm
				$1 \le r_{ou,st} / r_{in,st} \le 1.30$	–
				$1 \le r_{ou,rt} / r_{in,rt} \le 1.30$	–
Constraints					
$\alpha_2 \le 80.0$	–	$-15 \le \alpha_{fl} \le 15$	°	$-15 \le \alpha_{fl} \le 15$	°
$M_{rl,2} \le 0.85$	–	$M_{2,rl} \le 0.85$	–	$M_{2,rl} \le 0.85$	–
$r_{h,3} / r_{s,3} \ge 0.4$	–	$b_{0..3} \ge 2.0$	mm	$b_{0..3} \ge 2.0$	mm
$r_{s,3} / r_2 \le 0.7$	°			$D_i - b_i \ge 20$	mm
$w_3 / w_2 \ge 2.0$	–				

order to avoid flow separation at the end walls. Finally, the minimum hub diameter in axial machines is constrained to be at least the minimum inlet diameter, i.e., $D_i - b_i \ge 20$ mm.

The optimal solution of the design problem, calculated by the genetic algorithm in case MM is the working fluid, gives

i) ROT: $\eta_{net,opt} = 18.9$ %, $P_{7,opt} = 7.8$ bar;

ii) AXT: $\eta_{net,opt} = 21.3$ %, $P_{7,opt} = 10.5$ bar;

iii) RIT: $\eta_{net,opt} = 22.5$ %, $P_{7,opt} = 19.9$ bar.

The optimal values strongly depend on the turbine type, and the RIT configuration allows to achieve the maximum net system efficiency in all cases, followed by the AXT and ROT. The results in case PP_2 is the working fluid feature the same trend. Figure 2.9 shows the $T - s$ diagrams of the optimized *m*ORC systems operating with MM as working fluid, and for the three turbine configurations; Table 2.10 presents the corresponding system specifications.

The duty of the heat exchangers and their UA values are similar, thus, at least for this stationary application, their size is possibly not a deciding factor. The difference between the output power and net efficiency of the systems operating with the AXT and the RIT is rather small, considering the level of approximation of the calculations. However, the single-stage RIT configuration is considerably simpler than the three-stage axial configuration, thus possibly less expensive. The maximum pressure of the cycle employing a RIT is

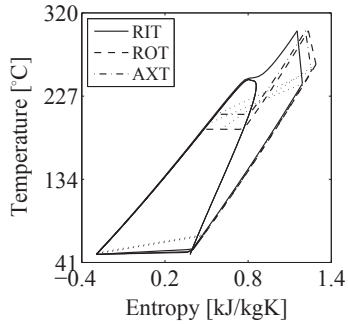

Figure 2.9: $T-s$ diagram of the thermodynamic cycles corresponding to the optimized *m*ORC systems operating with MM as working fluid. Thermodynamic cycle computed with $\Delta T_{\mathrm{pn,cn}} = 20.0$ K

Table 2.10: System specifications for the optimized *m*ORC systems operating with MM as working fluid. Information for the calculation of the UA values: heater hot side fluid: Therminol66 at 350 °C; $\Delta T_{\mathrm{pn,hr}} = 20.0$ K; condenser cold side fluid: water at 20 °C; $\Delta T_{\mathrm{pn,cn}} = 20.0$ K.

		ROT	AXT	RIT
Maximum pressure	bar	7.8	10.5	19.9
Net efficiency	%	18.9	21.3	22.5
Net power output	kW	8.6	9.6	9.7
Heater power - UA	kW - kW/K	46.9 - 0.9	46.6 - 0.8	46.2 - 1.0
Regenerator power - UA	kW - kW/K	52.8 - 1.3	48.4 - 1.2	42.5 - 1.2
Condenser power - UA	kW - kW/K	37.0 - 1.5	35.6 - 1.4	34.5 - 1.2
Turbine efficiency	%	68.7	76.7	77.3

slightly supercritical, $P_{\mathrm{r}} = 1.02$, and this could be advantageous because, contrary to solutions whereby the cycle is superheated, no phase transition would occur in the evaporator and regenerator.

Figure 2.10 shows the net conversion efficiency of the system as a function of the maximum cycle pressure, and the type of turbine and the working fluid. This type of chart is also an output of the design optimization code.

As can be observed, η_{net} monotonically increases for increasing maximum cycle pressure, up to the point at which the decrease of turbine efficiency is not compensated by the positive thermodynamic effect of the maximum cycle pressure increase. The maximum cycle pressure always results from the constraints on the blade height, i.e., $b_1 < 2$ mm. Only for the RIT, the maximum cycle pressure is determined also by the constraint on the flow acceleration, namely $w_3/w_2 > 2.0$. Note that the maximum cycle pressure in case PP_2 is the working fluid is considerably higher than in case of MM, see Fig. 2.10b, because the critical pressure of PP_2 is considerably higher than that of MM. Moreover, given the larger molecular complexity of PP_2, the enthalpy drop over expansion is smaller, and, as a consequence, the mass flow is larger.

OPTIMAL TURBINES

Figure 2.11 displays the main turbine specifications corresponding to the global optima shown in Figure 2.9 and referring to the design of the ORCHID setup, in case MM is the working fluid.

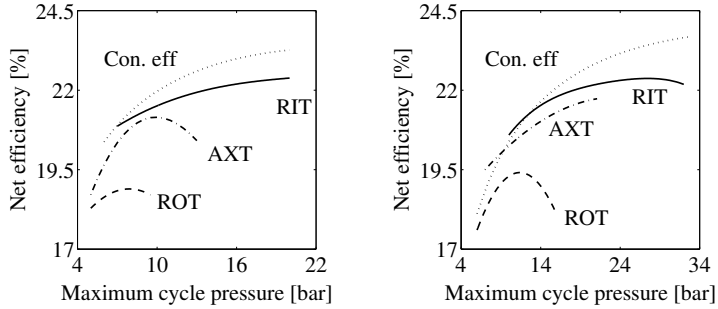

Figure 2.10: Net system efficiency as a function of the maximum cycle pressure for systems operating with (a) MM and (b) PP_2. Each point in the charts represent an optimal solution of the design problem for the given maximum cycle pressure. The dotted line (Con. eff) corresponds to the result of a thermodynamic cycle calculation with fixed turbine isentropic efficiency, $\eta_{tr,is} = 80.0$ %.

The effects of small blade heights and flow compressibillity can be analyzed by means of the size parameter κ, the volumetric expansion ratio ς, and the specific speed Ω_s [29, 30]

$$\kappa = \frac{\sqrt{\dot{V}_{out}}}{\sqrt[4]{\Delta h_{tr,is}}}, \tag{2.19}$$

$$\varsigma = \frac{\dot{V}_{out}}{\dot{V}_{in}}, \tag{2.20}$$

$$\Omega_s = \Omega_{rad} \frac{\sqrt{\dot{V}_{out}}}{\Delta h_{tr,is}^{3/4}}, \tag{2.21}$$

where $\dot{V}$ is the volumetric flow, and $\Delta h_{tr,is}$ is the turbine isentropic enthalpy drop. Low κ values imply large tip clearance loss and potential Reynolds effects. Large ς is generally associated with compressibillity effects, i.e., high Mach numbers and large flow area variations, which also deteriorate the stage performance.

Coincidentally, the value of ς calculated for the ROT and AXT for each stage is close to three, and this is the value corresponding to one of the cases treated in Ref. [31] in detail, which corroborates the results of the analysis discussed here. Conversely, the large volumetric expansion ratio (≈ 90) estimated for the RIT solutions is largely above the values considered in Ref. [30], therefore no comparison in these terms can be made. In this case, only considerations related to the specific speed are illustrated, in relation to the traditional method developed by Rohlik [12, 26].

Figure 2.12a, adapted from Refs. [12, 26], shows the stage total-to-static efficiency as a function of the specific speed for a radial inflow turbine, and the point corresponding to the optimal design for the case at hand. The specific speed of the optimal machine is ≈ 0.6, a value suggesting that design recommendations developed for turbochargers might still be valid for *m*ORC RITs with high expansion ratio. As expected, the efficiency of the *m*ORC turbine is considerably lower than that reported in the chart for the same specific speed, because this diagram was obtained from data about RITs featuring a much smaller

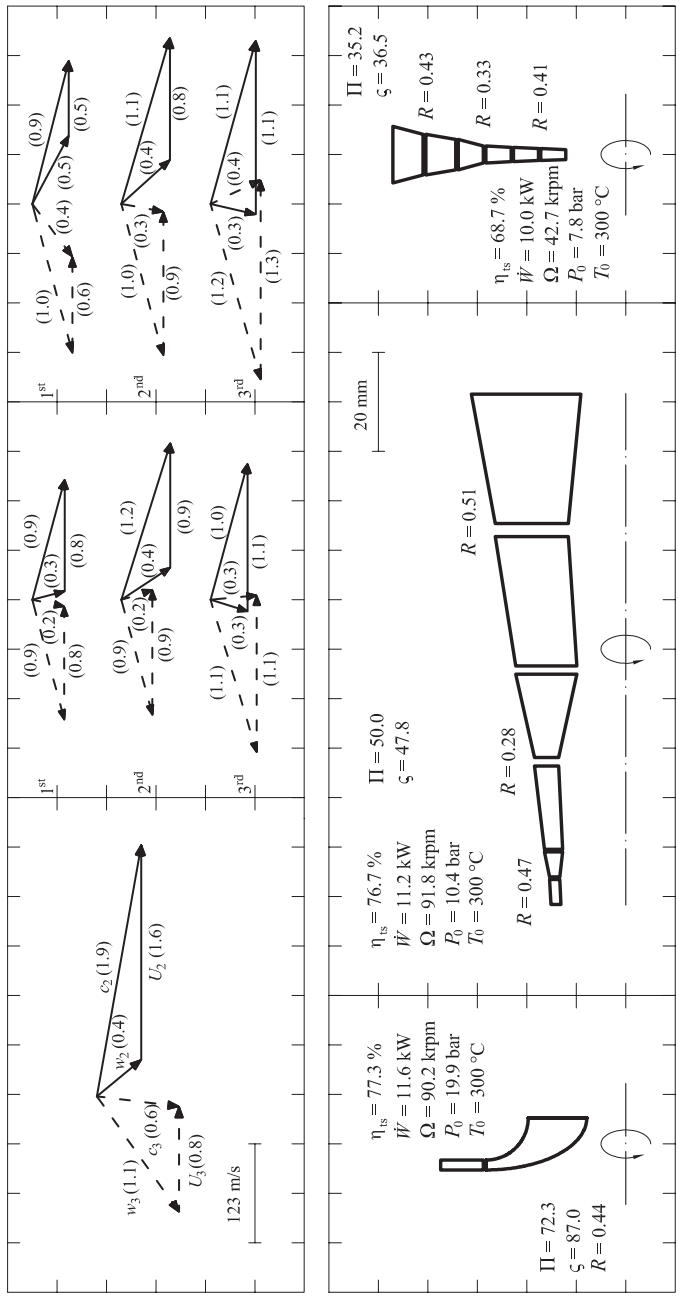

Figure 2.11: Turbine specifications and flow meridional channel corresponding to the global optima for the *m*ORC operating with MM introduced in Section 2.4.2 and depicted in Figure 2.10. The Mach numbers corresponding to the velocity triangles are presented in parenthesis. (-) Rotor inlet velocity triangle. (- -) Rotor outlet velocity triangle.

expansion ratio (< 3.5). The much lower efficiency of the *m*ORC turbine is caused by compressibility effects.

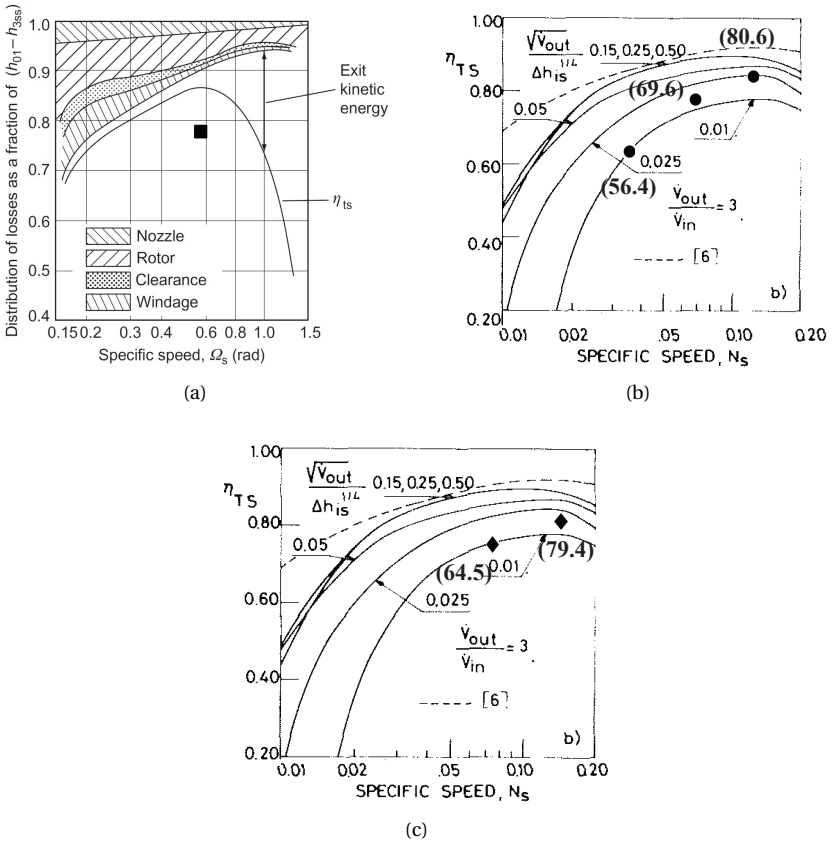

Figure 2.12: (a) Total-to-static efficiency for 90° radial inflow turbine stages as a function of the specific speed. Figure taken from Ref. [12, 26]. (■): optimal *m*ORC RIT (working fluid: MM). (b,c) Total to static efficiency for axial turbine stages operating with non-conventional fluids as a function of Ω_s, κ, and $\varsigma_{sg} \approx 3.0$ [31]. (•) in Figure (b): stages of the optimal *m*ORC ROT (working fluid: MM). (⧫) in Figure (c): stages of the optimal *m*ORC AXT (working fluid: MM). The values in parenthesis indicate the stage efficiency estimated with zTURBO.

Figures 2.12b and 2.12c depict the stage total-to-static efficiency for ORC axial turbines as a function of Ω_s, κ, and $\varsigma = 3.0$ [31]. They also show the coordinates corresponding to the selected ROT and AXT, including in parenthesis the efficiencies computed with zTURBO. The third stage of the AXT is not shown, because its coordinates fall outside these charts. The results of the case at hand resemble those from Ref. [31], thus providing confidence to this analysis.

The value of the specific speed calculated for each turbine stage is different, because the objective function of the optimizer is the overall total-to-static efficiency, which does not necessarily imply equal specific speed among the stages. Additionally, the first stage of the ROT and AXT have the same size parameter, though the corresponding stage efficiency is largely different. The reason is the widely dissimilar values of the specific speed, which,

in case of the ROT is grossly suboptimal, and also smaller than that of the AXT. Ultimately, this means that, recalling that the specific speed depends on the flow and stage load coefficients, as in $\Omega_s = \phi^{1/2}/\psi^{3/4}$ [12], the first stage of the ROT is excessively loaded; this feature of *m*ORC radial outflow turbines has been already discussed in Ref. [28].

The trends of the net efficiency as a function of the maximum cycle pressure displayed in Fig. 2.10 show how expander losses increase with increasing turbine pressure ratio. The following section provides a more detailed analysis of such relation.

INFLUENCE OF MAXIMUM CYCLE PRESSURE ON TURBINE EFFICIENCY

Figure 2.13 displays how the turbine total-to-static efficiency decreases with the maximum cycle pressure in all cases. In addition, the performance calculated for the RIT is always better than that for the AXT and ROT, independently of the fluid. This can be explained by noting that higher inlet pressures determine a combination of small size parameter and large volumetric expansion ratio, as shown in Fig. 2.13c for MM.

The analysis of the loss mechanisms allows to understand these trends.

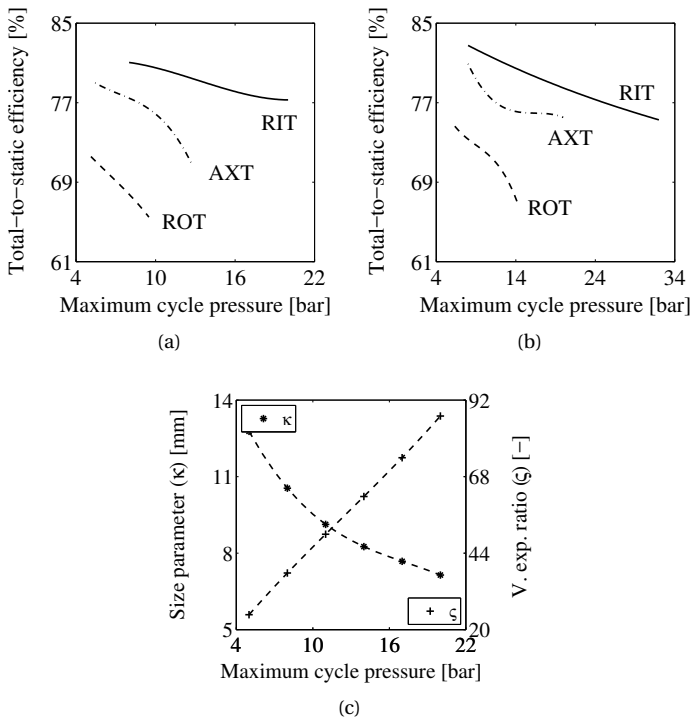

Figure 2.13: Optimization results: turbine total-to-static efficiency as a function of the maximum cycle pressure. Lines are obtained by interpolating the solutions calculated by the genetic algorithm. (a) Turbines operating with MM as working fluid. (b) Turbines operating with PP_2 as working fluid. (c) Size parameter and volumetric expansion ratio for the turbines operating with MM as the working fluid.

Loss breakdown for the radial inflow turbine

Figure 2.14a presents the loss breakdown as a function of the maximum cycle pressure in case MM is the working fluid. Figure 2.14b shows the corresponding specific speed,

degree of reaction and Mach number at stator outlet. Figure 2.14b shows that the optimization leads to turbines featuring similar specific speed values, namely, $0.5 < \Omega_s < 0.7$. This means that computed contribution of profile, secondary, and kinetic energy losses is similar, as depicted in 2.14a.

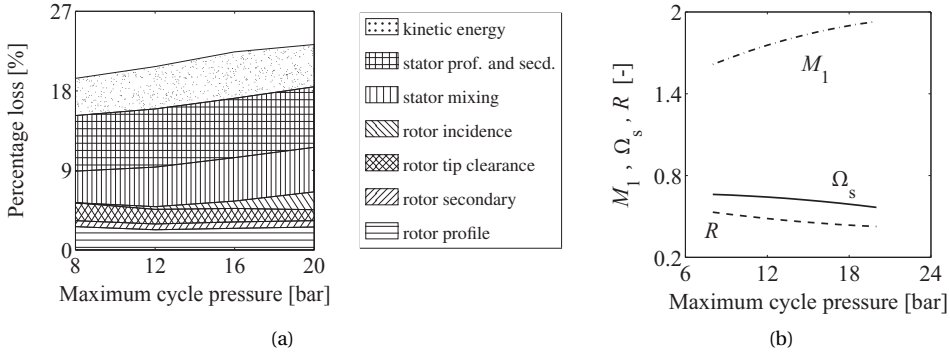

Figure 2.14: (a) Loss breakdown for the RIT operating with MM as a function of the maximum pressure, and computed by interpolating the results of the genetic algorithm. (b) Corresponding specific speed, degree of reaction, and Mach number at stator outlet.

The decrease in performance is thus mostly due to compressibility effects increasing with higher values of the pressure ratio, determining higher values of the Mach number. Accordingly, losses due to shock waves and mixing at the stator outlet become larger, as illustrated by the computed stator mixing losses, see 2.14a.

Being the degree of reaction a design variable, and being the blade height at stator outlet fixed, the value of degree of reaction which would cause perfect incidence cannot be attained at higher values of the inlet pressure. As a consequence, incidence losses grow with larger values of the inlet pressure (2.14a). Furthermore, the amount of tip flow strongly depends on the ΔP between the suction and pressure side of the rotor blades. Such pressure difference decreases with decreasing degree of reaction. Therefore, the tip clearance losses slightly decrease for increasing value of the pressure ratio.

Loss breakdown for the axial and radial outflow turbines

Figure 2.15a depicts the loss breakdown calculated for axial turbines operating with MM as working fluid. The loss percentage is computed as a summation of the contributions from all the blade rows. The stages likely feature different specific speed values, hence it is difficult to draw conclusions by relating losses to Ω_s. However, the analysis can be based on the evaluation of the relations composing the models implemented in zTURBO.

The profile loss is proportional to the stage loading, yet corrections for compressibility and Reynolds effects are necessary. The profile loss is thus approximately proportional to stage load ($\xi_{\mathrm{pr,axt}}$), down-stream Mach number (M_{ds}) and inversely proportional to the Reynolds number (Re), as in

$$\xi_{\mathrm{pr,axt}} \propto \psi\,, M_{\mathrm{ds}}\,, \frac{1}{\mathrm{Re}}. \tag{2.22}$$

Figure 2.15b presents values calculated for these quantities averaged over all the blade rows. A larger expansion ratio increases the stage loading, thus imposes a larger flow deviation, and primarily raises the profile loss. Moreover, the flow acceleration also increases

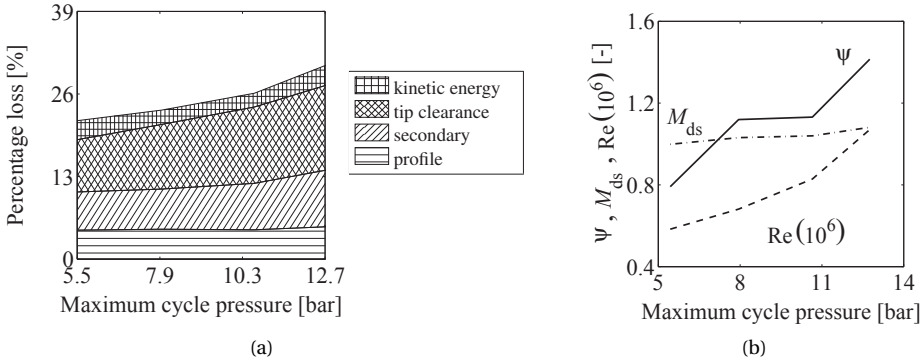

Figure 2.15: (a) Loss breakdown for the AXT operating with MM as a function of the maximum pressure, and computed by interpolating the results of the genetic algorithm. (b) Corresponding machine-averaged stage loading (ψ), Reynolds number (Re), and Mach number (M).

with $P_{\max}$, thus raises the Mach number and induces lower performance as the stream becomes transonic. Conversely, Reynolds effects are more prominent at low inlet pressure. All these effects balance, resulting in the profile loss being almost independent of maximum cycle pressure.

The secondary loss is proportional to flow deviation, and inversely proportional to flow acceleration. Furthermore, the secondary flow is larger for blades with low aspect ratio, hence

$$\xi_{\text{sc,axt}} \propto \frac{\vartheta}{\upsilon}, \gamma, \tag{2.23}$$

where $\xi_{\text{sc,axt}}$ is the percentage secondary loss, ϑ is the flow deviation, υ is the flow acceleration, and γ is the flow passage pitch-to-span ratio. A higher value of the pressure ratio increases the stage loading and the flow acceleration, and somehow these contributions balance out. In addition, a larger value of the pressure ratio decreases the volumetric flow and the blade height. As a result, the aspect ratio becomes incrementally suboptimal, thus raising secondary flow losses. Finally, since the manufacturing of shrouded blades is arguably unfeasible, due to the small turbine size, tip leakage is the main contribution to overall losses, and its effect becomes larger for increasing expansion ratio.

Figure 2.16 displays the loss breakdown computed for radial outflow turbines operating with MM as working fluid. As it can be seen, the trends calculated for all loss contributions are the same as those in Fig. 2.15a. However, the cross-sectional area strongly increases along the flow path in a radial outflow turbine. As a consequence, the blade height does not increase along the flow path as much as in an axial turbine. Due to this fact, the relative size of the tip clearance, and the corresponding losses, are larger than in comparable axial turbines.

In summary, this analysis shows that, for the given specification, the radial inflow configuration is preferable, leading to the highest net conversion efficiency. However, this conclusion may hold only if nominal operating conditions are considered. At off-design, multistage configurations might be beneficial, because it is possible to design transonic stages which are affected by lower mixing losses if compared to a single stage radial inflow turbine. Applications of *m*ORC systems like waste heat recovery from long-haul truck engines

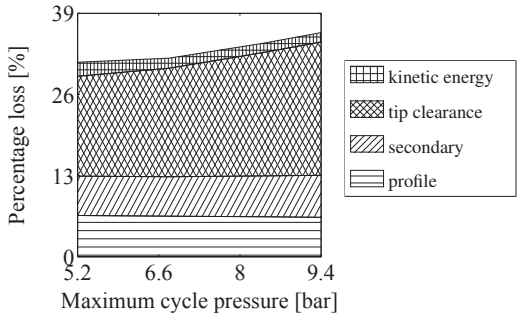

Figure 2.16: (a) Loss breakdown for the ROT operating with MM as a function of the maximum pressure, and computed by interpolating the results of the genetic algorithm.

or conversion of solar radiation require flexible operation [28], therefore the assessment of the best turbine configuration needs to encompass off-design performance.

2.5. CONCLUDING REMARKS

A robust two-step optimal design method for *m*ORC system design is presented. The thermodynamic cycle and the mean-line design of the turbine are integrated into the procedure. Three turbine configurations are treated, namely single-stage radial inflow, multi-stage radial outflow, and multi-stage axial. The first step allows to define the feasible bounds of the design space, and is based on the simultaneous calculation of the thermodynamic cycle and preliminary design of the turbine, in which the isentropic efficiency is assigned a value. The second step consists in a constrained optimization calculation whereby the system efficiency is the objective, but the isentropic efficiency of the mini turbine is a result of the mean-line design. In order to illustrate the method and qualitatively analyze and validate the results, the design of a 10 kW *m*ORC system has been performed and documented here. The system is an ORC setup named ORCHID for the testing of *m*ORC turbines, which is being realized at the Delft University of Technology.

The method is based on few assumptions which might affect the results in terms of absolute values, but the obtained trends are supposedly correct. In particular, most of the loss models implemented in the mean line code were developed for machines operating with fluids in thermodynamic states that can be calculated using the ideal gas assumption, which does not hold for the stator of high-temperature *m*ORC turbines. In addition, the data that were collected in order to develop the semi-empirical correlations of these models refer to machines characterized by low expansion ratio, as opposed to *m*ORC expanders. The accuracy of the results is also affected by the uncertainty of the fluid thermophysical property models, which in case of fluids made of complex organic molecules is comparatively low.

The study led to the following conclusions:

i) In order for the genetic optimization algorithm to be robust, the feasible design space must first be identified by means of a simplified integrated design procedure;

ii) In case of small power capacity, the blade height constraints the maximum cycle pressure. Furthermore, the value of the maximum cycle pressure depends on the

type of turbine, and the radial inflow configuration allows to reach higher maximum cycle pressure levels, hence higher system efficiency, also thanks to higher turbine efficiency.

iii) For *m*ORC radial outflow turbines, the optimal system features a turbine in which the first stage operates with a largely sub-optimal specific speed, due to geometrical constraints. This is the main cause of the lower estimated performance, if compared to the other turbine configurations, together with large tip clearance losses.

iv) The analysis of the turbine loss breakdown reveals that the major source of inefficiency is the tip clearance flow in case of axial and radial outflow turbines. Note though, that if the specified power output is larger, this effect becomes less relevant.

v) The maximum system efficiency is not necessarily achieved with the turbine featuring the highest isentropic efficiency. Lower pressure at the turbine inlet imply a larger machine and lower volumetric expansion ratio, which are strongly beneficial.

Currently, efforts are focused on CFD simulations aimed at further assessing the accuracy of the mean-line code. Future work with the ORCHID setup will be devoted to the experimental validation and calibration of the models adopted in the presented integrated design method for *m*ORC systems. In addition, the method will be extended to comprehend also the preliminary design of heat exchangers and the treatment of off-design operating conditions.

ACKNOWLEDGMENTS

The authors are grateful to Bosch GmBH for funding the project that led to the results presented in this article, and for the fruitful discussions with Dr. Bernd Banzhaf of the division Diesel Systems, Engineering Component - Simulation and Testing; and Dr. Martin Dreizler of the division Corporate Sector Research and Advance Engineering, Future Mechanical and Fluid Components.

NOMENCLATURE

b	Blade height [mm]
b'	Radial chord [mm]
c	Flow velocity [m/s]
D	Diameter [mm]
h	Enthalpy [kJ/kg]
$\dot{m}$	Mass flow rate [kg/s]
M	Mach number
N	Number
o	Opening [mm]
P	Pressure [bar]
$\dot{Q}$	Thermal power [kW]
r	Radius [mm]
R	Degree of reaction
s	Entropy [kJ/kg·K]
t	Distance [mm]
T	Temperature [°C]
U	Blade peripheral speed [m/s]
UA	Heat transfer coefficient [kW/K]
$\dot{W}$	Power [kW]
w	Relative flow velocity [m/s]
$\dot{V}$	Volumetric flow [m^3/s]

Greek symbols

α	Absolute flow angle [°]
β	Relative flow angle [°]
Δ	Difference
η	Efficiency
γ	Passage pitch-to-span ratio
κ	Size parameter [mm]
Ω	Rotational speed [krpm]
Ω_s	Specific speed
ϕ	Flow coefficient
ψ	Stage loading
Π	Pressure ratio
ρ	Density [kg/m^3]
ς	Turbine volumetric expansion ratio
ϑ	Flow deviation
υ	Flow acceleration
ζ	Loss coefficient

Subscripts

0..8	Thermod. states in Fig. 2.1b
0..4	Stage numbering in to Figs. 2.3 and 2.4
ab	Absolute
ax	Axial
cyc	Cycle
cl	Clearance
cn	Condenser
ds	Downstream
fl	Flaring
ge	Generator
h	Hub at rotor exit
hr	Heater
in	Inlet
is	Isentropic
m	Meridional component
max	Maximum
me	Mechanical
min	Minimum
net	Net
opt	Optimum
out	Outlet
pr	Profile
pm	Pump
pn	Pinch
rd	Radial
rg	Regenerator
rl	Relative
rt	Rotor
rw	Blade row-to-row
s	Shroud at rotor exit
sc	Secondary
sg	Stage
ss	Static
st	Stator
θ	Tangential component
te	Trailing edge
tit	Turbine inlet temperature
tr	Turbine
ts	Total-to-static
to	Stator throat
tot	Total

REFERENCES

[1] D. Haeseldonckx and W. Haeseleer, *The environmental impact of decentralised generation in an overall system context,* Renewable and Sustainable Energy Reviews **12**, 437 (2008).

[2] P. Colonna, E. Casati, C. Trapp, M. T., J. Larjola, T. Turunen-Saaresti, and A. Uusitalo, *Organic Rankine cycle power systems: from the concept to current technology, applications and an outlook to the future,* Journal of Engineering for Gas Turbines and Power **137**, 100801 (2015).

[3] S. Quoilin, M. Van Den Broek, S. Declaye, P. Dewallef, and V. Lemort, *Techno-economic survey of organic Rankine cycle (ORC) systems,* Renewable and Sustainable Energy Reviews **22**, 168 (2013).

[4] L. DiNanno, F. DiBella, and M. Koplow, *An RC-1 Organic Rankine Bottoming Cycle for an Adiabatic Diesel Engine*, Tech. Rep. DOE/NASA/0302-1 (NASA, Lewis Research Center, 1983).

[5] A. DiBella, L. DiNanno, and M. Koplow, *Laboratory and on-highway testing of diesel organic Rankine compound long-haul vehicle engine,* in *SAE International Congress and Exposition*, 830122 (SAE International, 1983).

[6] M. Astolfi, M. Romano, P. Bombarda, and E. Macchi, *Binary ORC (organic Rankine cycles) power plants for the exploitation of medium-low temperature geothermal sources - Part B: Techno-economic optimization,* Energy **66**, 435 (2014).

[7] A. La Seta, A. Meroni, J. G. Andreasen, L. Pierobon, G. Persico, and F. Haglind, *Combined turbine and cycle optimization for organic Rankine cycle power systems – part B: Application on a case study,* Energies **9**, 393 (2016).

[8] A. Head, C. De Servi, E. Casati, M. Pini, and P. Colonna, *Preliminary design of the ORCHID: A facility for studying non-ideal compressible fluid dynamics and testing ORC expanders,* in *ASME Turbo Expo*, Vol. 3 (2016) p. 14.

[9] Various Authors, *Matlab version 8.2.0.701 (r2013b),* (2013), the MathWorks Inc.

[10] P. Colonna, T. P. van der Stelt, and A. Guardone, *FluidProp (Version 3.0): A program for the estimation of thermophysical properties of fluids,* (2012), Asimptote bv.

[11] W. C. Reynolds and P. Colonna, *Vapor power plants,* in *Thermodynamics* (Cambridge University Press, 2018) Chap. 7, in Press.

[12] S. Dixon and C. Hall, *Fluid Mechanics and Thermodynamics of Turbomachinery*, 6th ed., edited by S. Dixon and C. Hall (Butterworth-Heinemann, Boston, MA, 2010).

[13] Various Authors, *Matlab – optimization toolbox 6.4,* (2013), the MathWorks Inc.

[14] D. Goldberg, *Genetic Algorithms in Search, Optimization & Machine Learning* (Addison-Wesley, Reading, MA, 1989).

[15] M. Pini, G. Persico, E. Casati, and V. Dossena, *Preliminary design of a centrifugal turbine for organic Rankine cycle applications,* Journal of Engineering for Gas Turbines and Power **135**, 042312 (2013).

[16] B. Bülten, W. Althaus, E. Weidner, and H. Stoff, *Experimental and numerical flow investigation of a centripetal supersonic turbine for organic Rankine cycle applications,* in 11th *European Conference on Turbomachinery Fluid Dynamics & Thermodynamics*, ETC2015-088 (2015) p. 12.

[17] A. Glassman, *Computer program for design and analysis of radial inflow turbines*, Tech. Rep. TN D-8164 (NASA, Lewis Research Center, 1976).

[18] H. Moustapha, M. F. Zelesky, N. C. Baines, and D. Japikse, *Axial and Radial Turbines* (Concepts NREC, Inc., White River Junction, VA, 2004).

[19] W. Traupel, *Thermische Turbomaschinen*, 3rd ed. (Springer-Verlag, Berlin, 1982).

[20] A. Wasserbauer and A. Glassman, *FORTRAN Program for Predicting the Off-Design Performance of Radial Inflow Turbines*, Tech. Rep. TN D-8063 (NASA, 1975).

[21] J. Stanitz, *Some theoretical aerodynamic investigations of impellers in radial and mixed flow centrifugal compressors,* Transactions of the ASME **74**, 473 (1952).

[22] C. Osnaghi, *Teoria delle Turbomachine* (Società Editrice Esculapio, Bologna, 2013).

[23] J. W. Sawyer, *Gas Turbine Engineering Handbook*, 2nd ed. (Gas Turbine Publications, Inc., Stamford, CT, 1966).

[24] M. Deich, G. Filippov, and L. Lazarev, *Atlas of Axial Turbine Blade Cascades*, C.E. Trans. 4563-4564 (CEGB Information Services, London, 1965).

[25] Various Authors, *Matlab – paralell computing toolbox,* (2013), the MathWorks Inc.

[26] H. Rohlik, *Analytical Determination of Radial Inflow Turbine Design Geometry for Maximum Efficiency*, Tech. Rep. TN D-4384 (NASA, Lewis Research Center, 1975).

[27] A. Whitfield and N. C. Baines, *Design of Radial Turbomachinery* (Longman Scientific & Technical, Harlow, Essex, 1990).

[28] E. Casati, S. Vitale, M. Pini, G. Persico, and P. Colonna, *Centrifugal turbines for mini-organic Rankine cycle power systems,* Journal of Engineering for Gas Turbines and Power **136**, 122607 (2014).

[29] E. Macchi, *Design criteria for turbines operating with fluids having a low speed of sound,* (Von Karman Institute for Fluid-dynamics, 1977) Chap. Closed Cycle Gas Turbines, Lecture Series 100.

[30] A. Perdichizzi, *Design criteria and efficiency prediction for radial inflow turbines,* in *ASME Turbo Expo*, 87-GT-231 (1987) p. 9.

[31] E. Macchi and A. Perdichizzi, *Efficiency prediction for axial-flow turbines operating with nonconventional fluids,* Journal of Engineering for Power **103**, 718 (1981).

3

ACTIVE SUBSPACES FOR THE OPTIMAL MEANLINE DESIGN OF UNCONVENTIONAL TURBOMACHINERY

The contents of this chapter appeared in:

S. Bahamonde, M. Pini, C. De Servi, and P. Colonna, *Active subspaces for the optimal meanline design of unconventional turbomachinery*, Applied Thermal Engineering 127, 1108-1118 (2017).

The preliminary fluid dynamic design of turbomachinery operating with non-standard working fluids and unusual operating conditions and specifications can be very challenging because of the lack of know-how and guidelines. Examples are the design of turbomachinery for small-capacity organic Rankine cycle and supercritical CO_2 cycle power plants, whereby the efficiency of turbomachinery components has also a strong influence on the net conversion efficiency of the system. These machines operate with the fluid in thermodynamic states that, for part of the process, largely deviate from those obeying to the ideal gas law, which implies the presence of so-called non-ideal compressible fluid dynamics effects.

Active subspaces, a model reduction technique, is at the basis of the methodology presented here aimed at the optimal meanline design of unconventional turbomachinery. The surrogate model depends on a very small set of non-physical variables, called active variables. The procedure integrates into a single constrained optimization framework the selection of the working fluid, the thermodynamic cycle calculation and the preliminary sizing of the turbomachinery component.

As a demonstration of the advantages of the proposed approach, the design of a 10 kW *mini organic Rankine cycle turbine with a turbine inlet temperature of* 240 °C *is illustrated. In this case, approximately the same maximum efficiency is estimated for three unlike turbines operating with different working fluids and rather different thermodynamic cycles. The use of active subspaces allows the seamless evaluation of the sensitivity of results to input parameters, both those related to the machine and the working fluid. The novel design procedure is compared in terms of computational efficiency to the conventional approach based on the coupling of a genetic algorithm directly with a meanline code. Results show that the procedure based on the use of surrogate models is more than two orders of magnitude faster. The surrogate can be used to solve any design problem within the specified boundaries of the design envelope. Results are affected by uncertainty on the estimation of losses and of effects, which, in turn, do not affect the applicability of the method, which will become quantitatively accurate once this information will become available. Work to this end is underway in various laboratories.*

3.1. INTRODUCTION

The increasing need for renewable energy conversion has boosted the development of power technologies based on thermodynamic cycles operating with unconventional fluids, e.g., the organic Rankine cyle (ORC) and the supercritical CO_2 cycle (sCO_2) [1]. In particular, R&D activities on mini ORC systems (*m*ORC, 3 – 50 kW) are considerably raising, because they are envisioned to play a relevant role in the decentralized energy generation scenario, and as waste heat recovery (WHR) systems for mobile engines, e.g., on board of long-haul trucks, ships, or aircraft [2–5].

The success of these technologies strongly depends on the realization of high efficiency turbomachinery. In this respect, its preliminary design is key and particularly challenging, because the machine is bound to be unconventional, and its feasibility and manufacturability are not guaranteed. The fluid dynamic design strongly depends on the working fluid and on the cycle operating parameters, and is constrained by a considerable number of parameters related to feasibility, e.g., rotational speed, tip clearance, blade height, etc. For instance, for a turbine operating in a high-temperature *m*ORC turbogenerator, the maximum pressure ratio, and thus the cycle thermal efficiency, might be constrained by the minimum blade height at the first-stage rotor inlet; this blade height is ultimately deter-

mined by a combination of factors like the fluid volumetric flow, the turbine degree of reaction, and the inlet diameter [6]. Moreover, for WHR on board of transportation systems, additional features to be considered are the weight and volume of the heat exchangers. Note that, although critical for *m*ORC systems, some of these challenges affect, to some extent, also the design of other more conventional ORC and $scCO_2$ systems. Here, emphasis is given to the optimal meanline design of mini-ORC turbines, but the methodology is applicable to a large variety of turbine and compressors whenever working fluids and operating conditions do not allow the use of an experience-based approach.

Generally, the preliminary fluid dynamic design stage is accomplished by following two sequential (or independent) procedures. First, the isentropic efficiency of the machine is estimated by means of similarity parameters taking into account the characteristics of the fluid process occurring in an ORC turbine: large volumetric expansion ratio, compressibility effects, and, in case of a small power output, scaling effects [7, 8]. These similarity parameters are a function of the fluid thermodynamic conditions at turbine inlet and outlet. As such, they have been widely used in the design of ORC systems, see, e.g, Refs. [9–11]. Once the best working fluids are selected, the geometry of the machine is determined by means of an automated optimization process based on a meanline turbine model, which is properly initialized using the outcome of the first step. The set of equations constituting the meanline turbine model is equivalent to a highly non-linear multidimensional function that is prone to discontinuities in the objective function. As a result, and in order to enhance the robustness of the optimization, a gradient-free optimizer is commonly adopted, see, e.g., Refs. [12–14].

This design process is arguably time-consuming and it can lead to suboptimal results, because it is made of subsequent procedures that have to be performed for each considered working fluid, for different turbine configurations and for a wide range of operating conditions. Furthermore, as already mentioned, the design of mini ORC turbines is particularly challenging, for the machine geometry and the operating conditions are mutually constrained variables, hence hampering the definition of a feasible design space. Ultimately, it is possible to assert that, for an inexperienced engineer, achieving an optimum solution might take few weeks.

A further drawback follows from the use of a gradient-free optimizer: the sensitivity of expander efficiency, or of any other output of interest, to individual design inputs is lost. If available, this information can be used to gain physical understanding of loss mechanisms already at preliminary design level.

A previous work demonstrated that a reduced-order model has the potential for abating the aforementioned disadvantages [15]. Following such development, this paper presents an innovative design methodology employing a reduced-order model that integrates fluid selection, thermodynamic cycle calculation, and preliminary fluid dynamic design of the corresponding ORC turbine.

The methodology is based on active subspaces, a parameter-reduction strategy that utilizes the dominant directions of the gradient of a scalar function to transform a multidimensional input space into a lower-dimensional problem [16]. The obtained surrogate is computationally efficient and robust, which makes this approach arguably preferable compared to the conventional design procedure. In addition, the resulting surface can be used to analyze the influence of the individual design inputs on the objective function. Finally, the selection of the working fluid is not limited to existing substances, because a fluid is specified by several molecular parameters, thus optimal solutions may encompass

parameters that do not correspond to any available compound, but that might guide to the synthesis of a new chemical. The benefits of this approach have been demonstrated by applying it to the exemplary design of a 10 kW ORC unit for exploitation of medium-temperature thermal sources and adopting a single-stage radial inflow turbine as expander. The results and the performance of the design procedure are discussed and compared to those obtained by employing a conventional approach in order to put into evidence the main advantages.

3.2. METHOD

The procedure for the integration of the thermodynamic cycle calculation, the working fluid selection, and the turbine preliminary design, consists of three steps. The first step is to construct a turbine model that includes the parameters of an equation of state to predict the properties of the working fluid, as in

$$f = f(\mathbf{x}), \quad \mathbf{x} = [\mathbf{y}, \mathbf{z}], \quad \mathbf{x} \in [-1, 1]^m, \tag{3.1}$$

where $\mathbf{y}$ and $\mathbf{z}$ are vectors containing the inputs for the fluid and turbine models, respectively. Expression (3.1) represents a scalar function to compute any quantity of interest, e.g., turbine total-to-static efficiency. Observe also that the inputs in $\mathbf{x}$ are centered and normalized, and that in order to construct the reduced-order model, (3.1) needs to be smooth [16]. The second step is to approximate (3.1) to a lower order function $\hat{f}$, i.e.,

$$f(\mathbf{x}) \approx \hat{f}(\mathbf{x}_{\text{ac}}), \quad \mathbf{x}_{\text{ac}} \in \mathbb{R}^n, \quad n < m, \tag{3.2}$$

where $\mathbf{x_{ac}}$ is constituted by the *active variables*. The reduced-order model is then used to construct a response surface of the turbine efficiency and the main turbine operating and geometric parameters. In the third and final step, the surrogate is employed to perform the optimization. Sections 3.2.1 - 3.2.4 describe these steps in detail.

As shown in Eq. (3.1), the method requires the definition of the design space $\mathbf{x}$. In order to better illustrate how $\mathbf{x}$ is constructed, a relevant application is herein introduced: the preliminary design of a *m*ORC unit (power capacity < 20 kW) for the exploitation of medium-temperature thermal sources (maximum cycle temperature < 240°C), and adopting a single-stage radial inflow turbine. This design problem, representative of applications like waste heat recovery from long-haul truck diesel engines [2], and solar power conversion in space [17, 18], poses particular challenges because the choice of system operating conditions, working fluid, and components design, are mutually constrained [6].

Figure 3.1 shows the corresponding process flow diagram and an exemplary thermodynamic cycle in the temperature-entropy plane. Table 3.1 lists the fluids selected because they feature a critical temperature > 240°C, and because of their high thermal stability [18].

The turbine preliminary design is performed by means of a meanline code, whose loss models are listed in Ref. [6]. These models have been developed for conventional turbomachinery operating with fluids in the the ideal gas region, and featuring subsonic flows and large Reynolds numbers. The meanline code has been validated with test cases presenting these characteristics. On the other hand, it is not possible to perform this validation for ORC turbines, due to the lack of experimental datasets. In this respect, work is in progress in order to be able to perform accurate measurements on mini ORC turbines [22]. Anyhow, the validity of the procedure to create a reduced-order model is not affected by the uncertainty in the loss correlations.

Table 3.1: Molecular mass (χ), acentric factor (ω), critical pressure (P_{cr}), critical temperature (T_{cr}), and molecular complexity $\left(\sigma = \frac{T_{cr}}{R}\left(\frac{\partial s_{sv}}{\partial T}\right)_{T_r=0.7}\right)^*$ for the selected working fluids [19, 20].

		χ	ω	P_{cr}	T_{cr}	σ
		kg/mol	-	bar	°C	-
toluene	C_7H_8	0.0921	0.2657	41.26	318.60	9.04
n-heptane	C_7H_{16}	0.1002	0.3490	27.36	266.98	17.56
m-xylene	C_8H_{10}	0.1062	0.3260	35.34	343.74	14.34
n-octane	C_8H_{18}	0.1142	0.3590	24.97	296.17	23.50
hexamethyldisiloxane (MM)	$C_6H_{18}OSi_2$	0.1624	0.4180	19.39	245.55	28.14
octamethyltrisiloxane (MDM)	$C_8H_{24}O_2Si_3$	0.2365	0.5290	14.15	290.94	48.44
octamethylcyclotetrasiloxane (D_4)	$C_8H_{24}O_4Si_4$	0.2966	0.5920	13.32	313.34	51.89
decamethyltetrasiloxane (MD_2M)	$C_{10}H_{30}O_3Si_4$	0.3107	0.6680	12.27	326.25	65.95
decamethylcyclopentasiloxane (D_5)	$C_{10}H_{30}O_5Si_5$	0.3708	0.6580	11.61	346.08	73.37
dodecamethylpentasiloxane (MD_3M)	$C_{12}H_{36}O_4Si_5$	0.3848	0.7220	9.45	355.21	92.31
dodecamethylcyclohexasiloxane (D_6)	$C_{12}H_{36}O_6Si_6$	0.4449	0.7360	9.61	372.63	104.54
tetradecamethylhexasiloxane (MD_4M)	$C_{14}H_{42}O_5Si_6$	0.4590	0.8250	8.77	380.05	106.39
Perfluorodecalin (PP_5)	$C_{10}F_{18}$	0.4620	0.4777	17.88	291.85	60.74
Perfluoro-2,4-dimethyl-3-ethylpentane (PP_{90})	C_9F_{20}	0.4881	0.5621	16.00	256.85	50.93

* For a complete discussion on the molecular complexity see Ref. [21].

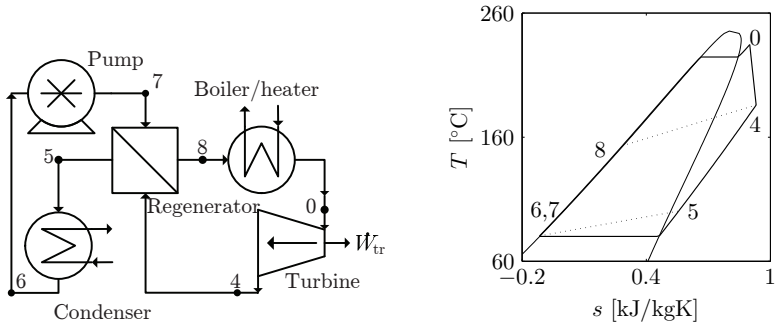

Figure 3.1: (a) Process flow diagram of an ORC system with regeneration. (b) Exemplary temperature-entropy diagram of a superheated thermodynamic cycle. Working fluid: MM, condensing temperature: 80°C, evaporating pressure: 14 bar, degree of superheating: 10 K, regenerator pinch temperature: 20 K, pressure loss: 0 %, turbine isentropic efficiency: 80 %.

The methodology has been implemented in a general-purpose programming environment [23], and it has been adapted for parallel computing. The original high-order turbine model consists of a meanline program for the preliminary design of turbomachinery [24], coupled with a computational library to which the specific fluid model developed for this purpose has been added [20]. The results presented here have been obtained on a Windows 64-bit computer, equipped with a 3.60 GHz processor with eight virtual cores and 16 GB of RAM.

3.2.1. WORKING FLUID MODEL

The model must guarantee sufficiently accurate estimation of the fluid thermodynamic properties for a wide range of operating conditions and for different working fluids; yet it should feature the lowest number of parameters in order to ease the construction of the reduced-order model. Cubic equations of state (CEoS) provide a balance between these requirements [25]. Four models were initially considered: van der Waals (VDW) [26], Redlich/Kwong (RK) [27], Peng/Robinson (PR)[28], and Soave/Redlich/Kwong (SRK) [29]. All these CEoS can be written with the general form

$$P = \frac{RT}{v-\gamma} - \frac{a(T)}{(v+\varepsilon\gamma)(v+\tau\gamma)}, \tag{3.3}$$

where P is the pressure, T is the temperature, v is the molar volume, and R is the universal gas constant. The other parameters of (3.3) ($a(T)$, ε, γ, and τ) depend on the selected model, and are a function of the temperature, acentric factor, and critical properties [25, 30].

The ideal gas heat capacity at constant pressure is approximated as a function of the molecular complexity [21], defined as

$$\sigma \equiv \frac{T_{cr}}{R}\left(\frac{\partial s_{sv}}{\partial T}\right)_{T_r=0.7}, \tag{3.4}$$

where s_{sv} is the saturated-vapor entropy. The partial derivative in (3.4) is calculated at a reduced temperature of $T_r = 0.7$. The molecular complexity parameter is used because it is

directly related to the molecular structure of the fluid and therefore to its heat capacity [21]. From the definition (3.4), it is possible to demonstrate that σ and the corresponding heat capacity are proportional.

A fluid model can thus be expressed as a function of five parameters, i.e.,

$$\text{fluid model} = f(\chi, \omega, P_{\text{cr}}, T_{\text{cr}}, \sigma). \tag{3.5}$$

In order to choose the best CEoS model, (3.3) was used to compute the saturation pressure and vapor molar volume for temperature values between 80°C and 240°C and for the fluids listed in Table 3.1. The model outputs were then compared against calculations performed with state-of-the-art fluid libraries implementing reference equation of state models [19, 20]. VDW and RK showed excessive deviation from the reference values and were consequently discarded. The computation of the property values with SRK is affected by a mean relative deviation from reference values that is lower than 4 % per fluid, while PR yielded some deviations from reference values as high as 14 %. SRK was therefore selected for implementation into the coded procedure. The addition of complex transport property models to the method is left for future developments. The viscosity employed in the estimation of stator losses is taken as a constant equal to 10^{-5} Pa·s [15].

The temperature dependence of the non-dimensional heat capacity is commonly expressed as a polynomial, i.e.,

$$\hat{c}_P = \frac{c_P}{R} = \mathbf{a}[1 \quad T \quad T^2 \quad T^3]', \quad \mathbf{a} = [a_1 \quad a_2 \quad a_3 \quad a_4], \tag{3.6}$$

where c_P is the molar heat capacity. The coefficients in $\mathbf{a}$ are fluid dependent, and they are generally determined by experiments combined with knowledge of the fluid molecular structure [25].

In order to approximate $\mathbf{a}$ as a function of σ, five $\hat{c}_P$ samples for equidistant temperature levels between 80°C and 240°C are obtained for each fluid by means of reference models [19, 20]; Figure 3.2a shows the values obtained with the accurate models and their regression using

$$\hat{c}_P\Big|_T \approx f(\sigma) \tag{3.7}$$

for each temperature. For a given σ, five $\hat{c}_P$ samples can be estimated by means of (3.7). These samples are then used to perform a polynomial regression and obtain $\mathbf{a}$. Figure 3.2b presents the mean relative error of the estimation of the heat capacity values within the selected temperature range, and as a function of the molecular mass of the selected fluids.

3.2.2. NORMALIZED INPUT OF THE TURBINE MODEL FOR PRELIMINARY DESIGN

A meanline code for the preliminary design of turbomachinery [6, 24] is coupled with the in-house computational fluid library [20] in which fluid model (3.5) has been implemented. Among various inputs, this model requires the turbine rotational speed Ω, rotor inlet diameter D_2, and mass flow $\dot{m}$. The successful application of the active subspaces method requires that the model of the turbine is smooth , therefore Ω, D_2 and $\dot{m}$ must be normalized, such that the input parameters are fluid independent. To this purpose, the mass flow rate is computed by means of the isentropic power $\dot{W}_{\text{s}}$, as in

$$\dot{m} = \frac{\dot{W}_{\text{s}}}{\Delta h_{\text{s}}}, \tag{3.8}$$

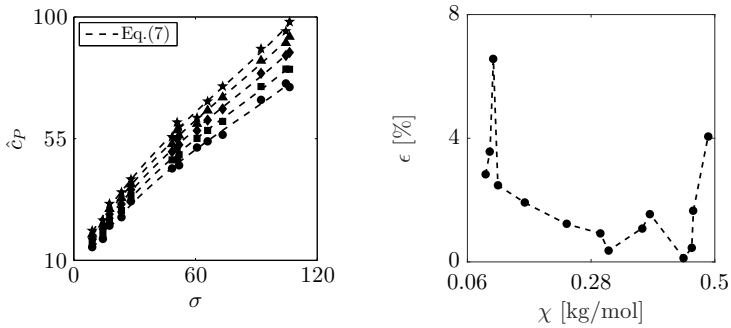

Figure 3.2: (a) Non-dimensional ideal gas heat capacities for the fluids listed in Table 3.1 as a function of the molecular complexity and for five temperature levels: (★) $T = 240°C$, (▲) $T = 200°C$, (⧫) $T = 180°C$, (■) $T = 100°C$, (•) $T = 80°C$. (- -) Polynomial regressions for each temperature level. (b) Mean error of the approximation of the heat capacity as a function of the molar mass and for the fluids listed in Table 3.1.

where Δh_s is the specific isentropic expansion work. Likewise, the rotational speed is calculated with the isentropic specific speed $\Omega_{e,s}$, i.e.,

$$\Omega = \frac{\Omega_{e,s}\Delta h_s^{3/4}}{\left(\dot{m} v_{out,s}\right)^{1/2}}, \tag{3.9}$$

where $v_{out,s}$ is the specific volume at the turbine outlet. The specific speed is therefore a design choice; a previous study suggests that the optimum value of $\Omega_{e,s}$ is in the range $[0.5, 0.7]$ [8].

Finally, an optimal rotor inlet diameter is estimated by means of conventional design guidelines for radial inflow turbines [31], combined with a mass balance assuming an isentropic expansion, as in

$$D_2 = 2\left(\frac{\dot{m} v_{out,s}}{\Omega\phi\pi\vartheta_0^2\left(1-\varphi_0^2\right)}\right)^{1/3}, \tag{3.10}$$

where ϑ_0 is the radius ratio of the rotor outlet shroud to rotor inlet ($r_{s,3}/r_2$, see Fig. 3.3), and φ_0 is the radius ratio of the rotor outlet hub to shroud ($r_{h,3}/r_{s,3}$, see Fig. 3.3). The subscript 0 indicate that these variables are primarily inputs used to compute the rotor diameter; the turbine model ultimately provides the design values of ϑ and φ. Furthermore, (3.10) requires the flow coefficient

$$\phi = c_{m,3}/U_2, \tag{3.11}$$

which is taken equal to 0.3. In (3.11), $c_{m,3}$ is the meridional flow velocity at rotor outlet, and U_2 is the rotor peripheral speed.

Figure 3.3 presents the meridional channel of a radial inflow turbine stage, and Table 3.2 presents the inputs required by the combined meanline/fluid model. Note that T_{ev}, T_{cn}, and ΔT_{sh} are used to determine the turbine inlet temperature and inlet/outlet pressure values, thus connecting the turbine model with the thermodynamic cycle calculation.

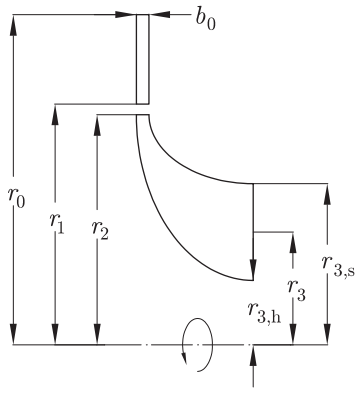

Figure 3.3: Meridional channel of a radial inflow turbine.

Inputs for the fluid model, **y** in (3.1)		Inputs for the turbine model, **z** in (3.1)	
Molar mass	χ	Cycle evaporating temp.	T_{ev}
acentric factor	ω	Isentropic power	$\dot{W}_{\text{tr,s}}$
Critical pressure	P_{cr}	Isent. deg. of reaction	R_{s}
Critical temperature	T_{cr}	Isent. specific speed	$\Omega_{\text{e,s}}$
Molecular complexity	σ	Stator outlet blade angle	$\alpha_{1,\text{ge}}$
		Rotor outlet blade angle	$\beta_{3,\text{ge}}$
		Stator outlet/rotor inlet radius ratio	r_1/r_2
		Stator inlet/outlet radius ratio	r_0/r_1
		Rotor inlet/outlet radius ratio	r_2/r_3
		Degree of superheating	ΔT_{sh}
		Cycle condensing temperature	T_{cn}
		Tip clearance thickness	t_{cl}
		Trailing edge thickness	t_{te}
		Rotor outlet shroud to inlet radius ratio	ϑ_0
		Rotor outlet shroud to hub radius ratio	φ_0
		Flow coefficient	ϕ

Table 3.2: Inputs for the combined turbine and fluid model.

3.2.3. ACTIVE SUBSPACES FOR THE CONSTRUCTION OF A REDUCED-ORDER MODEL

Ref. [16] provides a thorough review of the active subspaces method; the goal of this method is to transform the scalar function (3.1),

$$f = f(\mathbf{x}), \quad \mathbf{x} = [x_1, x_2, ..., x_m]', \quad \mathbf{x} \in [-1, 1]^m,$$

into (3.2), a lower-dimension approximation,

$$f(\mathbf{x}) \approx \hat{f}(\mathbf{x}_{\text{ac}}), \quad \mathbf{x}_{\text{ac}} \in \mathbb{R}^n, \quad n < m.$$

The input space of $\hat{f}$, $\mathbf{x}_{\text{ac}}$, is constituted by *active variables*: linear combinations of the original inputs, i.e.,

$$\mathbf{x}_{\text{ac}} = \mathbf{B}\mathbf{x}, \tag{3.12}$$

where $\mathbf{B}$ is a $n \times m$ matrix. The active subspaces method provides a strategy to compute $\mathbf{B}$. The procedure is based on the study of matrix $\mathbf{C}$,

$$\mathbf{C} = \mathbb{E}\left[(\nabla_{\mathrm{x}} f)(\nabla_{\mathrm{x}} f)'\right] = \int (\nabla_{\mathrm{x}} f)(\nabla_{\mathrm{x}} f)' \rho \, d\mathbf{x}, \tag{3.13}$$

where $\mathbb{E}$ denotes the expectancy, ρ is a probability density function, and $\nabla_{\mathrm{x}} f$ is the column vector of partial derivatives of f, namely,

$$\nabla_{\mathrm{x}} f = \left[\frac{\partial f}{\partial x_1}, \frac{\partial f}{\partial x_2}, ..., \frac{\partial f}{\partial x_m}\right]'. \tag{3.14}$$

The expectancy of a random variable x is the weighted average of all values x can take; $\mathbf{C}$ could be interpreted as the uncentered covariance of $\nabla_{\mathrm{x}} f$. As such, its eigenvectors determine the directions on which f changes the most, on average [32].

If multidimensional integration is not feasible, $\mathbf{C}$ can be approximated by sampling as

$$\hat{\mathbf{C}} = \frac{1}{M} \sum_{j=1}^{M} (\nabla_{\mathrm{x}} f)(\nabla_{\mathrm{x}} f)', \tag{3.15}$$

where M is the number of samples. The sampling strategy and number of samples might affect the accuracy of this approximation; this is discussed in detail in Ref. [16]. For this work, a previous analysis indicated that sampling with a latin hypercube combined with sparse grid produced the best results [15]. The derivatives in (3.15) can be computed by means of finite differences. Alternatively, $\hat{\mathbf{C}}$ can be determined with local linear models [16]; the latter has been used in this work.

$\hat{\mathbf{C}}$ can be transformed by a real eigenvalue decomposition, because it is real and symmetric. Therefore,

$$\hat{\mathbf{C}} = \hat{\mathbf{W}} \hat{\Lambda} \hat{\mathbf{W}}', \tag{3.16}$$

where $\hat{\Lambda}$ is a diagonal matrix containing the eigenvalues, and $\hat{\mathbf{W}}$ is a matrix containing the eigenvectors. The eigenvalues represent the magnitude of the variance of $\nabla_{\mathrm{x}} f$ along their eigenvectors orientation. It follows that large gaps between eigenvalues indicate directions where f changes the most. Subsequently, these matrices can be separated in two subsets denominated active (ac) and inactive (ic), namely,

$$\hat{\mathbf{W}} = \begin{bmatrix} \hat{\mathbf{W}}_{\mathrm{ac}} & \hat{\mathbf{W}}_{\mathrm{ic}} \end{bmatrix}, \quad \hat{\Lambda} = \begin{bmatrix} \hat{\Lambda}_{\mathrm{ac}} & \hat{\Lambda}_{\mathrm{ic}} \end{bmatrix}. \tag{3.17}$$

$\hat{\Lambda}_{\mathrm{ac}}$ contains the largest eigenvalues separated from $\hat{\Lambda}_{\mathrm{ic}}$ by a large gap; $\hat{\mathbf{W}}_{\mathrm{ac}}$ contains the corresponding eigenvectors. The input space is then geometrically transformed and aligned with $\hat{\mathbf{W}}_{\mathrm{ac}}$, in order to "hide" the directions where the function variability is small. This transformation leads to a lower-order input space formed by the active variables,

$$\mathbf{x}_{\mathrm{ac}} = \hat{\mathbf{W}}'_{\mathrm{ac}} \mathbf{x}. \tag{3.18}$$

$\mathbf{B}$ in (3.12) is therefore the active-eigenvector matrix $\hat{\mathbf{W}}'_{\mathrm{ac}}$.

Note that, thanks to the sampling required to approximate $\hat{\mathbf{C}}$, there are M transformations in the active subspace $\left(\hat{f} : \mathbf{x}_{\mathrm{ac}} \rightarrow f\right)$. These samples could be used to construct the reduced-order model by means of a regression based on any functional form. Alternatively, additional sampling might be required to cover regions with a low number of solutions.

Consider the following function as an illustrative exercise (adapted from Ref. [16]),

$$f = (0.7x_1 + 0.3x_2)^2 + 1. \tag{3.19}$$

Figure 3.4a presents a surface plot of (3.19) constructed with one hundred samples. Figure 3.4b shows the surface top view, with the sample gradients represented by arrows, and with the corresponding active and inactive eigenvectors. Note that the sample gradients are prominently aligned with a single orientation revealed by $\hat{\mathbf{W}}_{\text{ac}}$; the function variability has thus one dominant direction. Subsequently, the input space is rotated and aligned with $\hat{\mathbf{W}}_{\text{ac}}$, "hiding" the directions of low function variability, and reducing the number of model inputs to a single active variable, see Figure 3.4c. Finally, by means of the available samples, a polynomial regression is realized in the active subspace, and the reduced-order model adopts the functional form

$$\hat{f} = 0.6x_{\text{ac}}^2 + 1. \tag{3.20}$$

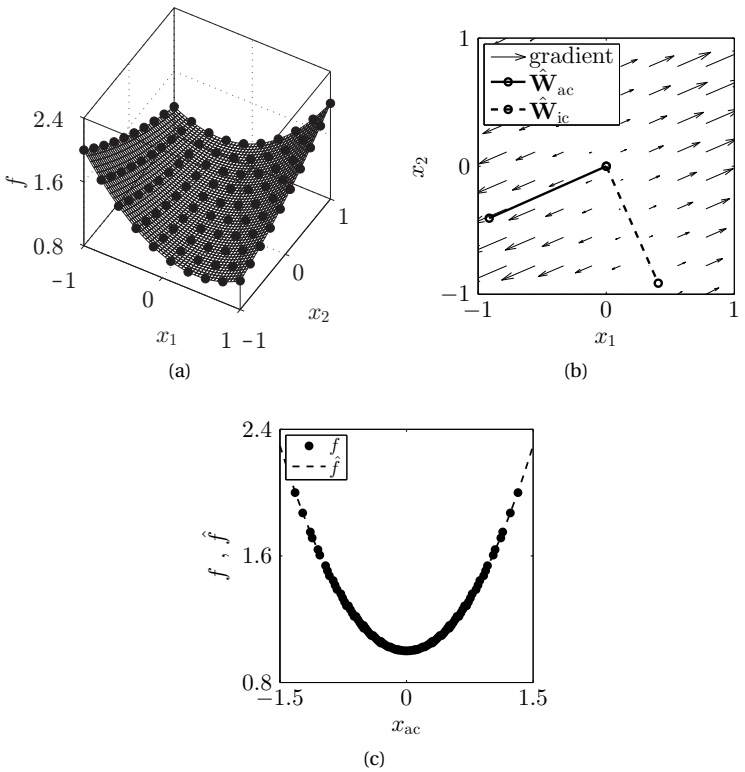

Figure 3.4: Exemplary construction of a reduced-order model. (a) Surface plot of (3.19) produced with one hundred samples (•). (b) Surface top view, with the sample gradients represented by arrows, and with the corresponding active ($\hat{\mathbf{W}}_{\text{ac}}$) and inactive ($\hat{\mathbf{W}}_{\text{ic}}$) eigenvectors. (c) Reduced-order model in the active subspace, function samples (•), and functional form (3.20) (-). Example adapted from Ref. [16].

3.2.4. OPTIMIZATION

Figure 3.5 presents a plot of the exemplary reduced-order model (3.19). The minimum function value is located between $x_{ac} = -0.2$ and $x_{ac} = 0.2$. The next step is the transformation of active variables in this region into original inputs. This problem constitutes an undetermined system of equations, where (3.12) is the sole member,

$$\mathbf{x}_{ac} = \mathbf{B}\mathbf{x},$$

and $\mathbf{x}$ becomes a vector with m number of unknowns. An alternative to solve this system is to perform a random search in $\mathbf{x}$, until solutions within the region $-0.2 \leq \mathbf{B}\mathbf{x} \leq 0.2$ are found. This procedure is computationally cheap, thanks to the fact that each transformation $\mathbf{B}\mathbf{x}$ takes only few milliseconds to compute.

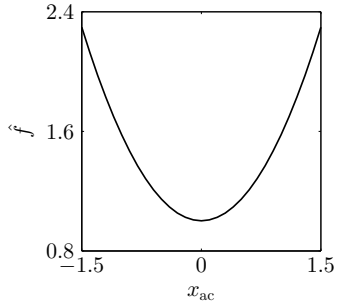

Figure 3.5: Exemplary reduced-order model (3.20).

TURBINE CONSTRAINED DESIGN

The meanline model computes several outputs of interest, e.g., the objective of the optimization which is typically the total-to-static efficiency $\eta_{tr,ts}$, and geometrical constraints, e.g. the radius ratio of the rotor outlet shroud to rotor inlet, $r_{s,3}/r_2$. Each output thus requires its own reduced-order model. The turbine meanline model can thus be transformed into a system of equations in the form

$$\text{Turbine reduced-order model} \begin{cases} \hat{\eta}_{tr,ts} & = \hat{f}\left(\mathbf{x}_{ac,\eta}\right), \\ \hat{\phi}_i & = \hat{g}_i\left(\mathbf{x}_{ac,\phi,i}\right), \quad i \in \{1,...,N\}, \end{cases} \tag{3.21}$$

where $\hat{\eta}_{tr,ts}$ is the active subspace model of the objective function, and $\hat{\phi}_i$ is the i^{th} active subspace model corresponding to a constrained output. Finally, the optimization problem reads

$$\begin{aligned} &\text{Maximize} && \hat{\eta}_{tr,ts}, \\ &\text{subject to} && \psi_{min,i} \leq \hat{\phi}_i \leq \psi_{max,i}, \quad i \in \{1,...,N\}, \end{aligned}$$

where ψ are the given design constraints. The problem can be solved by exploiting the random search approach, and by taking into account that each transformation $\mathbf{B}\mathbf{x}$ must concurrently respect the imposed constraints; this is the method adopted in this work. Alternatively, the optimization could be performed with a genetic algorithm or a gradient-based search method, as presented in Ref. [15].

3.3. EXEMPLARY APPLICATION

The test case is introduced in Section 3.2. Table 3.3 presents the design space, constant parameters, and required model outputs for the construction of the active subspace model. Note that the minimum and maximum values of the fluid parameters are taken from Table 3.1. Additionally, the degree of reaction is confined to a relatively small range, in order to guarantee a feasible combination of degree of reaction and specific speed, thus preventing discontinuities in the objective function. The other parameters are selected according to design practices for radial inflow turbines.

3.3.1. SURROGATE OF THE TURBINE EFFICIENCY FUNCTION

Due to the noisy nature of the meanline code, the determination of the active eigenvectors is performed with an oversampling factor of fifty, which is beyond the customary range (between two and ten). Figure 3.6 displays the results of the estimation of $\mathbf{C}$ associated to the total-to-static efficiency function. According to Figure 3.6a, the largest gap among eigenvalues is the first one, thus suggesting that the reduced-order model can be constructed with a single active variable. Nonetheless, the second gap is comparatively large, indicating the existence of another relevant direction of function variability. The reduced-order function is then constructed with two active variables; Figures 3.6b and 3.6c show the corresponding eigenvectors, and Figure 3.6d presents the corresponding response surface.

The dotted lines in Figures 3.6a-3.6c are bootstrap intervals [16]; they allow to assess the accuracy of the estimation of $\mathbf{C}$. These intervals thus suggest that the computation of the eigenvalues and the first eigenvector are accurate. However, the estimation of the second eigenvector is poor, for the error in the estimate is inversely proportional to the size of the second, smaller, eigenvalue gap. Eventually, this inaccuracy increases the approximation error of the reduced-order model.

Figure 3.7a presents the contour plot of the surrogate for the efficiency; Figure 3.7b displays the corresponding standard deviation, which includes the dispersion induced by the approximation of the fluid model and the meanline code. These charts are obtained with a minimum of ten samples per each region traced in Figure 3.7b. The sampling needed to determine $\hat{\mathbf{C}}$ does not provide enough samples in all the boxes in Figure 3.7b; thus, additional sampling must be performed wherever needed. The red areas indicate regions where the surrogate is not valid, because either the meanline code fails, or no active variables exist. The active subspace model features good accuracy, except for few combinations of active variables. The same procedure has been successfully applied to all the outputs of interest listed in Table 3.3, eventually employing a total time of five hours to construct the surrogate.

The reduced-order model depicted in Figure 3.7a is a polynomial of fourth degree,

$$\begin{aligned}\hat{\eta}_{\mathrm{tr,ts}} = &-0.0057225x_{\mathrm{ac},1}^4 - 0.19081x_{\mathrm{ac},1}^3x_{\mathrm{ac},2} + 0.49523x_{\mathrm{ac},1}^3 \\ &-1.2889x_{\mathrm{ac},1}^2x_{\mathrm{ac},2}^2 + 2.5406x_{\mathrm{ac},1}^2x_{\mathrm{ac},2} - 2.0352x_{\mathrm{ac},1}^2 \\ &-0.85368x_{\mathrm{ac},1}x_{\mathrm{ac},2}^3 + 3.9847x_{\mathrm{ac},1}x_{\mathrm{ac},2}^2 - 5.1624x_{\mathrm{ac},1}x_{\mathrm{ac},2} \\ &+7.214x_{\mathrm{ac},1} + 0.14738x_{\mathrm{ac},2}^4 + 1.7392x_{\mathrm{ac},2}^3 \\ &-5.2157x_{\mathrm{ac},2}^2 - 1.1701x_{\mathrm{ac},2} + 76.078.\end{aligned} \tag{3.22}$$

The regression is realized with an automated tool [33]. The large amount of terms allows the function to minimize the deviation in all the active subspace regions.

Table 3.3: Design space, constant parameters, and model outputs employed for the construction of the active subspace model

	ω	χ	P_{cr}	T_{cr}	σ	T_{ev}	R_s	$\alpha_{ge,1}$	$\beta_{ge,3}$	r_0/r_1	r_1/r_2	$\dot{W}_{tr,s}$	$\Omega_{e,s}$
	-	kg/mol	bar	°C	-	°C	-	°	°	-	-	kW	-
minimum	0.2657	0.0921	8.77	245.55	9.04	180	0.4	65	40	1.2	1.04	10	0.5
maximum	0.8250	0.4881	41.26	380.05	106.39	240	0.5	80	60	1.5	1.10	20	0.7
parameter number (i) in Fig. 3.6		1	2	3	4	5	6	7	8	9	10	11	12	13
	T_{cn}	ΔT_{sh}	t_{cl}	t_{te}	r_2/r_3	ϕ	ϑ_0	φ_0						
	°C	K	mm	mm	-	-	-	-						
constants	80.0	10	0.2	$0.1t_{to}$	2.0	0.3	0.7	0.4						
outputs	$\eta_{tr,ts}$	ϑ	w_3	α_2	β_3	b_0								

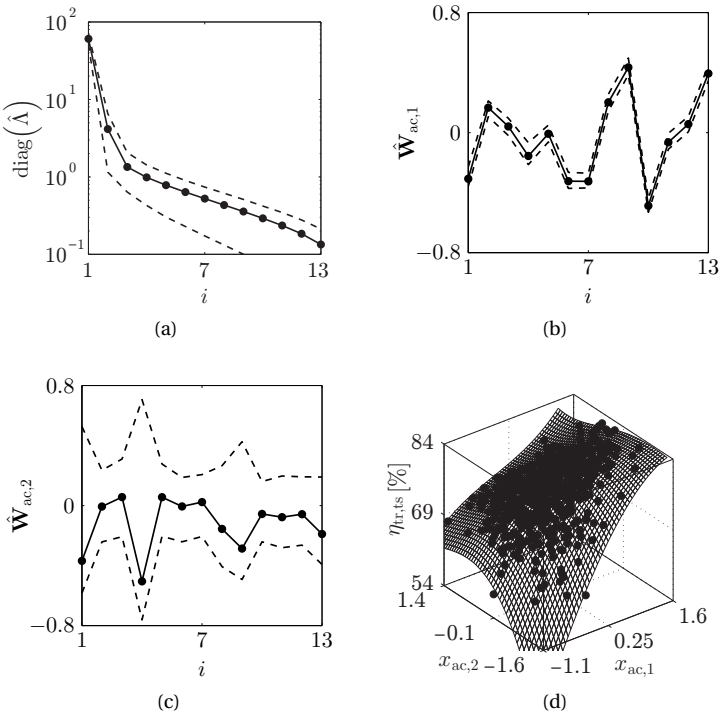

Figure 3.6: (a) Eigenvalues of $\hat{\mathbf{C}}$ associated with the total-to-static efficiency function computed with the combined fluid/turbine model. The dotted lines correspond to a 95 % bootstrap confidence interval computed with 10000 samples. (b) First active eigenvector. (c) Second active eigenvector. (d) Reduced-order response surface and samples (•). See Ref. [16] for information on bootstrapping. Table 3.3 lists the design variables.

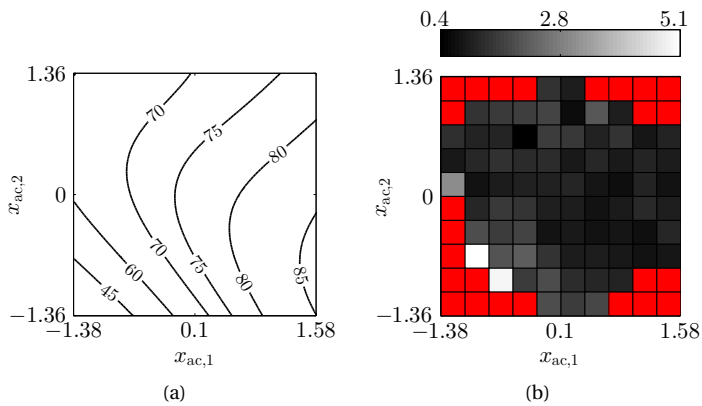

Figure 3.7: (a) Contour plot of the reduced-order response surface corresponding to the turbine total-to-static efficiency function. (b) Standard deviation of the surrogate.

RELEVANT DESIGN VARIABLES: RESPONSE SURFACE INTERPRETATION

The scalar values of the first eigenvector, shown in Figure 3.6b, are related to the global sensitivity of the efficiency to the design inputs. Accordingly, the most important turbine design parameters are the ratio of the stator inlet to outlet radii, the specific speed, and the rotor outlet blade angle. In order to interpret the two-dimensional response surface, Figure 3.8 displays these variables, and the total-to-static efficiency, as a function of the first active variable, and taking the second active variable equal to zero. The coordinates in Figure 3.8 are a result of averaging 1000 random samples per point, hence they represent general trends in the active subspace.

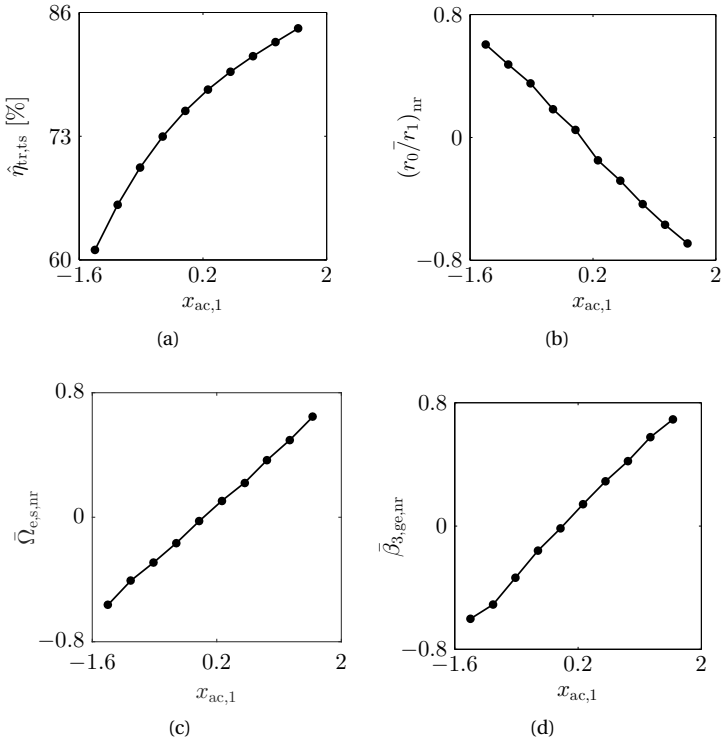

Figure 3.8: Total-to-static efficiency, and turbine-related normalized inputs as a function of the first active variable, and taking the second active variable equal to zero: (a) total-to-static efficiency, (b) stator aspect ratio, (c) rotor outlet blade angle, (d) isentropic specific speed. The plots are obtained with 1000 random samples per point.

Figure 3.8b shows the ratio of stator inlet to outlet radii. A lower value raises the turbine efficiency, because it reduces the end-wall area of the stator and the corresponding end-wall losses. The trend of the specific speed features a similar explanation (see Figure 3.8c): a higher value increases the stator aspect ratio, thus reducing secondary losses. A further advantage is the reduction of clearance losses. Finally, note in Figure 3.8d that a large rotor blade angle is beneficial, for it it reduces the leaving swirl and the corresponding rotor exit losses [8].

Figure 3.9 presents the corresponding charts for the most influential fluid model pa-

rameters: molar mass, acentric factor, and critical temperature. A higher molar mass increases the mass flow rate, the blade height, and the Reynolds number [34]. As a result, higher values improve the turbine efficiency by reducing scaling effects, see Figure 3.9a.

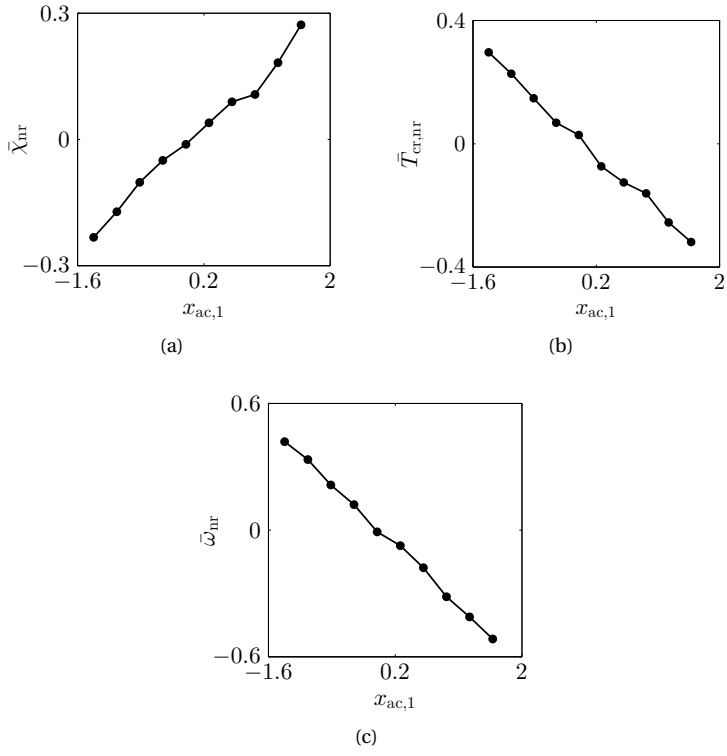

Figure 3.9: Fluid-related inputs as a function of the first active variable, and taking the second active variable equal to zero: (a) molar mass, (b) critical temperature, (c) acentric factor. The plots are constructed with 1000 random samples per point.

Figures 3.9b and 3.9c display the critical temperature and the acentric factor, respectively; they feature similar trends that are explained by analyzing the stator geometry. For given r_0/r_1 and r_1/r_2, the stator aspect ratio can be calculated as

$$\frac{b_0}{r_0 - r_1} = 2\left(\frac{r_0}{r_1}\frac{r_1}{r_2} - \frac{r_1}{r_2}\right)^{-1} \frac{b_0}{D_2} = K\frac{b_0}{D_2}, \tag{3.23}$$

where K is a constant. A lower critical temperature and acentric factor increase the saturation pressure and decrease the specific volume (e.g., see Fig. 3.10), thus reducing the blade height and the rotor inlet diameter, the latter computed with the volumetric flow at turbine outlet $\dot{m}v_{\mathrm{out,s}}$, see (3.10). However, the diameter decreases more rapidly, because the change of the specific volume $v_{\mathrm{out,s}}$ is steeper at lower pressures, e.g., see Fig. 3.11. Consequently, lower values of acentric factor and critical temperature increase the stator aspect ratio and decrease the secondary flows. Ultimately, the analysis of the response surface is an effective alternative to the conventional orthogonal sensitivity analysis, in order to rank the impact of the design parameters on the quantity of interest.

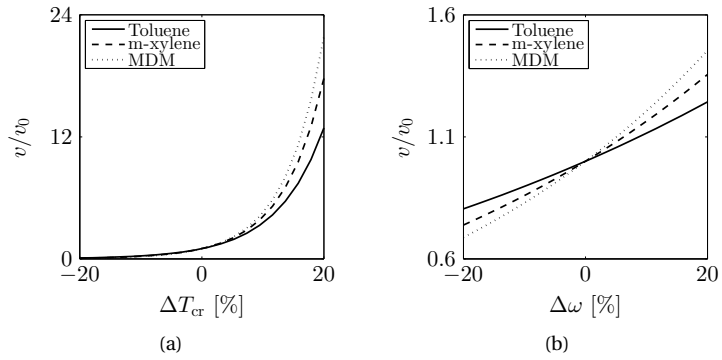

Figure 3.10: Change in saturated vapor specific volume as a function of (a) the critical temperature, and (b) the acentric factor, for three exemplary fluids. The specific volume values are computed with a saturation temperature of 80°C.

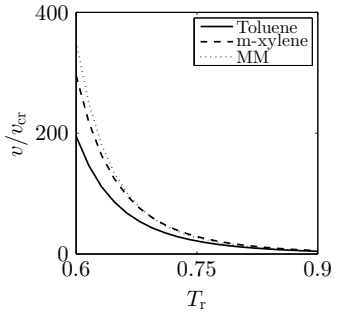

Figure 3.11: Ratio of saturated vapor specific volume to critical volume as a function of the reduced temperature, for three exemplary fluids.

3.3.2. APPLICATION OF THE SURROGATE MODEL - A TEST CASE

Table 3.4 presents the constraints employed in an exemplary optimization of a 10 kW turbine operating in a cycle with an evaporating temperature of 240°C. These restrictions originate from know-how on the design of radial inflow turbines [31], and considerations on manufacturing capabilities for the minimum blade height.

Table 3.4: Optimization constraints and constant parameters

ϑ	φ	w_3/w_2	b_0	$\dot{W}_{tr}$	T_{ev}
-	-	-	mm	kW	°C
≤ 0.7	≥ 0.4	≥ 1.5	≥ 1.5	$9 \leq \dot{W}_{tr} \leq 11$	240.0

The optimization procedure explained in Section 3.2.4 yields several solutions with similar efficiency and power, but with different working fluids and turbine specifications. It follows that, as already discussed in a previous work [15], the reduced-order model reunites all the multidimensional optima in a single active subspace region. As an example, Figure 3.12 presents the coordinates of three optima in the multidimensional space (3.12a),

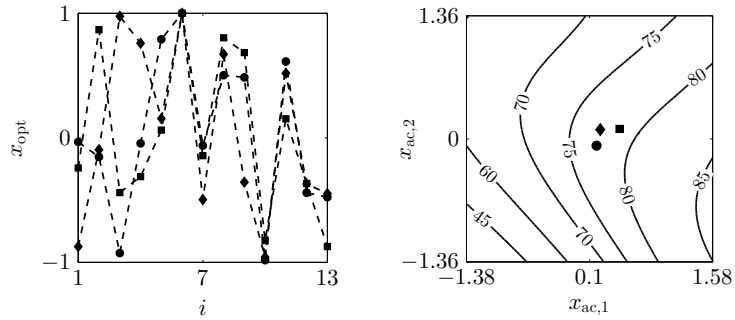

Figure 3.12: Solutions of the constrained optimization in (a) the multidimensional space, and in (b) a contour plot of the active subspace. (■) solution corresponding to PP_5.

and in the active subspace (3.12b). Note that the surrogate provides not only the efficiency of the turbine, but also the geometry of the machine and the parameters of the working fluid CEoS.

Figure 3.13 shows the main features of the optimal turbines. Since the three solutions feature three different working fluids, the size of the optimal turbines are different, as well as the rotational speed, and the pressure ratio. As a result, the distribution of the loss sources is different, yet the efficiency is the same because the optimal solutions are found in a small active subspace region.

Figure 3.14 displays thermodynamic cycles in the temperature-entropy diagram of the working fluid associated with the optimal turbine designs. The difference in the cycle thermal efficiency is mostly determined by the values of the critical temperature and molecular complexity of the working fluid [17]. In this case, all design options might be feasible. The selection of a particular solution must consider aspects related to turbine operation and geometry, and must also take into account other features, e.g., thermal efficiency, evaporating and condensing pressures, dimension and weight of the heat exchangers, etc..

One of the solutions in Figures 3.12, 3.13, and 3.14 is obtained by taking PP_5 as the working fluid. This component is selected because it features fluid parameters that are similar to those of the optima, thus proving that this method can be used to determine parameters of a non-existing fluid and possibly guide towards the synthesis of new chemicals, or to select existing ones. Alternatively, as demonstrated in the following section, it is possible to perform an optimization by predefining an already existing fluid in the design space.

3.3.3. PERFORMANCE OF THE SURROGATE MODEL

Figure 3.15 presents the results of a comparison between two optimization approaches: i) by means of a meanline code coupled with a genetic algorithm, and ii) by means of the active subspace model. In order to perform a fair comparison, the oversampling factor is taken equal to fifty for both methods. Additionally, PP_{90} is selected as the working fluid; the corresponding fluid parameters are then predefined in the design space.

The optimization is performed for three different temperature levels (180°C, 210°C, 240°C), and with the constraints reported in Table 3.4. Figure 3.15a depicts the optima provided by the active subspace model. Figure 3.15b illustrates the deviation between the

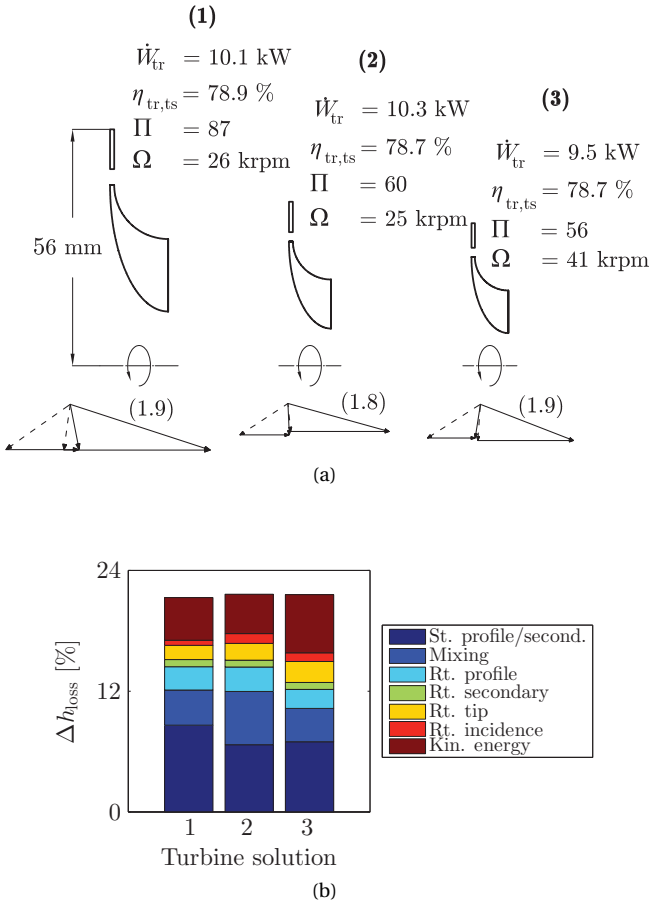

Figure 3.13: Solutions of the exemplary constrained design optimization problem: (a) turbine meridional channel and velocity triangles. The number in parenthesis above the velocity triangles correspond to the flow absolute Mach number at rotor inlet. (b) Turbine loss breakdown. Solution (2) is obtained with PP_5 as the working fluid. Design (1) and (3) correspond to turbines operating with non-existing fluids (the main fluid properties are shown in Fig.3.14.

results given by the surrogate and the genetic algorithm. This deviation is computed like a relative error where the result of the genetic algorithm is the reference.

The comparison of the computational time is shown in Figure 3.15c. The time referring to the active subspace optimization does not take into account the sampling. The optimization by means of active subspaces is at least two orders of magnitude faster than the conventional procedure based on the meanline code.

3.4. CONCLUDING REMARKS

This paper describes a new method to efficiently perform the integrated design of the turbine of power cycles operating with unconventional fluids, and its assessment. The preliminary design procedure integrates the selection of the working fluid, the calculation of the optimal thermodynamic cycle and the sizing of the corresponding optimal turbine. Such

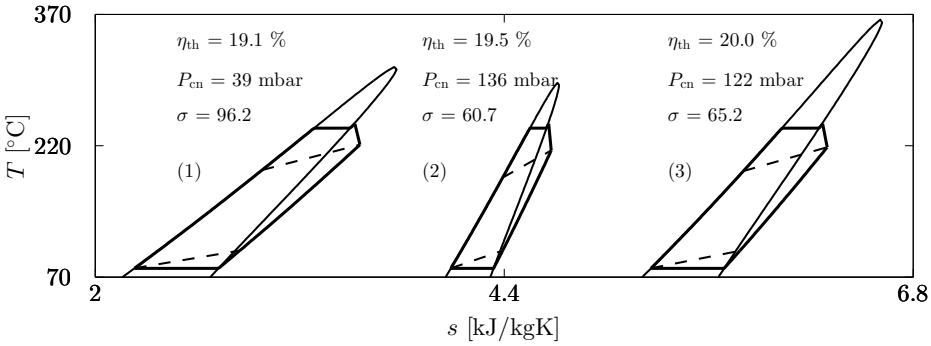

Figure 3.14: Solutions of the constrained optimization: temperature-entropy diagram of the thermodynamic cycle. Solution (2) is obtained with PP_5 as the working fluid. The regenerator pinch temperature is 20 K.

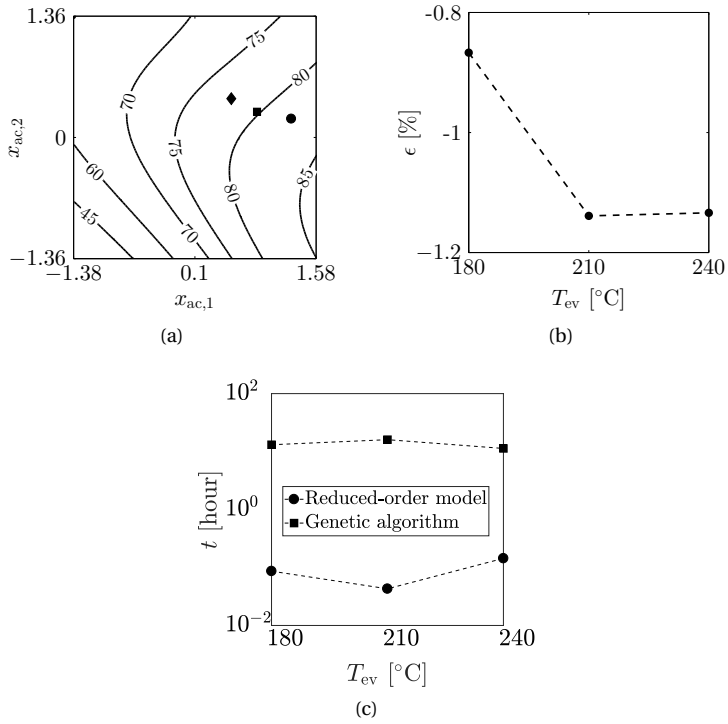

Figure 3.15: (a) Optimization results using the active subspace model and PP_{90} as the working fluid: (•) $T_{\text{ev}} = 180°\text{C}$, (■) $T_{\text{ev}} = 200°\text{C}$, (⧫) $T_{\text{ev}} = 240°\text{C}$. (b) Deviation between the results given by the surrogate and those given by the genetic algorithm. The deviation is computed like a relative error where the result of the genetic algorithm is the reference. (c) Optimization time, without taking into account the sampling time.

a complex mathematical problem has been solved with active subspaces, mathematical technique yielding a reduced order model that proved to be computationally efficient and robust.

The benefits of the method are demonstrated by its application to the design of a 10 kW *m*ORC unit for the exploitation of medium-temperature thermal sources, and adopting a single-stage radial inflow turbine. The application of the active subspaces to the turbine efficiency function leads to a reduced-order model constituted by two active variables. Similar results are also obtained for the other outputs of interest (e.g., blade height). Other advantages of the proposed method are:

- The method allows to restrict the search of the global optimum to a small region in terms of active variables. These solutions contain information regarding the turbine geometry, the working fluid parameters, and the thermodynamic cycle operating conditions. If the molecular parameters of the fluid do not correspond to an existing fluid, it can be speculated that further investigation might tell if the molecule can be synthesized.
- The surrogate-based optimization outperforms the standard design approach by providing optimal solutions with a computational cost which is at least two orders of magnitude lower.
- Once the surrogate is available, it can be used to solve any design problem within the boundaries employed to construct the surrogate. The surrogate requires negligible computational effort.
- The response surface can be used to infer which parameters and trends are dominant with respect to turbine performance. In the described example, the most influential design inputs are the stator inlet to outlet radius ratio, the specific speed, and the rotor outlet geometric angle. Likewise, the most important fluid model parameters are the molar mass, the critical temperature, and the acentric factor.

Future developments will include the addition of the preliminary design of the heat exchangers to the procedure. Therefore, it will be possible to evaluate other objective functions, e.g., system cost, weight, volume, etc.

ACKNOWLEDGMENTS

The authors are grateful to Bosch GmBH for funding the project that led to the results presented in this article, and for the fruitful discussions with Dr. Bernd Banzhaf of the division Diesel Systems, Engineering Component - Simulation and Testing; and Dr. Martin Dreizler of the division Corporate Sector Research and Advance Engineering, Future Mechanical and Fluid Components.

NOMENCLATURE

a	Equation of state parameter
a	Coefficients of the ideal gas heat capacity at constant pressure
b	blade height [mm]
c_P	Ideal gas heat capacity at constant pressure [kJ/kmol.K]
D	Diameter [mm]
h	Specific enthalpy [kJ/kg]
$\dot{m}$	Mass flow rate [kg/s]
P	Pressure [bar]
r	Radius [mm]
R	Gas constant [kJ/kmol·K]
s	Entropy [kJ/kg·K]
T	Temperature [°C]
t_{cl}	Tip clearance thickness [mm]
t_{te}	Trailing edge thickness [mm]
t	Time [hour]
U	Blade peripheral speed [m/s]
x_{ac}	Active variables
w	Relative flow velocity [m/s]
$\dot{W}$	Power [kW]

Greek symbols

ϵ	Error [%]
γ	Equation of state parameter
Φ	Pressure ratio
ϕ	Flow coefficient
ϑ_0	Radius ratio of the rotor outlet shroud to rotor inlet
φ_0	Radius ratio of the rotor outlet hub to shroud
Ω	Rotational speed [krpm]
Ω_e	Specific speed
Δ	Drop
ε	Equation of state parameter
τ	Equation of state parameter
η	Efficiency [%]
σ	Molecular complexity
χ	Molecular mass [kg/mol]
ω	Acentric factor
υ	Specific volume [m3/kg]
$\alpha_{1,ge}$	Stator outlet blade angle [°]
$\beta_{3,ge}$	Rotor outlet blade angle [°]

Subscripts

0..3	Turbine stage stations relative to Figure 3.3
ts	Total-to-static
sh	Superheating
cn	Condensation
ev	Evaporation
m	Meridional
in	Inlet
out	Outlet
s	Isentropic
cr	Critical
sv	Saturated vapor
r	Reduced

REFERENCES

[1] P. Colonna, E. Casati, C. Trapp, M. T., J. Larjola, T. Turunen-Saaresti, and A. Uusitalo, *Organic Rankine cycle power systems: from the concept to current technology, applications and an outlook to the future,* Journal of Engineering for Gas Turbines and Power **137**, 100801 (2015).

[2] W. Lang, P. Colonna, and R. Almbauer, *Assessment of waste heat recovery from a heavy-duty truck engine by means of an ORC turbogenerator,* Journal of Engineering for Gas Turbines and Power **135**, 042313 (2013).

[3] C. Perullo, D. Mavris, and E. Fonseca, *An integrated assessment of an organic Rankine cycle concept for use in onboard aircraft power generation,* in *ASME Turbo Expo*, GT2013-95734 (2013) p. 8.

[4] M. E. Mondejar, F. Ahlgren, M. Thern, and M. Genrup, *Quasi-steady state simulation of an organic Rankine cycle for waste heat recovery in a passenger vessel,* Applied Energy **185, Part 2**, 1324 (2017).

[5] C. De Servi, L. Azzini, M. Pini, A. G. Rao, and P. Colonna, *Exploratory assessment of a combined-cycle engine concept for aircraft propulsion,* in *Proceedings of the 1st Global Power and Propulsion Forum - GPPF2017*, GPPF-2017-78 (2017) p. 11.

[6] S. Bahamonde, M. Pini, C. De Servi, and P. Colonna, *Method for the preliminary fluid dynamic design of high-temperature mini-ORC turbines,* Journal of Engineering for Gas Turbines and Power **139**, 082606 (2017).

[7] E. Macchi and A. Perdichizzi, *Efficiency prediction for axial-flow turbines operating with nonconventional fluids,* Journal of Engineering for Power **103**, 718 (1981).

[8] A. Perdichizzi, *Design criteria and efficiency prediction for radial inflow turbines,* in *ASME Turbo Expo*, 87-GT-231 (1987) p. 9.

[9] A. Toffolo, A. Lazzaretto, G. Manente, and M. Paci, *A multi-criteria approach for the optimal selection of working fluid and design parameters in organic Rankine cycle systems,* Applied Energy **121**, 219 (2014).

[10] D. Maraver, J. Royo, V. Lemort, and S. Quoilin, *Systematic optimization of subcritical and transcritical organic Rankine cycles (ORCs) constrained by technical parameters in multiple applications,* Applied Energy **117**, 11 (2014).

[11] A. Pezzuolo, A. Benato, A. Stoppato, and A. Mirandola, *The ORC-PD: A versatile tool for fluid selection and organic Rankine cycle unit design,* Energy **102**, 605 (2016).

[12] E. Casati, S. Vitale, M. Pini, G. Persico, and P. Colonna, *Centrifugal turbines for mini-organic Rankine cycle power systems,* Journal of Engineering for Gas Turbines and Power **136**, 122607 (2014).

[13] M. Erbas and A. Biyikoglu, *Design and multi-objective optimization of organic Rankine turbine,* International Journal of Hydrogen Energy **40**, 15343 (2015), the 4th International Conference on Nuclear and Renewable Energy Resources (NURER2014), 26-29 October 2014, Antalya, Turkey.

[14] A. La Seta, A. Meroni, J. G. Andreasen, L. Pierobon, G. Persico, and F. Haglind, *Combined turbine and cycle optimization for organic Rankine cycle power systems – part B: Application on a case study,* Energies **9**, 393 (2016).

[15] S. Bahamonde, M. Pini, and P. Colonna, *Active subspaces for the preliminary fluid dynamic design of unconventional turbomachinery,* in *European Congress on Computational Methods in Applied Sciences and Engineering*, 7806, edited by M. Papadrakakis, V. Papadopoulos, G. Stefanou, and V. Plevris (2016) p. 15.

[16] P. G. Constantine, *Active Subspaces: Emerging Ideas for Dimension Reduction in Parameter Studies* (SIAM-Society for Industrial and Applied Mathematics, 2015).

[17] G. Angelino, C. Invernizzi, and E. Macchi, *Organic working fluid optimization for space power cycles,* (Springer-Verlag, Berlin, 1991) Chap. 16, pp. 297–326.

[18] G. Angelino and C. Invernizzi, *Cyclic methylsiloxanes as working fluids for space power cycles,* Journal of Solar Energy Engineering **115**, 130 (1993).

[19] E. W. Lemmon, M. Huber, and M. O. McLinden, *NIST standard reference database 23: Reference fluid thermodynamic and transport properties-REFPROP, version 9.1,* (2013), national Institute of Standards and Technology, Gaithersburg.

[20] P. Colonna, T. P. van der Stelt, and A. Guardone, *FluidProp (Version 3.0): A program for the estimation of thermophysical properties of fluids,* (2012), Asimptote bv.

[21] C. M. Invernizzi, *Closed Power Cycles*, Lecture Notes in Energy, Vol. 11 (Springer-Verlag, London, 2013).

[22] A. Head, C. De Servi, E. Casati, M. Pini, and P. Colonna, *Preliminary design of the ORCHID: A facility for studying non-ideal compressible fluid dynamics and testing ORC expanders,* in *ASME Turbo Expo*, Vol. 3 (2016) p. 14.

[23] Various Authors, *Matlab version 8.2.0.701 (r2013b),* (2013), the MathWorks Inc.

[24] M. Pini, G. Persico, E. Casati, and V. Dossena, *Preliminary design of a centrifugal turbine for organic Rankine cycle applications,* Journal of Engineering for Gas Turbines and Power **135**, 042312 (2013).

[25] J. M. Smith, H. C. Van Ness, and M. M. Abbot, *Introduction to Chemical Engineering Thermodynamics*, 7th ed. (McGraw-Hill Education, New York, 2005).

[26] J. D. van der Waals, *The equation of state for gases and liquids,* in *Nobel Lectures, Physics 1901-1921* (Elsevier Publishing Company, Amsterdam, 1967) pp. 254–265.

[27] O. Redlich and J. N. S. Kwong, *On the thermodynamics of solutions. V. An equation of state. Fugacities of gaseous solutions.* Chemical Reviews **44**, 233 (1949).

[28] D. Y. Peng and D. B. Robinson, *A new two-constant equation of state,* Ind. Eng. Chem., Fundam. **15**, 59 (1976).

[29] G. Soave, *Equilibrium constants from a modified Redlich-Kwong equation of state,* Chemical Engineering Science **27**, 1197 (1972).

[30] W. C. Reynolds and P. Colonna, *Vapor power plants,* in *Thermodynamics* (Cambridge University Press, 2018) Chap. 7, in Press.

[31] S. Dixon and C. Hall, *Fluid Mechanics and Thermodynamics of Turbomachinery*, 6th ed., edited by S. Dixon and C. Hall (Butterworth-Heinemann, Boston, MA, 2010).

[32] P. Constantine, E. Dow, and Q. Wang, *Active subspaces method in theory and practice: applications to kriging surfaces,* SIAM Journal on Scientific Computing **36**, A1500 (2014).

[33] J. D'Errico, *Polyfitn - polynomial modeling in 1 or n dimensions,* (2012), MATLAB Central File Exchange. Retrieved March, 2014.

[34] H. Tabor and L. Bronicki, *Establishing criteria for fluids for small vapor turbines, SAE National Transportation, Powerplant, and Fuels and Lubricants Meeting*, SAE Technical Paper **640823**, 561 (1964).

4

HYBRID ELECTRIC POWERTRAIN FOR LONG-HAUL TRUCKS AND BUSES: PRELIMINARY ANALYSIS OF A NEW CONCEPT BASED ON A COMBINED CYCLE POWER PLANT

The contents of this chapter are based on:

S. Bahamonde, C. De Servi, and P. Colonna, *Hybrid Electric Powertrain for Long-haul Trucks and Buses: Preliminary Analysis of a New Concept Based on a Combined Cycle Power Plant*, Proceedings of the Global Power & Propulsion Forum, GPPS-NA-2018-137 (2018).

The electric hybridization of heavy-duty road vehicles is a promising alternative to reduce the environmental impact of freight and passengers transportation. Employing a micro gas turbine as a prime mover presents several advantages: high power density, fuel flexibility, ultra-low emissions, low vibrations and noise, simplicity and lower maintenance and operational cost. State-of-the-art micro gas turbines feature a thermal efficiency of 30 %*, which can be increased to* 40 % *by employing a mini organic Rankine cycle system for waste heat recovery. This work presents an exploratory analysis of the performance of a hybrid electric heavy-duty vehicle with a prime mover based on this concept.*

The assessment is done in two steps: preliminary design of the combined cycle power plant, and estimation of the vehicle fuel economy and emissions over a representative driving cycle. One of the most promising simulated solutions is based on a combined cycle system featuring a peak thermal efficiency of 0.44*, and a nominal power output of about* 150 kW*. This corresponds to the power demand at cruise condition of a long-haul truck (weight approx. 36 ton). A series configuration with Lithium-Ion batteries is selected for the hybrid powertrain, for it decouples the prime mover dynamics from the power demand. The benchmark is a vehicle featuring a next generation diesel engine, with a peak efficiency equal to* 50 %*.*

The results show that the fuel economy can be largely improved by increasing the size of the battery in the hybrid powertrain. Furthermore, employing natural gas in the prime mover of the hybrid vehicle leads to ultra low emissions that are well below the European and north American regulations, without the need of exhaust gas aftertreatment. Additionally, the CO_2 *emissions of the hybrid powertrain are considerably lower than that of the benchmark. This work thus demonstrates the relevant potential of this hybrid powertrain, especially in terms of exhaust emissions.*

4.1. INTRODUCTION

Heavy-duty road transport produces approximately 5% of the European Union's total greenhouse gas emissions, contributing more than international shipping and aviation to the total CO_2 release in the atmosphere [1]. The electric hybridization of the power train is a promising option to improve the fuel economy and reduce emissions. It makes it possible to downsize the combustion engine, to recover energy during deceleration, to continuously operate the engine under optimum conditions, and to eliminate idle fuel consumption and clutching losses [2]. A hybrid electric power train is particularly suited for long-haul trucks (class 8, weight > 15 ton, US standards [3]) and buses. They travel for long distances, their current autonomy range cannot be arguably reached by a fully electric power train without significant penalties in payload, due to the insufficient energy density of current and near-future electric batteries [4]. Furthermore, these vehicles operate in stable cruise conditions for many hours, hence the power plant and its control can be optimized for constant on-design operation allowing for higher efficiency and lower emissions. Several companies have been and are thus developing heavy-duty hybrid power trains with prime movers like reciprocating engines [5], fuel cells [6], and micro gas turbines [7].

The use of a gas turbine for road propulsion presents some potential merits: high power density, fuel flexibility, ultra-low emissions, low vibrations and noise, simplicity and lower maintenance and operational cost. This concept was already studied decades ago. Even though commercial organizations realized prototypes of heavy-duty trucks and passenger cars, gas turbine powered vehicles were not introduced into the market, mainly due to the poor efficiency micro/mini gas turbines, especially in off-design conditions [8]. This prob-

lem does not occur if the gas turbine is part of a hybrid configuration, for the machine can always run at optimal conditions independently from the vehicle speed and gear position. Moreover, by employing a bottoming organic Rankine cycle (ORC) system, it is possible to increase the efficiency of micro gas turbines (μGT, power output < 500 kW) to 40% [9]. Note also that recovering waste energy from a single high-temperature source in a μGT is easier than from a Diesel engine, for which the full recovery potential can only be achieved if also the low-temperature energy content of the cooling and lubrication system is employed.

This paper presents an analysis of a hybrid power train for a class 8 truck employing a combined cycle with a μGTand a mini ORC system (mORC, power output < 50 kW). The assessment of the proposed power train concept is performed in two steps. The first one deals with the preliminary design and performance assessment of the combined cycle (CC) power plant, while the second focuses on the vehicle fuel economy over a representative mission. The preliminary design considers recuperative and non-recuperative cycle configurations, and the working fluids for the mORC are selected taking into account performance, manufacturing constraints typical of small scale turbomachinery, safety and environmental aspects. The design of the heat exchangers is performed with a well-known engineering software [10], and it takes into account constraints on weight and volume given by the vehicle architecture. The estimated characteristics of the CC gen-set are then used for the assessment of the fuel economy of a hybrid electric long-haul truck at full load (weight approx. 36 ton); this analysis is performed with an open source library for quasi-steady-state simulations [11]. A series configuration with Lithium-Ion batteries is selected for the hybrid powertrain, because it decouples the prime mover dynamics from that of the vehicle [2].

The objective of the analysis is to evaluate the trade-off between the size of the batteries and the cargo weight and fuel economy, and also to estimate the flue gas emissions if natural gas is employed.

4.2. METHOD

The preliminary design of the CC system has been carried out using a general-purpose open source programming software [12], while for the following analysis an open-source library developed with a proprietary software for system simulations was employed [11, 13]. Values of fluid thermophysical properties were estimated by means of state-of-the-art software libraries implementing a wide variety of models [14, 15]

4.2.1. PRELIMINARY DESIGN OF THE COMBINED CYCLE

A parametric study was performed to select the optimum gas turbine inlet temperature. As a result, three cycle configurations, with three different temperature levels have been chosen. Figure 4.1 presents the corresponding process flow diagrams.

Figure 1a shows the RGT-ORC configuration, based on a state-of-the-art μGTturbine operating with a low pressure ratio of four, a maximum turbine inlet temperature approaching 1000°C, and a gas-to-gas recuperator with a maximum inlet temperature of approximately 650°C [16]. Regarding the ORC system, a preliminary thermodynamic analysis showed that regeneration has little effect on the overall efficiency. Additionally, the water in the flue gas might partially condense in the primary heat exchanger of the ORC unit. Condensation in the stack has therefore been modeled following the procedure reported by by Lu *et al.* [17].

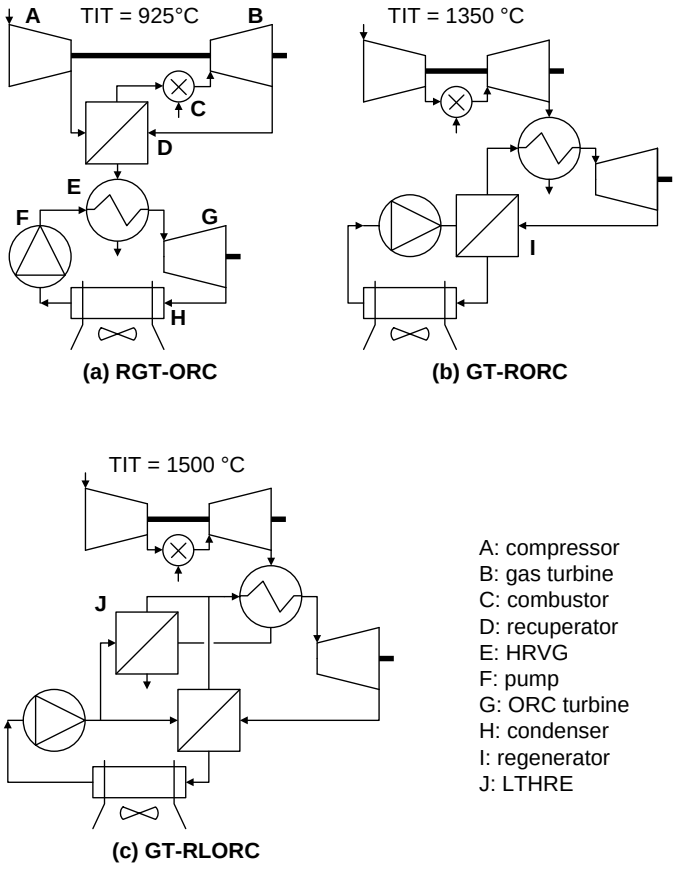

Figure 4.1: Process flow diagrams of the studied combined cycle systems. HRVG: heat recovery vapor generator. LTHRE: low-temperature heat recovery exchanger.

The CC configuration in Figure 1b presents a combined cycle with a non-recuperative gas turbine (GT-RORC). In this case, in order to achieve a sufficiently high thermal efficiency, the turbine inlet temperature must have a value that is not attainable with uncooled blades. An alternative is to employ a ceramic machine, which has been tested in the past with a maximum temperature of 1350°C [18]. The potential of this type of technology is still under scrutiny, as shown by recent research projects on micro ceramic gas turbines for unmanned air vehicles [19]. For this cycle configuration, the preliminary thermodynamic analysis showed that the best performance is achieved with a regenerator in the bottoming cycle.

Figure 1c shows the configuration GT-RLORC, a non-recuperative gas turbine with a bottoming cycle employing an additional (low temperature) heat recovery exchanger (LTHRE). In this case, the flow leaving the pump in the bottoming cycle is split, in order to obtain a very good match between the temperature profiles of the hot and cold stream in the regenerator. The bypassed liquid flow is then preheated by the exhaust gases after the HRVG, thus enhancing the amount of thermal energy recuperated. This system also

requires a high gas turbine inlet temperature, to reach a high conversion efficiency. Here, instead of a ceramic turbine, film blade cooling is considered [20]. It could be then possible to raise the turbine inlet temperature to values as high as 1500°C (like in modern gas turbines). The impact of film cooling on the thermodynamic cycle efficiency is taken into account according to the modeling method proposed by Horlock [21], and assuming a four stage machine with cooling at the inlet of the first two stages.

A thermodynamic cycle analysis is used to determine the optimal cycle specifications, which are then used to design the turbomachinery and the heat exchangers. The procedure can be consulted in any engineering Thermodynamics textbook, see, e.g., Reynolds and Colonna [22], or Moran *et al.* [23]; thus, it is not reported here. A degree of freedom of these CC configurations is the ORC condensing temperature. Its value is determined following the calculation procedure described in the following section

DETERMINATION OF THE ORC CONDENSATION TEMPERATURE

The geometry of the ORC condenser is assumed of the plate-fin and tube type, like that of ICE radiators, with louvered-fins for the air side, and a single-pass flat tubes for the working fluid side, see Fig. 4.2a. The condenser can be installed in front of the vehicle and its size is taken equal to that of a typical radiator on board of long-haul trucks. Therefore, the frontal area and the aerodynamic performance of both the hybrid electric vehicle and a conventional vehicle can be considered equal.

In order to obtain the condensing temperature, the thermodynamic cycle analysis of the candidate CC configurations is run with condensing temperatures varying between 50°C and 80°C. This allows to estimate the condenser operating conditions (working fluid mass flow rate, and inlet/outlet thermodynamic states) which are required as inputs to a rating model of the heat exchanger. The model outputs are the specified air mass flow rate and the corresponding pressure drop. The condensing temperature is then the minimum value whereby the calculated pressure loss is equal to the dynamic pressure of the air stream entering the radiator at cruise speed, thus guaranteeing that the radiator can operate solely with such stream (or *ram* air).

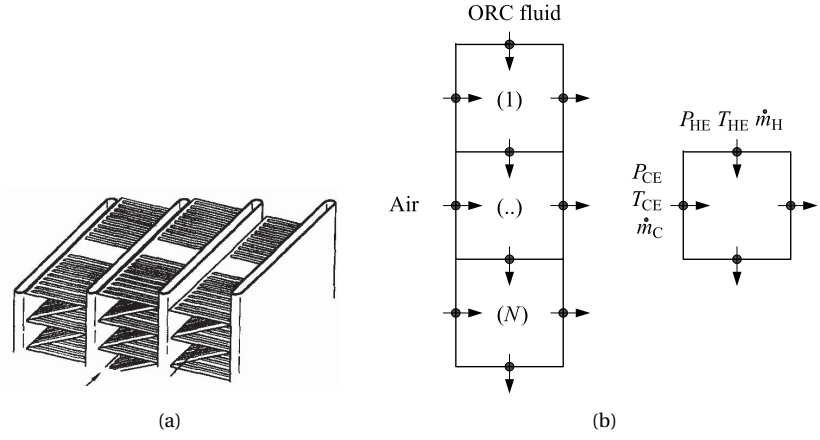

Figure 4.2: a) Louver fin with triangular channel [24]. b) Scheme of the one-dimensional discretization.

The rating model of the condenser is based on a one-dimensional discretization of the

geometry, as illustrated in Figure 4.2b. Mass, energy and momentum balances are evaluated at each cell. Details of the solution strategy can be consulted in the book of Shah and Sekulić [25].The overall heat transfer coefficient, assuming negligible fouling, reads

$$\frac{1}{UA} = \frac{1}{(\eta_o \chi A)_{\mathrm{H}}} + R_{\mathrm{W}} + \frac{1}{(\eta_o \chi A)_{\mathrm{C}}}, \tag{4.1}$$

where η_o is the fin efficiency, χ is the fluid heat transfer coefficient, A is the heat transfer area, and R_{W} is the wall resistance. The subscripts H and C correspond to hot and cold side, respectively.

Following the various assumptions listed by Shah and Sekulić [25], and neglecting the momentum effect, the hot and cold side single-phase pressure drop are computed as

$$\Delta P = \frac{G^2}{2}\left[\frac{1-\sigma^2+K_i}{\rho_i} + f\frac{L}{r_h}\rho_i\frac{1}{2}\left(\frac{1}{\rho_i}+\frac{1}{\rho_o}\right) - \frac{1-\sigma^2-K_o}{\rho_o}\right] \tag{4.2}$$

were G is the mass flux, ρ_i is the inlet density, ρ_o is the outlet density, f is the Fanning friction factor, σ is the ratio of core minimum free-flow area to frontal area. K_i and K_o are entrance and exit pressure loss coefficients defined by Kays and London [26], their value has been computed assuming a multiple-tube flat-tube core on the hot side, and a multiple triangular tube core on the cold side.

The correlations for the Colburn and Fanning friction factor of the air side are those for a louvered fin geometry developed by Chang and Wang [24] and Chang *et al.* [27]. For the hot side, the Nusselt number and Fanning friction factor are computed with the correlations for flat tubes developed by Spiga and Dall'Olio [28] under laminar flow conditions, while the correlations of Gnielinski [29] are used for turbulent regime. According to the recommendation of Hesselgreaves [30], the heat transfer coefficient for a condensing flow is computed with the multiplication factor introduced by Taylor [31]. The two-phase friction factor coefficient is obtained with the method of Lockart and Martinelli [32]. The fin efficiency for the air side is that of a louver fin [25]. Finally, the wall resistance (flat tube wall) is computed assuming a flat plate geometry.

The method has been successfully validated with the work of Yadav *et al.* [33].

TURBOMACHINERY MEANLINE DESIGN

The thermodynamic cycle analysis provides the inputs for the design of the turbines. This task is performed with an in-house meanline code [34, 35]. The loss models implemented in this software are listed in the work of Bahamonde *et al.* [36]. The program has been validated with conventional test cases, i.e., turbines operating with ideal-gas fluids, large Reynolds numbers, and subsonic flows. Efforts are currently underway to perform the validation with *m*ORC machines [37, 38]. The design of compressors and pumps, the effect of blade film cooling, and the effect of leakage and windage losses on turbine efficiency, will be addressed in future studies.

PRELIMINARY DESIGN OF THE HEAT EXCHANGERS

Plate-fin exchangers are selected, because they are a mature technology that has been widely used in industry for decades (including in automotive and aerospace applications). Their manufacturing process allows for the use of different metals that can operate under temperatures up to 840°C, which can be increased to 1150°C by employing ceramic materials [25]. Besides, they were selected for several prototypes of high temperature ceramic μGT [18]. A commercial software is employed for their design [10].

4.2.2. ANALYSIS OF THE FUEL ECONOMY FOR A HEAVY-DUTY TRUCK

The analysis is done with an open source toolbox for quasi-steady-state simulations originally developed for passenger vehicles [11]. Figure 4.3 displays a flow diagram of the simulation programs, with the connections of their quasi-steady-state model components developed to evaluate the two long-haul truck configurations studied here: 4.3a) a conventional vehicle (CV) powered by a reciprocating engine operating with Diesel, and 4.3b) a hybrid-electric vehicle (HEV). For a detailed explanation on how to model and simulate hybrid and non-hybrid vehicles the reader is referred to the work of Guzzella and Sciarretta [2]. The weight of the CC system is an input for the analysis of the fuel economy. As a first approximation, the CC-engine weight is taken equal to the weight of the heat exchangers.

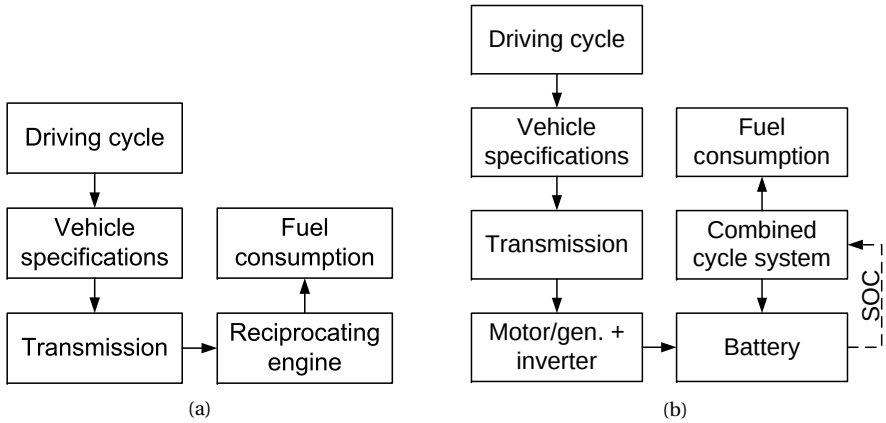

Figure 4.3: Process flow diagram of the simulations, with the connections of their quasi-steady-state model components: a) a vehicle employing a diesel reciprocating engine, and b) a series hybrid electric vehicle with the combined cycle system.

In order to analyze the CV performance, components from the library have been modified to create two new models: a heavy-duty gearbox for the transmission, and a 320 kW reciprocating engine with its corresponding performance map. The required information has been obtained from an open-source database [39], and it corresponds to a Kenworth T800 truck powered by a Caterpillar C15 engine.

The powertrain configuration selected for this preliminary analysis of a HEV is of the series type. In this configuration, the gas turbine and the ORC system always run under optimal conditions independently from the power demand. For this simulation, several models have been developed:

- a lithium-ion battery, whose charge/discharge curves are obtained from a commercial manufacturer [40]. The specific weight and power have been adjusted, to reflect recent estimations on the characteristics of state-of-art batteries for automotive applications [41].

- A 320 kW electric motor/inverter, whose performance maps have been obtained by linearly scaling those from a 220 kW machine [42]. The regenerative braking power is computed by mirroring the torque-rotational speed efficiency map.

- The CC power plant. The start-up and the shut-down of the CC unit is controlled based on the state-of-charge of the batteries. The startup time and the corresponding energy consumption are not considered in the calculation of the HEV fuel economy; they will be studied in future stages of this research program.

The fuel economy or trucking efficiency is evaluated in ton-cargo·km/kg-fuel. This measurement unit takes into account the payload, thus it is a more appropriate figure of merit for the comparison of the performance of different truck configurations than the specific fuel consumption per driven kilometer [43].

The energy to charge the batteries might come from many different sources. In order to simplify this first analysis, it is assumed that the energy required to charge the batteries comes from renewable energy with negligible emissions and zero fossil-fuel consumption.

HEV CONTROL STRATEGY

For missions characterized by long periods at constant speed, an on/off control strategy of the generator is appropriate [44]. The CC system is thus started or stopped if the battery state-of-charge exceeds predefined limits: 90% for the shut-down and 10% for the start-up. To calculate the fuel consumption of the HEV, it is assumed that the battery is discharged in a single cycle and the state-of-charge reaches 10% when the driving mission ends. Furthermore, the combined cycle power plant operates only when the truck is cruising. It follows that the ram air is always sufficient for the condensation of the working fluid of the ORC system, thus no fan is required.

As a first approximation, the energy consumption related to power plant startup and shutdown is neglected. Such approximation has arguably no effect on the results of this work, because the driving cycle lasts hours, while the startup/shutdown operations last minutes [45].

ESTIMATION OF THE EMMISIONS

The HEV emissions are approximated assuming that the gas turbine operates with natural gas. However, gas turbines running on diesel and achieving very low emission levels are also available [46]. The estimation of CO, HC, NO_x, and PM (particular matter) is based on fuel-to-emission conversion factors issued by a gas turbine commercial manufacturer [47]. These coefficients are kept constant for the simulation of the entire driving cycle, because gas turbine is assumed to operate always at design conditions, thus neglecting the startup and shutdown phases. The emissions per unit energy are then compared against the current limits for heavy-duty vehicles imposed by the United States Environmental Protection Agency (EPA) [48], and by the European Union (EURO-VI) [49].

The CO_2 emissions from the HEV can be computed by using the flue gas composition shown in Table 4.1. The CO_2 discharge from the conventional vehicle is computed assuming an average chemical formula for diesel fuel, namely $C_{12}H_{24}$ [50].

4.3. APPLICATION AND RESULTS

4.3.1. PRELIMINARY DESIGN OF THE COMBINED CYCLE

Table 4.1 presents the model parameters considered for the thermodynamic cycle analysis. The CC nominal power output is taken equal to the mechanical power required at cruise conditions, as suggested by Ehsani *et al.* [44]. For a fully loaded long-haul truck (weight

Table 4.1: Parameters for the thermodynamic cycle analysis

General parameters		
Net power output	kW	150
Environmental pressure	bar	1.01
Environmental temperature	°C	15
Mechanical (bearing) efficiency	-	0.98
Brayton cycle		
Combustor efficiency	-	0.999
Air composition	-	N_2(0.7729) H_2O(0.0101) Ar(0.0092) CO_2(0.0003) O_2(0.2075)
Flue gas composition	-	N_2(0.7049) H_2O(0.1919) Ar(0.0082) CO_2(0.095)
Maximum temperature	°C	925[1] / 1350[2] / 1500[3]
Turbine polytropic efficiency	-	0.84
Compressor polytropic efficiency	-	0.79
Recuperator effectiveness	-	0.87
Total pressure loss	%	5.0
HRVG pinch	K	10
Rankine cycle		
Working fluid	-	cyclopentane[1] / toluene[2,3]
Maximum temperature	°C	255[1] / 400[2,3]
Turbine isentropic efficiency	-	0.80
Pump isentropic efficiency	-	0.60
Regenerator pinch	K	20
P. loss, regeneration and evaporation	%	1.0
P. loss, regeneration and condensation	bar	0.1
Maximum reduced evaporating P.	-	1.1
Turbine max. vol. expansion ratio	-	60

[1] RGT-ORC, [2] GT-RORC, [3] GT-RLORC

circa 36, according to the limits in the the U.S. roadways), trial computations showed that this power is approximately 150 kW.

As far as the μGT model is concerned, the mechanical and combustor efficiency, and the recuperator effectiveness are taken from Ref. [16]. As shown in that Table 4.1, the total Brayton cycle pressure loss is taken as a fraction of the maximum cycle pressure. The pressure losses are attributed to the various components according to Ref. [16].

The Brayton cycle maximum temperature varies according to the CC-genset configuration under study: a) the RGT-ORC configuration features a turbine inlet temperature of 925°C. Higher values would result in temperatures at the hot side of the Brayton cycle recuperator exceeding the limit of 650°C, and would thus require special and expensive materials. b) the turbine inlet temperature of the GT-RORC configuration is assumed to be 1350°C, which corresponds to the maximum temperature arguably achievable by ceramic turbines. c) the GT-RLORC configuration has a turbine inlet temperature of 1500°C, a value typical of a state-of-the-art gas turbine with blade cooling. The turbine and compressor polytropic efficiencies are taken from the work of Massardo *et al.* [51].

The selection of the ORC working fluid for the GT-RORC and GT-RLORC configurations is done as follows. These power plants have a gas turbine outlet temperature higher than 600°C, see Fig. 4.5. It is thus desirable to select an organic fluid with high thermal stability, in order to minimize the thermodynamic losses associated with heat transfer in the HRVG. Toluene is arguably the best candidate: it can operate at temperatures as high as 400°C [52],

and it leads to a comparatively high thermodynamic cycle efficiency, for it features a relatively low molecular complexity [9]. On the contrary, as far as the RGT-ORC configuration is concerned, the maximum temperature in the heat recovery vapor generator is around 300°C. In this case, various fluids were tested. Ultimately, cyclopentane allows to achieve the best performance. Its estimated maximum temperature is 255°C, which is a value that incorporates a safety margin with respect to its predicted thermal stability limit in contact with stainless steel [52].

The values of the ORC model parameters follow common practice for such systems, see, e.g., Refs. [36] and [37]. In particular, the maximum reduced evaporating pressure is 1.1, because larger values have little effect on the cycle thermodynamic efficiency. Moreover, the maximum turbine volumetric expansion ratio is set to 60. Although such a value my seem too large for a single-stage RIT, the operation of commercial high-temperature 150 kW ORC turbines [53], and a detailed recent numerical study, describing the design of a 10 kW ORC radial inflow expander, supports this assumption [38].

ORC CONDENSING TEMPERATURE

The length, width, and depth assumed for the plate-fin condenser correspond to those of the radiator installed on a Kenworth T800 heavy-duty truck [54]. The louvered fin and plate geometric patterns are obtained from the work of Yadav *et al.* [33].

Figure 4.4 shows the results of the condenser rating model for several condensing temperatures between 50°C and 80°C, and obtained using the parameters introduced in Table 4.1. The estimated performance of the combined cycle power plant has been optimized

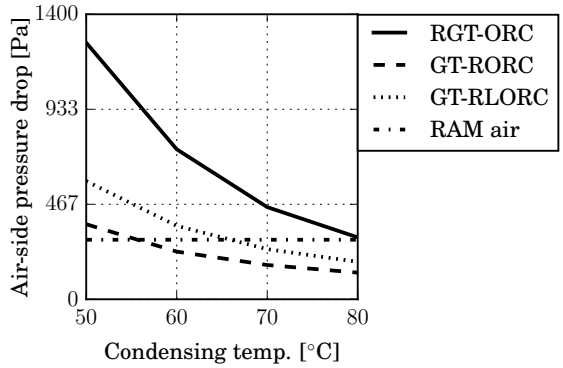

(a)

Figure 4.4: Radiator air-side pressure drop as a function of the condensing temperature.

by tuning the maximum cycle pressure of both the μGTand mORC unit. The condensing temperature results from imposing that the air side pressure drop is equal than the air dynamic pressure for a cruising speed of 85 km/h. Thus, according to Fig. 4.4, the condensing temperature values for each cycle configuration are: 80°C for RGT-ORC, 60°C for GT-RORC, and 70°C for GT-RLORC. These values may seem high. However, recall that typically truck radiators operate with water at approximately 85°C. This analysis has been done assuming an environmental temperature of 15°C. Future work should consider the effects of ambient conditions (e.g., higher temperature values) and possibly other solutions and further

optimization, as a lower condensing temperature considerably increases the efficiency of the power plant.

THERMODYNAMIC CYCLE ANALYSIS

Figure 4.5a shows the variation of the calculated efficiency of three CC power plant configurations under study as a function of the Brayton cycle maximum pressure, assuming the ORC condensing temperatures indicated in previously; Figure 4.6 presents the cycle specifications for the thermodynamic cycles exhibiting the highest performance and the corresponding temperature-entropy diagrams.

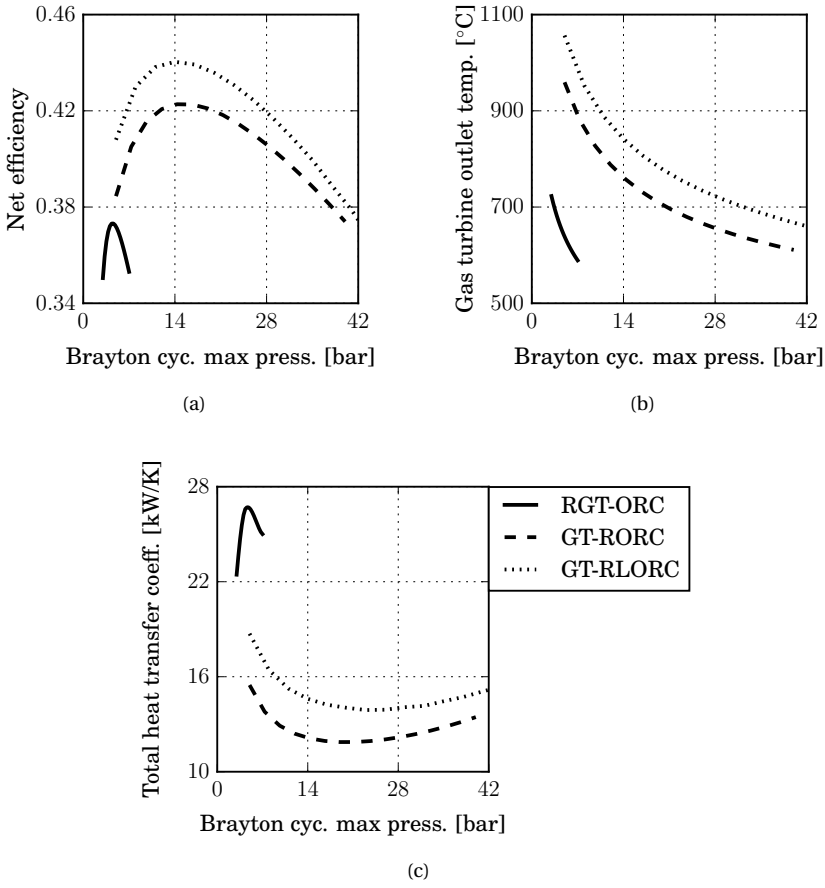

Figure 4.5: Thermodynamic cycle analysis: a) net efficiency, b) gas turbine outlet temperature, c) exchangers heat transfer coefficient. The cycle parameters are listed in Table 4.1.

From Figure 4.5 it is apparent that the GT-RLORC system is the most efficient. This is due to a combination of two factors: the largest thermodynamic potential due to the large difference between maximum and minimum operating temperatures of the system (1500°C and 70°C); and the higher efficiency of the bottoming cycle, due to the larger amount of thermal energy recovered from the GT exhaust gases. The *m*ORC units of the

GT-RORC and GT-RLORC systems feature considerably higher thermal efficiency if compared to those from other ORC units designed for automotive waste heat recovery, see e.g., Ref.[55]. This is a result of the high gas turbine exhaust temperature (approx. 800°C), which allows raising the ORC turbine inlet temperature to a very high value: 400°C.

Despite the fact that the GT-RORC and GT-RLORC systems feature the best predicted thermal efficiencies, these configurations are suboptimal, because of the considerable exergy destruction produced in the heat recovery exchanger, see Figs. 1.6b and 1.6c. An optimal system configuration which mitigates this drawback would include partial recuperation in the gas turbine. In this case, it would also be possible to reduce the TIT of the gas turbine, which could also be beneficial. Such alternative will be studied in future stages of this work.

The thermal efficiency of the gas turbine system has the largest influence on overall performance of the CC power plant. It follows that the optimal Brayton cycle pressure is close to that of the stand-alone μGT. Thus, the optimal maximum pressure is 4.4 bar for the CC system featuring a gas-to-gas recuperator. The CC systems with no recuperation require a larger maximum pressure: 15.3 bar for the GT-RORC system, and 14.2 bar for the GT-RLORC system.

Due to the very high gas turbine inlet temperature in GT-RORC and GT-RLORC systems, the corresponding outlet temperature largely exceeds 650°C for the optimal operating conditions: 746°C and 838°C, for the GT-RORC and GT-RLORC configurations, respectively. Hence, these power plants require a HRVG manufactured with special alloys or ceramic materials. On the other hand, the RGT-ORC system was designed following specifications which are representative of the state-of-art for μGTand mORC turbogenerators. It can operate with a heat exchanger manufactured with conventional materials, because the turbine outlet temperature is approximately 650°C. The RGT-ORC configuration is, from a technological point of view, the most currently feasible solution among those studied here.

Figure 4.5c displays the calculated total heat transfer coefficient UA, whose value, to a first approximation, is proportional to the size of the heat exchangers. The μGT of RGT-ORC system has a small pressure ratio and a small specific work, hence it requires large mass flow to achieve the targeted power output. Its recuperator has a large effectiveness (0.87), hence it features a large UA value. Moreover, note in Fig. 1.6a that the temperature difference between the hot and cold streams in the HRVG is small when compared against the other cases (see Fig. 1.6b and 1.6c for GT-RORC and GT-RLORC systems, respectively); the required heat transfer area is hence larger. It follows that the RGT-ORC system features the largest heat exchangers. Note also in Fig. 4.5c that the GT-RLORC system has a heat transfer coefficient slightly larger than GT-RORC system, due to its additional low-temperature heat recovery exchanger.

The energy content of the gas turbine exhaust is larger in cycles without recuperation. As a result, the GT-RORC and GT-RLORC systems feature a bottoming cycle with larger power output. This is beneficial for the ORC turbomachinery, because it leads to larger flow passages, thus reducing scaling effects (e.g., tip clearance losses). On the other hand, the resulting small height of the gas turbine blade might be problematic, resulting in lower fluid-dynamic performance of the machine.

Two cycle configurations were selected for the preliminary design of the turbines and the heat exchangers: the RGT-ORC system, as the corresponding power plant would boast the highest technological readiness; and the GT-RLORC system, because it would allow to reach a very high thermal efficiency..

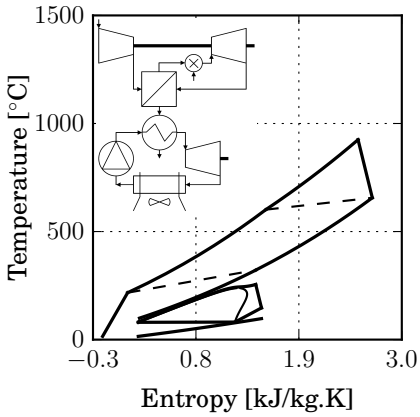

Net efficiency	-	0.374
Net power	kW	150
gas turb. outlet temp.	°C	656
Br./Rn. cycle efficiency	-	0.300 / 0.146
Br./Rn. mass flow rate	kg/s	0.803 / 0.353
Br./Rn. output power	-	120 / 32
Br./Rn. max. pressure	bar	4.4 / 49.1
Br./Rn. turbine power	kW	286 / 36
Br./Rn. pressure ratio	-	4.4 / 19.7
Br. recuperator duty	kW	332
Heat recovery HX duty	kW	205
Condenser HX duty	kW	173

(a) RGT-ORC

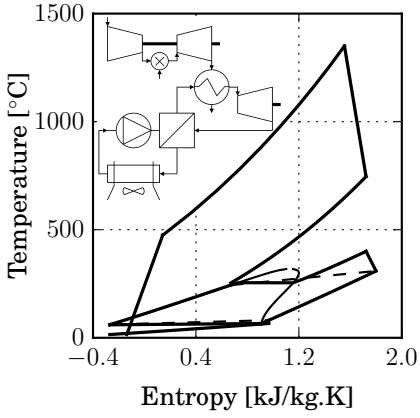

Net efficiency	-	0.422
Net power	kW	150
gas turb. outlet temp.	°C	746
Br./Rn. cycle efficiency	-	0.287 / 0.293
Br./Rn. mass flow rate	kg/s	0.287 / 0.295
Br./Rn. output power	-	102 / 51
Br./Rn. max. pressure	bar	15.3 / 17.7
Br./Rn. turbine power	kW	239 / 52
Br./Rn. pressure ratio	-	15.2 / 97.1
Heat recovery HX duty	kW	176
Rn. regenerator duty	kW	114
Condenser HX duty	kW	125

(b) GT-RORC

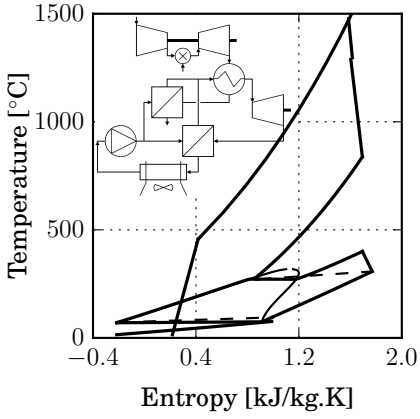

Net efficiency	-	0.440
Net power	kW	150
gas turb. outlet temp.	°C	838
Br./Rn. cycle efficiency	-	0.294 / 0.295
Br./Rn. mass flow rate	kg/s	0.231 / 0.336
Br./Rn. output power	-	96 / 57
Br./Rn. max. pressure	bar	14.2 / 22.4
Br./Rn. turbine power	kW	203 / 59
Br./Rn. pressure ratio	-	14.1 / 83.7
Heat recovery HX duty	kW	161
Rn. regenerator duty	kW	127
Condenser HX duty	kW	141
Low T. heat rec. HX duty	kW	37

(c) GT-RLORC

Figure 4.6: Optimal CC power plants. Temperature-entropy diagrams of the thermodynamic cycles and main design specifications. The gas turbine $T-s$ diagram has been scaled according to the ORC $T-s$ diagram.

PRELIMINARY DESIGN OF GAS AND ORC TURBINES

The combination of the low enthalpy drop in an ORC expansion, and the constraint on the volumetric flow ratio, allow to design a single-stage radial inflow turbine for all the bottoming cycles of the considered configurations. The same type of expander is selected for the μGT of the RGT-ORC system, due to its small pressure ratio (4.4). For the other μGT systems a four-stage axial machine has been chosen, in order to limit the rotational speed to values up to 150 krpm, thus easing the design of the bearing system. The selection/design of an electric generator coupled to all these turbomachines should not present a major challenge, given the the current level of technology: μGT operating with rotational speeds as high as 300 krpm have been already successfully coupled with high-speed electrical generators [16]. Table 4.2 displays the main constraints utilized in the optimization. The work of Bahamonde *et al.* [36] includes a detailed explanation of the procedure followed for the turbine preliminary design.

Table 4.2: Main constraints for the turbine optimization

Constraints		
rotational speed	krpm	≤ 150
blade height (radial/axial)	mm	≥ 2 / ≥ 5
relative mach number at rotor inlet	-	≤ 0.9
blade tip speed	m/s	≤ 700
maximum flare angle	°	≤ 15
minimum shaft diameter	mm	≥ 10
relative mach number at rotor outlet	-	≤ 1.4
maximum stator angle (radial/axial)	°	80 / 75

Table 4.3 presents the main results of the meanline design of the μGTand *m*ORC turbine of the RGT-ORC and GT-RLORC systems. The difference in the total-to-static efficiency can be explained by means of the size parameter and the volumetric expansion ratio [56, 57]. Machines with a small size parameter generally undergo considerable tip clearance losses

Table 4.3: Turbine specifications

cycle configuration	-		**RGT-ORC**		**GT-RLORC**
turbine type	-	RIT-μGT	RIT-ORC	AXT-μGT	RIT-ORC
working fluid	-	flue gas	cyclopent.	flue gas	toluene
power	kW	303.2	33.8	195.0	64.0
total-to-static eff.	-	0.911	0.746	0.843	0.873
rotational speed	krpm	57.3	150.0	150.0	95.5
size parameter	mm	54.8	13.6	25.3	31.7
vol. exp. ratio	-	2.9	29.6	7.5	60.0

and Reynolds effects. Likewise, efficiency penalties from compressibility effects and large flow area variations are related to a large volumetric expansion ratio. The radial inflow gas turbine of the RGT-ORC system features the largest size parameter and the smallest volumetric expansion ratio, thus its estimated efficiency is the highest. The lower efficiency of the other turbines is a result of a combination of a large volumetric expansion ratio and small size parameter. In particular, note that the cyclopentane machine seems to be strongly affected by the low size parameter, which is mostly caused by the comparatively lower power output (half the one of the toluene turbine). Future stages of this project will

study the utilization of alternative fluids with a larger molecular complexity, which allow the design of turbines with a larger size parameter (e.g., siloxanes [58]). Finally, for the axial turbine, the constraints on the blade height and rotational speed do not allow to design stages operating with the optimal specific speed.

PRELIMINARY DESIGN OF THE HEAT EXCHANGERS

A commercial software has been employed for the heat exchanger design [10]. Figure 4.7 shows the weight of the heat exchangers for RGT-ORC and GT-RLORC systems. The contribution of the different HEX's to the overall weight of the CC unit is somewhat proportional to the corresponding UA values. Figures 4.8 and 4.9 display the temperature profile and the overal dimensions of the heat exchangers, for RGT-ORC and GR-RLORC systems, respectively.

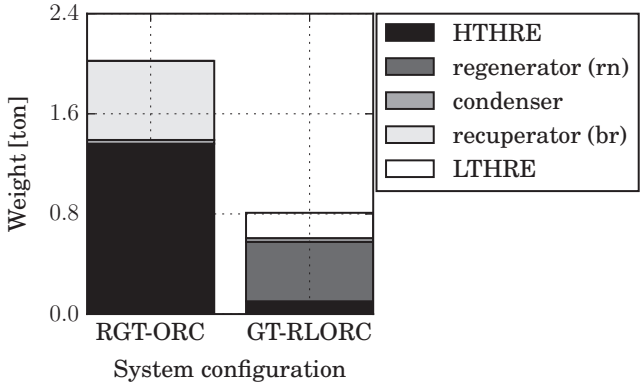

Figure 4.7: Heat exchangers weight for a net power output of 150 kW.

The weight of the CC system is critical, because it must be added to the weight of the batteries, potentially reducing the truck payload. Due to this reason, only the system that is predicted to be the lightest, GT-RLORC system, is considered for the fuel economy analysis. The corresponding analysis of the system obtained with state-of-the-art components, the RGT-ORC system, is left for future developments.

4.3.2. ANALYSIS OF THE FUEL ECONOMY AND ESTIMATION OF THE EMISSIONS

Table 4.4 lists the parameters for the quasi-steady-state simulation with the corresponding information sources. Two types of vehicle propulsion systems are analyzed: a heavy-duty vehicle powered by a diesel reciprocating engine (CV), and a heavy-duty vehicle with a series hybrid powertrain (HEV). The total weight of both configurations is taken equal to 80000, which is the roadways legal limit in the United States. Consequently, as shown in Figure 4.10b, the cargo weight varies as a function of the vehicle type and battery capacity.

The efficiency map of the reciprocating engine has been scaled to match expected performance improvements in the upcoming years the peak value has been set to 0.50. Additionally, and as a first approximation, the battery energy efficiency has been kept fixed at 0.95 [44]. The CC system efficiency is assumed to have slightly lower than that calculated for the GT-RLORC power plant, in order to take into account generator and transmission losses. Finally, thanks to the multi-fuel capability of gas turbines, two types of fuel have been considered for the HEV: diesel and compressed natural gas (CNG).

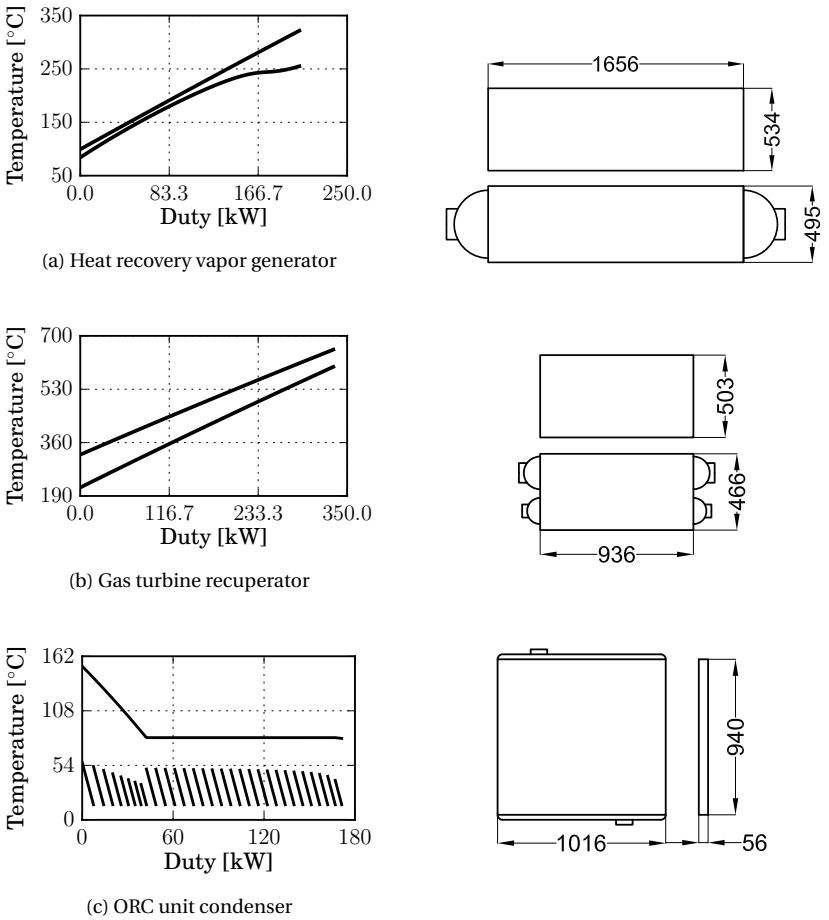

(a) Heat recovery vapor generator

(b) Gas turbine recuperator

(c) ORC unit condenser

Figure 4.8: RGT-ORC system. Temperature profile diagrams and overall dimensions of the heat exchangers in mm. The preliminary dimensions have been obtained with a commercial software[10].

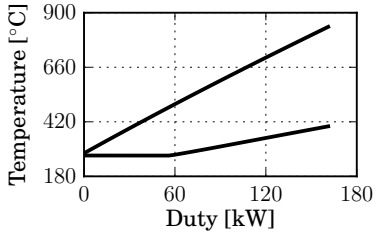

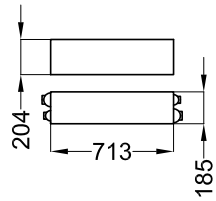

(a) Heat recovery vapor generator. Pinch temperature: 10 K.

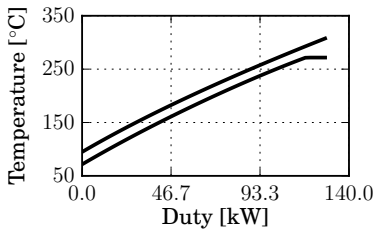

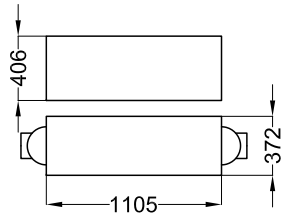

(b) ORC unit regenerator

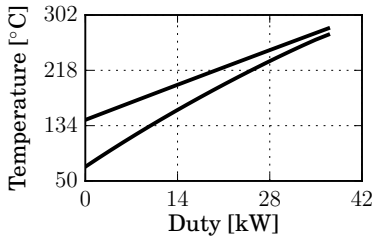

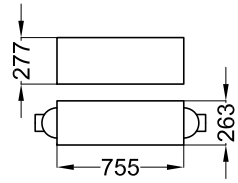

(c) ORC unit low T. exchanger

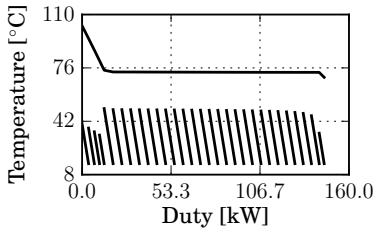

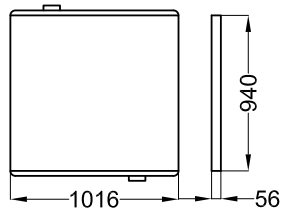

(c) ORC unit condenser

Figure 4.9: RGT-RLORC system. Temperature profile diagrams and overall dimensions of the heat exchangers in mm. The preliminary dimensions have been obtained with a commercial software[10].

Table 4.4: Key parameters of the quasi-steady-state simulation

		CV	HEV
Components weight			
Trailer[1]	ton	2.25	2.25
Cargo[1]	ton	30.41	refer to Fig. 4.10b
Prime mover	ton	1.43[1]	0.8
Transmission[1]	ton	0.33	0.33
Wheel/axle[1]	ton	1.44	1.44
Fuel	ton	0.34	varies
Exhaust aftertreatment[1]	ton	0.09	-
Electric motor/gen. + inverter[2]	ton	-	0.23
Battery	ton	-	from 1 to 4
Total weight[2]	ton	36.29	36.29
Components efficiency			
Reciprocating engine (peak)[1,3]	-	0.50	-
Reciprocating engine (idle)[4]	-	0.11	-
Electric motor/gen + inverter (peak)[1]	-	-	0.94
Battery[6]	-	-	0.95
Combined cycle	-	-	0.44
CC generator + transmission	-	-	0.96
Battery specifications			
Energy density[7]	kW.h/kg	-	0.183
Power density[7]	kW/kg	-	0.817
Max/min state of charge	%	-	90/10
Other parameters			
Engine power at idle[9]	kW	4.3	-
Power required by auxiliaries[9]	kW	1.3	1.3
Fuel	-	diesel	diesel, CNG
CC system power	kW	-	151.3
References			
[1]Alliance for Sustainable Energy, LLC [39], [2]California Department of Transportation [59], [3]Gibble and Amar [60], [4]Rahman *et al.* [61], [5]Holmberg *et al.* [62], [6]Ehsani *et al.* [44], [7]Bower [41], [8]Taguchi *et al.* [20], [9]Stodolsky *et al.* [63]			

DRIVING CYCLE

Long-haul trucks spend 85% of their mission time in cruise conditions (at 85 km/h), and might have an idling time between 6 and 16 hours [61, 63]. A representative average mission has been constructed based on this information, because standard driving cycles do not represent real missions [64]. The velocity-time profile is formed by two standard driving cycles and idling time: Urban Dynamometer Driving Schedule for Heavy-Duty Vehicles (UDDSHDV): 0 - 0.4 hours; Heavy Heavy-Duty Diesel Truck Schedule (HHDDT): 0.4 - 11 hours; idling: 11 - 17 hours.

FUEL ECONOMY AND EMISSIONS

Table 4.5 presents the main results calculated for the mission of the next-generation CV. The miles-per-gallon (mpg) are close to those obtained in a similar study [64]. Figure 4.10

Table 4.5: Results of the simulation performed on a vehicle employing a diesel reciprocating engine

Miles per gal. mpg	Fuel economy ton-cargo.km/kg-fuel	Payload ton	CO_2 emissions kg-CO_2/ton-cargo.km
5.4	79.63	30.41	$6.2 \cdot 10^{-3}$

shows the results of the HEV analysis for different battery capacity values. These results are expressed as percentage gain with respect to the CV solution.

The fuel economy units have the kg of fuel at the denominator; they are thus affected by the lower heating value (LHV). For instance, in an analysis where the payload and the required mechanical energy remain constant, the vehicle employing a fuel with higher LHV will require a lower mass of fuel, thus featuring a higher fuel economy.

The fuel economy gain is shown in Figure 4.10a. Since the results are affected by the LHV, the solution using diesel fuel is appropriate to perform a comparison between the CV and the HEV. The prime mover of the HEV is less efficient than the reciprocating engine: it has additional transmission losses, and the peak efficiency of the CC system is lower than that assumed the reciprocating engine (0.44 and 0.50, respectively). As a result, a HEV with a small battery will necessarily feature a negative fuel economy gain, as shown in Fig. 4.10a. Since it is assumed that the battery is fully charged with renewable energy, it is necessary to increase the battery size to obtain a positive gain: at least 300 kW.hr according to Fig. 4.10a.

A better fuel economy compared to that of the CV has been calculated for the vehicles operating with CNG fuel, independently from the battery capacity value. This is caused by the higher LHV of CNG, which leads to a lower consumption of kilograms of fuel.

Observe in Fig. 4.10a that the fuel economy can be largely improved by increasing the battery capacity. However, since the total weight cannot exceed 36.29 ton, increasing the fuel economy requires reducing the cargo weight, as shown in Figure 4.10b. The analysis of the corresponding economic trade-off is left for future developments. The prospect of the adoption of CNG as fuel for heavy duty vehicles seems positive, as its price will likely be lower compared to oil, at least in the United States [65]. Moreover, even if the constraint on the weight is released and the payload remains constant, the fuel economy will increase in proportion to the battery capacity, as it can be inferred from the trend in Fig. 4.10a.

The analysis of the emissions is done only for the HEV powered by the CC system operating with CNG. However, note that the gas turbine can also operate with diesel, and that it has been proven that the corresponding emissions are lower than those from a reciprocating engine (NO_x at 80% and CO at 99% less than the required levels), thanks to lean premix combustion preventing local hot spots [46]. Figures 4.10c and 4.10d display the estimates of the HEV emissions compared to the EPA and EURO-VI standards. The emissions calculated for the HEV are well below the regulated limits, without the need of an exhaust aftertreatment system.

Finally, Figure 4.10e presents the comparison of the computed CO_2 discharge from the HEV compared against that of the CV. A reduction of 30% with respect to the CV propelled by a next-generation diesel engine seems achievable.

4.4. CONCLUDING REMARKS

This paper documents a preliminary assessment of a hybrid electric powertrain for heavy-duty vehicles employing a combined cycle power plant composed by a micro gas turbine

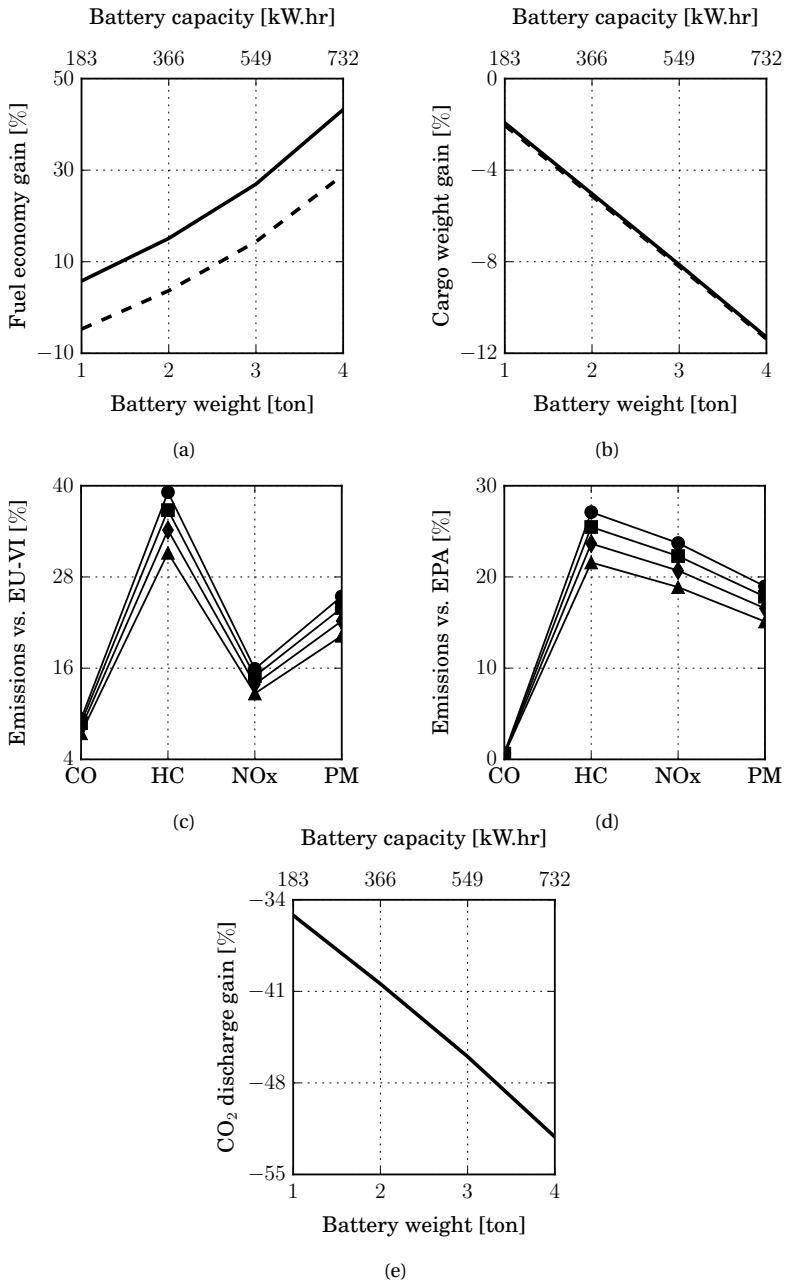

Figure 4.10: a) HEV fuel economy and b) cargo weight gain as a function of the battery capacity and with the CC system operating with (-) natural gas, and (–) diesel. c-d) Emissions compared against the Euro VI, and EPA standards: battery weight of (•) 1 ton, (■) 2 ton, (⧫) 3 ton, and (▲) 4 ton. e) CO_2 emissions gain of the HEV.

and a mini organic Rankine cycle system. The hybrid power train is of series type. It follows that the gas turbine is decoupled from the truck power demand, and thus the combined cycle system runs always at design conditions. As test case, the performance of the proposed powertrain concept is evaluated for a long-haul truck (weight approx. 36 ton) performing a representative mission. Two fuel options were explored for the μGT: diesel and compressed natural gas. As benchmark for the HEV, a conventional truck powered by a diesel reciprocating engine is considered. The relevant conclusions stemming from this work are:

- The selected combined cycle system features a thermal efficiency of 0.44. It is constituted by a non-recuperative gas turbine and a regenerative organic Rankine cycle system with an additional low temperature heat recovery exchanger. This system requires forefront technology: a μGT with film blade cooling for a maximum operating temperature of 1500°C, and a high-temperature heat recovery exchanger manufactured with special alloys or ceramics that can operate at 840°C.
- For a diesel-fueled hybrid powertrain, the fuel economy (ton-cargo.km/kg-fuel) can be improved by employing a battery with a capacity of at least 300 kW.hr. The hybrid vehicle powered by natural gas has even more potential, because it features a higher fuel economy with ultra low emissions.
- When compared with EPA and EURO-VI standards, the hybrid powertrain fueled by natural gas produces emissions which are much lower than those required by regulations, without the need of an exhaust aftertreatment system. Likewise, the CO_2 discharge produced by the HEV fueled with natural gas is at least 30% lower than that of the diesel reciprocating engine.

In summary, this work demonstrates that the adoption of a combined cycle system in a hybrid powertrain has a considerable merit potential in terms of fuel economy and exhaust emissions. Future planned investigation will expand the analysis to cover these aspects:

- other CC system configurations;
- turbine fluid dynamic losses caused by film blade cooling;
- effect of startup and shutdown on the fuel economy and emissions;
- integrated thermodynamic cycle and heat exchanger design optimization to minimize the powertrain weight and volume.

REFERENCES

[1] European Commission, Climate Action, *Reducing CO_2 emissions from heavy-duty vehicles.* (2017), last updated 29 December 2017.

[2] L. Guzzella and A. Sciarretta, *Vehicle Propulsion Systems. Introduction to Modeling and Optimization.* (Springer-Verlag., 2013).

[3] U.S. Department of Energy, *Maps and data - vehicle weight classes & categories,* (2018), last updated 14 March 2018.

[4] I. Aharon and A. Kuperman, *Topological overview of powertrains for battery-powered vehicles with range extenders,* IEEE Transactions on Power Electronics **26**, 868 (2011).

[5] Daimler Trucks North America LLC, *Natural gas freightliner,* (2017), last updated 29 December 2017.

[6] A. Goodarzi, *Ushybrid: Integrated electric, fuel cell and hybrid powertrain components powering clean mobility,* in *Hydrogen + Fuel Cells + Batteries Group Exhibit Hannover* (2017).

[7] Wrightspeed Powertrains, *Wrightspeed technology,* (2017), last updated 29 December 2017.

[8] Chrysler Corporation: Technical Information Engineering office, *Hystory of Chrysler Corporation Gas Turbine Vehicles*, Tech. Rep. (Chrysler Corporation, 1979).

[9] C. Invernizzi, P. Iora, and P. Silva, *Bottoming micro-Rankine cycles for micro-gas turbines,* Applied Thermal Engineering **27**, 100 (2007).

[10] Aspen Technology, Inc., *Exchanger design and rating V 8.8,* (2015).

[11] L. Guzzella and D. Ambühl, *Quasistatic simulation toolbox,* (2005).

[12] Python Software Foundation, *Python 2.7,* (2017).

[13] The Mathworks, Inc., *Simulink-simulation and model-based design, v 7.3,* (2017).

[14] P. Colonna, T. P. van der Stelt, and A. Guardone, *FluidProp (Version 3.0): A program for the estimation of thermophysical properties of fluids,* (2012), Asimptote bv.

[15] I. Bell, J. Wronski, S. Quoilin, and V. Lemort, *Pure and pseudo-pure fluid thermophysical property evaluation and the open-source thermophysical property library Coolprop,* Industrial & Engineering Chemistry Research **53**, 2498 (2014).

[16] W. Visser, S. Shakariyants, and M. Oostveen, *Development of a 3 kW microturbine for CHP applications,* Journal of Engineering for Gas Turbines and Power **133**, 042301 (2011).

[17] P. Lu, T. Fu, S. Garg, and G. Nowakowski, *Boiler Stack Gas Heat Recovery*, Tech. Rep. (Naval Civil Engineering Laboratory Port Hueneme California, 1987).

[18] C. McDonald and C. Rodgers, *Small recuperated ceramic microturbine demonstrator concept,* Applied Thermal Engineering **28**, 60 (2008).

[19] M. Vick, T. Young, M. Kelly, S. Tuttle, and K. Hinnant, *A simple recuperated ceramic microturbine: design concept, cycle analysis, and recuperator component prototype tests,* in *ASME Turbo Expo: Turbomachinery Technical Conference and Exposition*, GT2016-57780 (2016) p. 14.

[20] H. Taguchi, K. Komori, O. Kido, F. Nishiwaki, and Y. Nishiyama, *Micro gas turbine system,* (2017).

[21] J. Horlock, *Advanced Gas Turbine Cycles* (Pergamon, 2003).

[22] W. C. Reynolds and P. Colonna, *Vapor power plants,* in *Thermodynamics* (Cambridge University Press, 2018) Chap. 7, in Press.

[23] M. Moran, H. Saphiro, and D. Boettner, *Fundamentals of Engineering Thermodynamics*, 7th ed. (Wiley, 2010).

[24] Y. Chang and C. Wang, *A generalized heat transfer correlation for louver fin geometry,* International Journal of Heat and Mass Transfer **40**, 533 (1997).

[25] R. Shah and D. Sekulić, *Fundamentals of Heat Exchanger Design* (John Wiley & Sons, Inc., 2003).

[26] W. Kays and A. London, *Compact Heat Exchangers*, 3rd ed. (Krieger Publishing, 1998).

[27] Y. Chang, K. Hsu, Y. Lin, and C. Wang, *A generalized friction correlation for louver fin geometry,* International Journal of Heat and Mass Transfer **23**, 2237 (2000).

[28] M. Spiga and R. Dall'Olio, *Friction factor and nusselt number in flat tubes with rounded edges,* International Journal of Heat and Fluid Flow **16**, 307 (1995).

[29] G. Gnielinski, *New equation for heat and mass transfer in turbulent pipe and channel flow,* Internation Chemical Engineering **16**, 359 (1976).

[30] J. Hesselgreaves, *Compact Heat Exchangers - Selection, Design and Operation* (Pergamon, 2001).

[31] M. Taylor, *Plate-Fin Heat Exchangers: Guide to their Specification and Use* (HTFS, 1990).

[32] R. Lockart and R. Martinelli, *Proposed correlation of data for isothermal two-phase two-component flow in a pipe,* Chemical Engineering Progress **45**, 39 (1949).

[33] M. Yadav, S. Giri, and V. Momale, *Sizing analysis of louvered fin flat tube compact heat exchanger by genetic algorithm,* Applied Thermal Engineering **125**, 1426 (2017).

[34] Asimptote bv, *zturbo, a 1D tool for the preliminary design of turbines operating with higly non-ideal fluids,* (2017).

[35] M. Pini, G. Persico, E. Casati, and V. Dossena, *Preliminary design of a centrifugal turbine for organic Rankine cycle applications,* Journal of Engineering for Gas Turbines and Power **135**, 042312 (2013).

[36] S. Bahamonde, M. Pini, C. De Servi, and P. Colonna, *Method for the preliminary fluid dynamic design of high-temperature mini-ORC turbines,* Journal of Engineering for Gas Turbines and Power **139**, 082606 (2017).

[37] A. Head, C. De Servi, E. Casati, M. Pini, and P. Colonna, *Preliminary design of the ORCHID: A facility for studying non-ideal compressible fluid dynamics and testing ORC expanders,* in *ASME Turbo Expo*, Vol. 3 (2016) p. 14.

[38] M. Pini, C. D. Servi, M. Burigana, S. Bahamonde, A. Rubino, S. Vitale, and P. Colonna, *Fluid-dynamic design and characterization of a mini-ORC turbine for laboratory experiments,* in *Energy Procedia: IV International Seminar on ORC Power Systems*, Vol. 129 (2017) pp. 1141–1148.

[39] Alliance for Sustainable Energy, LLC, *Advanced vehicle simulator (ADVISOR),* (2016).

[40] Saft Batteries, *High energy lithium-ion cell,* (2005).

[41] G. Bower, *Tesla semi truck battery is how big?* (2017), last updated 4 May 2017.

[42] UQM Technologies, Inc., *Powerphase HD 220 specifications,* (2017).

[43] B. Sharpe and R. Muncrief, *Literature Review: Real-world Fuel Consumption of Heavy-duty Vehicles in the United States, China, and the European Union*, Tech. Rep. (International Council on Clean Transportation, 2015).

[44] M. Ehsani, Y. Gao, S. Gay, and A. Emadi, *Modern Electric, Hybrid Electric, and Fuel Cell Vehicles. Fundamentals, Theory, and Design* (CRC Press LLC, 2004).

[45] W. De Paepe, M. Montero, S. Bram, A. Parente, and F. Contino, *Experimental characterization of a T100 micro gas turbine converted to full humid air operation*. The 6th International Conference on Applied Energy ICAE2014 (2014).

[46] Capstone Turbine Corp., *Capstone announces launch of CARB emissions certified product to operate in hybrid electric vehicles,* (2010), last updated 21 June 2010.

[47] Capstone Turbine Corp., *Capston turbine C30 CNG microturbine certified to carb 2010 requirement for on-road heavy-duty diesel engines for urban bus,* (2010), last updated 27 December 2010.

[48] S. Hoekman and C. Robbins, *Review of the effects of biodiesel on NOx emissions,* Fuel Processing Technology **96**, 237 (2012).

[49] I. A. Reşitoğlu, K. Altinişik, and A. Keskin, *The pollutant emissions from diesel-engine vehicles and exhaust aftertreatment systems,* Clean Technology Environmental Policy **17**, 15 (2015).

[50] A. Date, *Analytic Combustion: With Thermodynamics, Chemical Kinetics and Mass Transfer* (Cambridge University Press, 2011).

[51] A. Massardo, C. McDonald, and T. Korakianitis, *Microturbine/fuel-cell coupling for high-efficiency electrical-power generation,* Journal of Engineering for Gas Turbines and Power **124**, 110 (2002).

[52] C. Invernizzi, P. Iora, G. Manzolini, and S. Lasala, *Thermal stability of n-pentane, cyclopentane and toluene as working fluids in organic Rankine engines,* Applied Thermal Engineering **121**, 172 (2017).

[53] J. Harinck, D. Pasquale, R. Pecnik, J. Buijtenen, , and P. Colonna., *Performance improvement of a radial ORC turbine by means of automated design*. Proceedings of the Institution of Mechanical Engineers, Part A: Journal of Power and Energy **227**, 637 (2013).

[54] Autozone, Inc., *Duralast radiator,* (2017).

[55] L. Shi, G. Shu, H. Tian, and S. Deng, *A review of modified organic Rankine cycles (ORCs) for internal combustion engine waste heat recovery (ICE-WHR),* Renewable and Sustainable Energy Reviews **92**, 95 (2018).

[56] A. Perdichizzi, *Design criteria and efficiency prediction for radial inflow turbines,* in *ASME Turbo Expo*, 87-GT-231 (1987) p. 9.

[57] G. Angelino, C. Invernizzi, and E. Macchi, *Organic working fluid optimization for space power cycles,* (Springer-Verlag, Berlin, 1991) Chap. 16, pp. 297–326.

[58] P. Colonna, E. Casati, C. Trapp, M. T., J. Larjola, T. Turunen-Saaresti, and A. Uusitalo, *Organic Rankine cycle power systems: from the concept to current technology, applications and an outlook to the future,* Journal of Engineering for Gas Turbines and Power **137**, 100801 (2015).

[59] California Department of Transportation, *Weight limitation,* (2017).

[60] J. Gibble and P. Amar, *Volvo supertruck powertrain technologies for efficiency improvement,* in *U.S. Department of Energy's Annual Merit Review* (2016).

[61] S. Rahman, H. Masjuki, M. Kalam, M. Abedin, A. Sanjid, and H. Sajjad, *Impact of idling on fuel consumption and exhaust emissions and available idle-reduction technologies for diesel vehicles - a review,* Energy Conversion and Management **74**, 171182 (2013).

[62] K. Holmberg, P. Andersson, N. Nylund, KariMäkelä, and A. Erdemir, *Global energy consumption due to friction in trucks and buses,* Tribology International **78**, 94 (2014).

[63] F. Stodolsky, L. Gaines, and A. Vyas, *Analysis of Technology Options to Reduce the Fuel Consumption of Idling Trucks*, Tech. Rep. ANL/ESD-43 (Argonne National Laboratory, 2000).

[64] H. Zhao, A. Burke, and M. Miller, *Analysis of class 8 truck technologies for their fuel savings and economics,* Transportation Research Part D **23**, 55 (2013).

[65] S. Brown, *Natural gas vs. oil in U.S. transportation: Will prices confer an advantage to natural gas?* Energy Policy **110**, 210 (2017).

5

CONCLUSIONS AND PERSPECTIVES

This dissertation presents and discusses design methodologies for high-temperature *m*ORC power plants. In particular, its focus is the integrated and concurrent design of the thermodynamic cycle, working fluid, and turbine. It also documents the preliminary design of a high-temperature *m*ORC unit for automotive waste heat recovery. Each chapter includes self-contained concluding remarks. Here, relevant learnings deriving from this project are integrated and summarized.

5.1. CONCLUSIONS

Realizing the turbine preliminary design is a complex task, because the specifications of the optimal machine are intertwined with those of the thermodynamic cycle and the selection of the working fluid. These aspects are particularly important in the design of *m*ORC machines, because the design space is affected by special limitations if compared to the design of conventional and larger ORC power plants. For instance, the selection of the working fluid, thermodynamic cycle and turbine preliminary design are mutually constrained, because increasing the maximum system pressure to maximize the cycle thermal efficiency might lead to a turbine blade height that is below the limits imposed by manufacturing restrictions. As a result, during the optimization process, bounding the design space is possibly the most important step. Performing this operation with rules of thumb from conventional turbomachinery practice can lead to suboptimal solutions: the computer optimizer that is commonly employed to obtain the turbine preliminary design often fails to find a feasible combination of thermodynamic parameters (like cycle pressure and turbine inlet temperature) and turbine specifications (like rotational speed, degree of reaction, or minimum blade height). The work presented in Chapter 2 demonstrates that it is possible to reveal a feasible design space *a priori*, by means of first principles combined with simple assumptions on the turbomachinery performance. This method is then used for the design of a *m*ORC system (power output 10kW) employing three different expander configurations: a single-stage radial inflow, a three-stage radial outflow, and a three-stage axial turbine. The results suggest that a radial inflow turbine is the best machine for high-temperature *m*ORC power plants: the optimal pressure ratio is not limited by the blade height, and its performance is weakly dependent on tip clearance losses.

Incorporating the working fluid design in the optimization process is an ambitious yet compelling challenge. This can be done by including the parameters of the fluid thermodynamic models in the optimizer design space. As a result, the cumulative number of variables defining the thermodynamic cycle, the turbine, and the working fluid, can easily surpass the dozen. Such problem features the curse of dimensionality: solving it requires considerable computational resources, and it is practically impossible to find a global optimum. The work presented in Chapter 3 tackles this difficulty by employing *active subspace methods* to create a reduced-order model of the turbine total-to-static efficiency function. The method is applied to the design of a *m*ORC system operating with a single-stage radial inflow turbine. The resulting surrogate model is a smooth bidimensional response surface that offers significant advantages. Its evaluation consumes negligible computational resources, because it is an explicit algebraic equation. Moreover, the search for the global optimum can be restricted to a small region in the response surface. The solutions in this region contain information regarding the turbine geometry, the working fluid parameters, and the thermodynamic cycle operating conditions. An engineer can thus select the best alternative from this set of solutions that feature different turbine specifications (e.g., ro-

tational speed or diameter), but offer the same performance. Finally, the new model can be used to infer which parameters are dominant with respect to turbine performance, thus leading to design guidelines applicable to high-temperature *m*ORC systems. In the current study, the most influential turbine design inputs are the stator inlet to outlet radius ratio, the specific speed, and the rotor outlet geometric angle. Similarly, the most important fluid model parameters are the molar mass, the critical temperature, and the acentric factor.

The potential of *m*ORC systems is ultimately demonstrated in Chapter 4, which reports the preliminary design of a combined cycle unit as a prime mover for an innovative hybrid electric power train for heavy-duty vehicles. This power plant is constituted by a micro gas turbine (μGT) fueled by natural gas or diesel, and discharging its thermal energy to a *m*ORC unit operating with toluene as a working fluid. It is decoupled from the traction gear by employing a hybrid series configuration. Therefore, it runs at optimum conditions independently from the vehicle power demand. The combined cycle unit is designed for a net thermal efficiency of 0.44, and it features a non-recuperative μGT and a regenerative *m*ORC system. The hybrid power train has notable advantages. Its fuel economy is higher than that of a vehicle powered by a cutting-edge diesel reciprocating engine. Additionally, it is estimated that it produces emissions that are less than half the limit imposed by United States and European regulations, without the need of an exhaust aftertreatment system. Finally, its discharge of greenhouse gases is at least 30% lower than that from a diesel engine over a representative driving cycle.

5.2. PERSPECTIVES

The design of a *m*ORC unit constitutes a multidimensional optimization problem that might encounter conflicting objectives and design variables that are mutually constrained. The work presented in Chapter 2 tackles this challenge by integrating the turbine design and the thermodynamic cycle calculation in a single function. Future developments must also account for the weight and volume of the heat exchangers, which play a major role in the design of *m*ORC systems for applications like waste heat recovery for propulsion engines (e.g., for those of truck, aircraft, ships, etc.) where weight and volume, to a different degree, are important factors.

Active subspace methods have been used to integrate the working fluid model, the thermodynamic cycle specifications, and the turbine preliminary design, in a bidimensional reduced-order model. This achievement suggests the existence of few turbomachinery similarity parameters that might incorporate the nature of the working fluid molecular interactions. The development of such principles would lead to an integral framework that could be used to provide relevant answers with respect to the selection or optimization of a turbine configuration and its working fluid. Moreover, with negligible computational time, the reduced-order model allows the exploration of new working fluids that could be synthesized in the near future.

The preliminary design of the combined cycle system as a prime mover for a hybrid-electric power train elucidates the benefits of *m*ORC technologies: in this particular case, as the reduction of fuel consumption and emissions for heavy-duty road transport. The next steps must consider the integrated design of cycle and heat exchangers, in order to minimize the combined cycle weight and size, and also to conceive a first layout of the entire system. Furthermore, the turbomachinery efficiency predicted by the meanline analysis must be confirmed by higher-fidelity models, or, in the best case, by experimentation.

Finally, the design of the compressor for the gas turbine, and the pump for the ORC system, should be also performed, in order to confirm the efficiencies assumed in the cycle calculation.

From the system optimization standpoint, this dissertation demonstrates that, with a high efficiency, compactness and relative simplicity, high-temperature *m*ORC systems are potential game changers in the new energy scenario. Furthermore, around the world, many theoretical studies are being performed also at component level. It is the moment now to take the next natural step: the realization of experimental power plants; only then the full potential of *m*ORC systems can be explored. The role of private organizations is fundamental in this respect; not only their financial support is necessary, but also their openness, because understanding their needs is paramount to bridge academia with society. Therein lies the significance of this entire project, for it is the author's hope that its results encourage private partners to establish a productive and long-lasting relationship with research groups working in this field.

ACKNOWLEDGMENTS

This short text might seem insufficient to recognize everyone's contribution. However, be sure that I am grateful for each person and event that brought me to this moment. With this very sentence, I invoke you all.

Piero, thank you for giving me the opportunity to pursue this PhD. I am always impressed by your enthusiasm and your positive attitude. I can only assume that such strength comes from doing something you truly love.

Matteo, thank you for your supervision. In particular, thank you for your kindness and for providing me with stimulating research ideas, which were instrumental in the second part of this work, during a difficult stage in my project. Carlo, thanks also for your supervision. I appreciate your rigorousness and I have learned very much from it. I want to thank also the members of the committee for the time they invested in my graduation process.

Where would I be without my dear PhD acquaintances from the interracial room? All these years of liver/braincell-depleting and entropy-generating activities were a worthy experience. Know that I have many dear pre-blackout memories, which I will cherish forever. In some way, you have all authored this dissertation: Adamo, Andre, Beyoncé, Lucy, Nando, Nightish, Salvo, Tiemo, Tony.

Many others were there to drink a beer, tell a bad joke (or listen to one), or to do some sport: the members of the KKK office, the yellow room, Synext, A.C. Brancaleone, the people from the old days in P&E, my friends in Ecuador, my extended family... the list is large. I am very grateful for all the time we shared.

Querida familia, cualquier cosa que escriba es insuficiente para describir lo agradecido que estoy por todo, les llevo en mi corazón donde sea que vaya. Papá Roberto y mamá Teresa, ñañito Tito y ñañita Emilia, gracias por haberme apoyado incondicionalmente cuando decidí dejar Ecuador. Para mis preciosas Vicky y Romi, les envío un abrazote enorme desde acá. David y Diani, gracias también por todo su cariño.

Finalmente, mi Cristina, princesita, pecosita, te amo mucho. Gracias por todo.

ABOUT THE AUTHOR

Juan Sebastián Bahamonde Noriega was born in Quito-Ecuador, the 23rd of June 1980. He obtained a bachelor's degree in Mechanical Engineering in 2005. After working for five years in the private sector, he came to the Netherlands to obtain a Master of Science, also in Mechanical Engineering, in the Delft University of Technology. The title of his Master's thesis is "Design method for s-CO_2 gas turbine power plants. Integration of thermodynamic analysis and components design for advanced applications". In 2013 he started a PhD project under the supervision of professor Piero Colonna. The title of his dissertation is "Integrated design methods for mini organic Rankine cycle power systems". Currently, he is a postdoctoral researcher in the Propulsion & Power group of the TUDelft, and the chief technical officer of Synext b.v.

PUBLICATIONS

S. Bahamonde, C. De Servi, A. Rubino, and Piero Colonna, *Optimized preliminary design method for mini-ORC power plants: an integral approach*, proceedings of the International Conference on Power Engineering, ICOPE-15-1188, pp. 9 (2015).

S. Bahamonde, M. Pini, and P. Colonna, *Active Subspaces for the Preliminary Fluid Dynamic Design of Unconventional Turbomachinery*, proceedings of the VII European Congress on Computational Methods in Applied Sciences and Engineering (4), pp. 8572-8586 (2016).

S. Bahamonde, M. Pini, C. De Servi, A. Rubino, and Piero Colonna, *Method for the Preliminary Fluid Dynamic Design of High-Temperature Mini-Organic Rankine Cycle Turbines*, Journal for Engineering for Gas Turbines and Power 139(8), pp. 082606-01-14 (2017).

S. Bahamonde, M. Pini, C. De Servi, and P. Colonna, *Active subspaces for the optimal mean-line design of unconventional turbomachinery*, Applied Thermal Engineering 127, pp. 1108-1118 (2017).

S. Bahamonde, C. De Servi, and P. Colonna, *Hybrid Electric Powertrain for Long-haul Trucks and Buses: Preliminary Analysis of a New Concept Based on a Combined Cycle Power Plant*, Proceedings of the Global Power & Propulsion Forum, GPPS-NA-2018-137, pp. 11 (2018).